THE FRACTURE TOUGHNESS AND MICROSTRUCTURE OF THE HEAT AFFECTED ZONE OF A WELDED MARAGING STEEL

by

M. C. Coleman, B.Sc., Grad.I.M.

A thesis submitted for the degree of Doctor of Philosophy of the University of Aston in Birmingham

October 1971

SYNOPSIS

The fracture toughness and microstructure of the heat affected zone of welded 300 grade maraging steel have been studied. Attention has been confined to full penetration welds produced in a single pass, and a wide range of processes has been covered. This has been achieved by use of a thermal simulation technique, the thermal cycles being based on heat flow theory. This approrach has been justified by correlating real weld heat affected zone properties and structures with these produced in simulation.

Fracture toughness has been found to be a function of peak temperature, being independent of heating and cooling rates. In the regions of the heat affected zone where changes occurred, the fracture toughness was greater than that of the parent material. These changes were related to particular peak temperatures, being 67.8 ksi$\sqrt{in}$ at 650°C and 59.6-70.1 ksi$\sqrt{in}$ over 1200°C-1400°C, as compared with the parent material value of 54.2 ksi$\sqrt{in}$. The increases in fracture toughness were accompanied by decreases in tensile strength in all cases.

The metallographic, fractographic and fracture toughness results have been correlated to explain the observed changes in fracture toughness. It has been shown that reverted austenite is responsible for the increased toughness associated with the peak temperature of 650°C whilst acicular structures account for the increased toughness in the peak temperature range 1200°C-1400°C. In the higher temperature range constitutional liquation of inclusions was detected, but did not produce grain boundary embrittlement.

The practical significance of the results is considered in terms of critical defect size and general applicability to other grades of maraging steel.

CONTENTS

PAGE NUMBERS CUT OFF IN ORIGINAL

1. INTRODUCTION

Maraging steels, developed in the late 1950's by the International Nickel Company, are a range of high strength steels that contain very little carbon. They gain their strength from the precipitation hardening which can be produced in iron-nickel martensite by a combination of cobalt and molybdenum. The term "maraging" derives from the combination of martensite and age-hardening.

Prior to the development of maraging steels, it appeared that low alloy steels had reached a strength maximum imposed by brittleness. The development of precipitation hardening stainless steels having carbon contents of about 0.2% did not solve the toughness problem. Precipitation hardening of low carbon iron-nickel martensite promised toughness and strength and it was this that led to the development of maraging steels. The heat treatment of these alloys involves a solution anneal at 820°C and hardening is achieved by ageing for three hours at 485°C. Problems of decarburisation, distortion or cracking are not encountered and consequently the manufacturing sequence is simpler than that of quenched and tempered high-strength steels.

The mechanical properties of maraging steels, notably their high strength and toughness, immediately made them promising for aerospace applications. Hydrospace vehicles, missile casings, cryogenic parts and various aircraft components have been manufactured from these alloys. Dimensional stability during ageing, due to the absence of a phase change, further increases their usefulness. In the manufacture of complex-shaped components considerable economic advantage can be gained from their use.

For many applications, particularly in the aerospace industry, it is necessary to utilise welded fabrications. It is possible to weld maraging steels by most conventional processes. Welding is usually carried out in the annealed condition, and the weld metal, heat affected zone (H.A.Z.) and parent material can be aged in one treatment. It is not necessary to preheat or post weld heat-treat and ageing usually produces the required properties.

The weld metal and H.A.Z. in any joint form a region of considerable complexity. In the weld metal the temperature experienced can be extremely high and a variety of rapid reactions can be occurring. In the H.A.Z., the welding thermal and strain cycles interact with the parent material producing in some cases a considerable number of structures and variation in properties over very small distances. In all welded fabrications it is essential that these complex regions can be relied on, and although some components can tolerate a range of properties, others demand more precise limits. This latter case is typical of the situation that arises in aerospace applications where maraging steel is often utilised.

Recently difficulties have been experienced in obtaining satisfactory properties, particularly fracture toughness, in the weld H.A.Z. of maraging steel. Both variation and scatter have been reported and, whilst some investigators consider the effects negligible, others have shown that catastrophic failures can occur. This conflict of opinion reflects on the fact that the effects of welding thermal cycles on the structure and properties of this alloy are not fully understood. Whilst much work has been carried out in this area on quenched

and tempered steels, little has been done on maraging steels that depend on precipitation hardening to attain their properties.

The difficulties that have been reported, appear to arise as the result of two distinct problems:

(1) the formation of reverted austenite

and (2) constitutional liquation of inclusions.

Both phenomena are dependent on the type of thermal cycles experienced, that is the heating rate, peak temperature and cooling rate. Consequently, they could be expected to arise and possibly cause problems in any maraging steel weld H.A.Z. To determine the reliability of a joint and evaluate such parameters as the critical defect size, it is necessary to obtain precise fracture toughness data relevant to these H.A.Z. problem areas.

In view of the difficulties reported and the lack of information concerning the effects of thermal cycles on welded maraging steel, it was decided to undertake a detailed and systematic examination of the fracture toughness and microstructural relationships in the H.A.Z. A range of welding heat inputs representative of the welding processes employed in practice have been studied. Attention has been confined to the conditions corresponding to full penetration welds produced in a single pass. This not only simplifies the approach to be used, but corresponds to a major field of application, namely the welding of thin sheet in the aerospace industry. It was anticipated that the investigation would not only yield quantitative data about the H.A.Z. of this alloy, but also contribute to a basic understanding of the

influence of thermal cycles on the structure and properties of alloys of this type.

Since maraging steels are welded by most of the conventional processes, to consider all these processes and the combinations of parameters in each process, has obvious practical limitations. Also, detailed examination of structures and properties in any real weld H.A.Z. is difficult because only small amounts of material are involved. Any normal mechanical tests applied to the H.A.Z. will only record the properties of a composite structure. These problems have been overcome by the development of simulative techniques for reproducing the thermal and possibly strain cycles of a weld H.A.Z. This enables a wide range of processes and parameters to be readily studied. Even more important however, it enables precise information to be obtained from any one structure by reproducing it uniformly in a specimen of sufficient size to apply normal testing techniques. Accordingly, this technique was adopted in the present work, and to substantiate the validity of this approach, correlation was made with real weld H.A.Z.s. Two processes were selected: submerged arc and M.I.G., such that relatively wide H.A.Z.s were produced and inaccuracies minimised.

To simulate a wide range of processes, it it necessary to know their corresponding thermal cycles. Direct experimental measurements are often difficult, particularly with narrow H.A.Z.s and again the number of processes involved presents a limitation. However, heat flow equations are available that enable thermal cycles to be calculated from welding parameters. In full penetration welds, two dimensional

heat flow conditions arise, and the equations relevant to this situation were used in this investigation. It is known that these equations give acceptable agreement with experimental values when applied to steels. In fact, the approach adopted in this investigation did not necessitate precise correlation with real thermal cycles but only a coverage of the range of heating and cooling rates which would be encountered.

2. LITERATURE REVIEW

2.1 Maraging Steels

A range of maraging steel alloys have been developed on the basis of the precipitation hardening capabilities of iron-nickel martensite. To obtain the optimum combination of properties requires specific heat treatments. To appreciate the properties produced and the heat treatments required it is necessary to understand the precipitation hardening mechanisms taking place. The development of these alloys, their properties and heat treatments, and the physical metallurgy involved will now be considered.

2.1.1 The development of maraging steels

The first grades of maraging steel, the 25% and 20% nickel steels, were developed by Bieber[1] in the late 1950s. These depended on a combination of titanium, aluminium and niobium to produce age-hardening in iron-nickel martensite. The 25% nickel steel requires a complex heat treatment as shown schematically in Fig. 2.1(a) taken from the work of Decker et al[2]. The ausaging treatment is necessary to raise the M_s temperature, and even then refrigeration is needed to promote complete transformation to martensite. This steel has a yield strength of about 250 ksi with a notched tensile strength to tensile strength ratio (NTS/TS) of 1.1. The alternative treatment shown in Fig. 2.1(a), involving cold work, improves these properties to 270 ksi and 1.3 respectively. In both cases reductions in area in excess of 50% are obtained with elongations of about 12%.

(a) 25% nickel steel

(b) 18% nickel steel

Fig. 2.1. The heat treatment cycles for different maraging steels (after Decker et al[2]).

The 20% nickel steel in contrast to the 25% grade requires a simple heat treatment. Solution annealing for one hour at 820°C produces a completely martensitic structure on air cooling to room temperature. Maraging is carried out at 485°C for three hours followed by air cooling. This produces a yield strength of 250 ksi and a NTS/TS ratio of 1.45. In both grades mentioned, the physical and environmental properties are similar, as are their advantages in terms of cold working, ease of machining, low distortion, freedom from decarburisation and weldability.

From these steels the 18% nickel maraging steels have developed. They were reported by Decker et al[2] and differ from the other grades since they used cobalt and molybdenum additions to produce the required properties. Three grades were mentioned, having yield strengths of 200, 250 and 300 ksi and NTS/TS ratios ranging from 1.5 to 1.6. In terms of plane strain fracture toughness, values from 150 ksi$\sqrt{in}$ for the 200 grade to about 60 ksi$\sqrt{in}$ for the 300 grade can be obtained. All three require the same heat treatment shown schematically in Fig. 2.1(b).

Details of the development of these grades is given by Decker et al[3]. Early work revealed that cobalt and molybdenum interacted to produce considerable hardening, and consequently a range of compositions was studied containing from 1.7% Co, 1.8% Mo to 7% Co, 5.4% Mo. The effects of these additions on the annealed and maraged martensite are shown in Fig. 2.2. This indicates that the additions produce weak solid solution hardening but a strong maraging effect, and it is suggested that this accounts for

Fig. 2.2. The effect of Co x Mo on the maximum hardness of nominally 18% Ni-Fe alloys (after Decker et al[3]).

Fig. 2.3. The effect of molybdenum on yield strength and NTS/TS ratio of 18.5% Ni, 7.5% Co, 0.4% Ti-Fe alloy (after Decker et al[3])

their combination of toughness and strength. Fig. 2.3 shows how strength is increased, with little deleterious effect on toughness as the molybdenum content is increased in a basically 18% Ni, 8% Co steel.

The effects of other elements were also studied[3]. It was found that titanium acted as a supplemental hardener as well as neutralising residual carbon and nitrogen by removing them from solution in the martensite. As titanium was increased from 0.1 to 0.7% in an 18% Ni, 7% Co, 5% Mo steel, the yield strength increased from 220 to 280 ksi. The NTS/TS ratio decreased in air melts containing more than 0.4% titanium but remained constant at about 1.5 for vacuum melts. Silicon and manganese were shown to be detrimental leading to lower notch-tensile strength and lower toughness. Up to 0.03% carbon produced no decrease in toughness, but melts containing 0.04 and 0.05% carbon had increasingly lower notch tensile strength. Aluminium was used throughout (0.1%) as a deoxidiser. Larger amounts supplemented hardening, but decreased toughness. It appears that elements other than the main alloying additions and titanium offer no advantages when an optimum combination of strength and toughness is required.

During the development of these alloys, variations in heat treatment as well as composition have been studied. Floreen and Decker[4] investigated the effects of annealing, warm or cold working, and ageing heat treatments on the properties of an alloy containing 18% Ni, 7% Co, 5% Mo, 0.2% Ti. Annealing times of one hour were used and they found that annealing temperatures between 600°C and 700°C

should be avoided in order to prevent the formation of reverted austenite, an important point that will be considered later in more detail.

The minimum solution annealing temperature to give a completely martensitic structure on cooling was found to be about 730°C. Annealing temperatures up to 1000°C gave about the same grain size but above this grain growth occurred. At high annealing temperatures, 1200°C plus, a coarse Widmanstatten morphology was evident in the microstructures, although it was emphasized that no difference in chemical composition or hardness was found between the light and dark areas and that the structures were entirely body centred cubic martensite.

From a combination of annealing and ageing treatments it was found that annealing above 820°C resulted in a decrease in hardness after ageing. A range of ageing temperatures were studied and it was found that ageing at 485°C produced the most satisfactory combination of ageing time and strengthening response. Prolonged or higher temperature ageing resulted in the formation of austenite and a consequent drop in hardness. Some advantages were gained from mechanical working, either warm working of the solution annealed austenite or cold working of the martensite. The strength increases were only slight however and it was suggested that with the proper finishing temperature at the end of hot rolling the anneal can be omitted to gain the benefit of warm work. This work was carried out at the same time as that of Decker et al[2,3] and the standard heat treatment suggested, annealing for one hour at 820°C, air

cooling, ageing for three hours at 485°C and final air cooling was used in Decker's work.

Many of the properties and advantages of maraging steel can be attributed to the low carbon content martensite. The physical metallurgy involved and comparisons with iron-carbon martensite will be dealt with in the next section, but specific properties will now be considered. In terms of processing, maraging steels are readily cast, resist hot tearing and can be hot or cold worked. During heat treatment, problems of decarburisation, quenching, through hardening and dimensional stability are not encountered.

Decker et al[2] report that the 18% nickel grades have properties generally superior to those of other maraging steels. Improved dimensional stability and exceptional resistance to sea water corrosion are noted. However, Contractor[5] records that the 18% nickel grades offer no advantage over other high strength low alloy steels in terms of sea water corrosion rate. Also, although the fatigue strength of maraging steel compares with other high strength steels, no distinct advantage is offered. However, distinct advantages are offered by maraging steels in terms of the mechanical properties of toughness and strength.

The benefit obtained from maraging steel is not strength alone, but a combination of strength and toughness. It has already been shown that within the maraging grades, the 18% nickel steels have the best combination of these properties[1,2]. When compared with other high strength steels their superiority is more pronounced. Matthews et al[6] have shown that above a tensile strength of about

200 ksi the notched tensile strength (indicative of toughness) decreases for most high strength low alloy steels but continues to increase for maraging steels as shown in Fig. 2.4.

For materials in general there appears to be an inverse relationship between strength and toughness. Srawley[7] has shown that in maraging steel fracture toughness was approximately proportional to the reciprocal of the yield strength squared. Similar relationships have been reported for other high strength steels, and Fig. 2.5 taken from a review by Corten[8] illustrates the superiority of maraging steels over other high strength steels in terms of combined toughness and strength. Further evaluation of the toughness properties of maraging steel is recorded by Contractor[5]. This indicates that maraging steels do not display a sharp ductile to brittle transition temperature. Consequently, whilst other high strength alloys might suffer from a rapid loss of toughness with decreasing temperature, this is not so with maraging steels.

Finally, advantages can be gained from maraging steel in terms of fabrication. They can be welded by most processes, a factor that will be given further consideration later. In the solution annealed condition they can be machined and formed using conventional tools and plant, and strengthening can be achieved after these operations.

2.1.2 <u>The physical metallurgy of maraging steels</u>

A considerable quantity of literature has been published relating to the physical metallurgy of maraging steels. Some of the earlier results have been discussed in the review of Contractor[5] but a considerable amount of work

Fig. 2.4. Comparison of notched tensile strength of alloy steels at various strength levels (after Matthews[6]).

Fig. 2.5. Fracture toughness of steels as a function of yield strength (after Corten[8]).

has been done since then. The latest and more complete review is that of Floreen[9] and this provides the background to the present consideration.

2.1.2.1 Iron-nickel martensite

The martensite produced in maraging steels forms by a process of diffusionless shear, as in conventional carbon steels[3]. However, the nature of the transformation and the product contrast sharply with that of conventional steels. To appreciate these differences it is useful to consider the iron-rich end of the iron-nickel equilibrium diagram as given by Owen and Liu[10] shown in Fig. 2.6. This indicates that at lower temperatures the equilibrium phases are ferrite and austenite. However, on cooling an 18% nickel maraging steel from the austenite range it does not decompose into the equilibrium phases, but forms martensite[3].

Jones and Pumphrey[11] have determined the metastable iron-nickel diagram, Fig. 2.7, and this relates martensite transformation temperature and nickel content. This explains the formation of martensite in maraging steel. This transformation is insensitive to cooling rate, and even if held for long times in the two phase region the austenite will not decompose into the equilibrium phases. Instead with further cooling martensite forms. This presents one of the differences between iron-nickel and iron-carbon martensites. In the former, because of the high nickel content and virtual absence of carbon, hardenability is not a problem and the cooling rate after annealing is unimportant.

Iron-nickel martensite also contrasts with iron-carbon martensite in that it exhibits no tetragonality, but has a

Fig. 2.6. The iron-rich portion of the iron-nickel equilibrium diagram (after Owen and Liu[10]).

Fig. 2.7. The metastable iron-nickel diagram (after Jones and Pumphrey[11]).

b.c.c. crystal structure. This is only moderately hard, 300 Hv, but, as already shown, very tough compared with the high hardness and brittleness of untempered iron-carbon martensite. Tempering does not occur on reheating, and these differences can be directly attributed to the absence of carbon. The hysteresis of the transformation allows considerable reheating of the martensite for ageing, in the presence of alloying additions, before reversion to austenite occurs. The martensite will break down to the equilibrium phases at elevated temperatures below the A_s, but the rate of the reaction at 485°C is slow enough for considerable precipitation hardening to occur before reversion takes place.

It has been shown by several investigators that the Jones and Pumphrey diagram is oversimplified. Swanson and Par[12] indicate that in alloys containing between 0 and 10% nickel ferrite will form at slow cooling rates. However, alloys between 10 and 25% nickel form a completely martensitic matrix, referred to as massive martensite, and transmission electron microscopy indicates that all grades of 18% nickel maraging steel have this structure.

The massive martensite structure consists of laths or platelets and contains a high dislocation density. Studies of this structure in 18% nickel binary[13] and iron-nickel-chromium ternary alloys[14] by Floreen, have shown they possess good tensile ductility and impact properties. It is suggested that after ageing, a massive martensite gives better toughness than a twinned martensite. Martensite formation in plain carbon steels[15] and in iron-nickel

alloys[16] has shown that twinned martensite formation is favoured with lower M_s temperatures. Hence, to avoid twinned martensite and gain the benefits of increased toughness, it is desirable to raise the M_s temperature. Alloying elements commonly used generally lower the M_s temperature, but one significant exception is cobalt which raises the M_s temperature in iron-nickel alloys[17]. This has meant that in maraging steels the effect of cobalt has allowed higher alloy contents to be added, whilst maintaining a massive martensite matrix and its advantages in terms of toughness.

The high dislocation density present in massive martensite has also been linked to the rapid rate of hardening during maraging. The maraging reaction, and the strengthening precipitates formed will now be considered.

2.1.2.2 Maraging reactions

A considerable amount of effort has gone into studying maraging reactions and identifying the precipitates formed. In the majority of cases the technique adopted has been the study of diffraction patterns from extracted precipitate particles. This in itself has often proved difficult because the precipitates are very small. Overaged specimens have been used in some cases but this gives rise to a certain amount of debate. Many believe that the precipitation process takes place in stages and by studying overaged structures the initial stages may be missed.

Most investigators have observed two distinct precipitates, but disagreement arises over identification. Reisdorf[18] designates them Ni_3Mo and the hexagonal phase Ni_3Ti, whereas Miller and Mitchell[19] consider them to be

the Laves phase Fe_2Mo and Ni_3Ti. Other variations have been suggested, but one of the major difficulties in positively identifying the precipitates is that many of the phases that might be anticipated from compositional considerations have very similar "d" spacings. To overcome this problem Marcus et al[20] and Chilton and Barton[21] have both adopted different approaches. The former utilised Mossbauer spectroscopy whilst the latter measured the angles between planes from selected area diffraction patterns. In both cases the main precipitate was identified as Ni_3Mo, but the secondary precipitate was concluded to be Fe_2Mo and sigma FeTi respectively.

The exact role of titanium in 18% nickel maraging steel has also led to a variety of conflicting opinions. Some investigators[19] have indicated that the titanium precipitate was probably Ni_3Ti. Others[21] suggest that part of the titanium may be present in the molybdenum precipitate giving $Ni_3(Mo,Ti)$. Again the problem arises that the similar structures of Ni_3Ti and Ni_3Mo make simultaneous identification of both very difficult. In general, there appears to be agreement that Ni_3Mo is the primary hardening precipitate in maraging steel and that some form of titanium precipitate is also formed. However, the idendity of the titanium precipitate and other possible precipitates still need to be definitely determined.

Chemical analysis of the precipitates extracted from maraging steel has shown that the precipitate compositions are not simply those indicated by the structural formulae reported. Generally, the precipitates contained a considerable

amount of iron and sometimes small amounts of other alloying elements. Cobalt however was usually present only in small quantities if at all. The Mossbauer study[20] also indicated that no significant precipitation of cobalt occurred during maraging. Nevertheless, cobalt undoubtedly plays an important role in maraging steels in conjunction with molybdenum and this will now be considered.

2.1.2.3 The cobalt-molybdenum interaction

It was Decker et al[3] who found that combinations of cobalt and molybdenum produced greater strengthening in iron-nickel alloys than the sum of the strength increments produced when they were added individually. Floreen and Speich[22] confirmed this, and remarked that the strength level attained was much greater than would be expected from ternary data. They suggest that the added strengthening is due to the formation of a finer dispersion of molybdenum precipitates. It was considered that cobalt might have lowered the solubility of molybdenum in the matrix and this increased the amount of precipitate. Miller and Mitchell[19] also came to this conclusion.

Peters and Cupp[23] studied the resistivity changes in a series of ternary and quaternary alloys during ageing. They found that cobalt additions accelerated the ageing reaction and confirmed that it increased the amount of molybdenum precipitated. The suggestion that cobalt may alter the dislocation density of the martensite matrix and provide a higher more uniform number of dislocation sites for subsequent precipitation is mentioned by Floreen[9]. If changes in dislocation distribution were important then

it would be expected that cobalt would have raised the strength of a number of alloys studied[22]. However, the strong hardening effect of cobalt was only found in conjunction with molybdenum, and even without cobalt massive iron-nickel martensite has a very high dislocation density.

Floreen and Speich[22] noted from the range of alloys they studied that the 18% Ni, 8% Co, 5% Mo steel had fracture toughness properties distinctly superior to any of the other quaternary alloys. This they attributed to the fact that segregation and, or, precipitation at former austenite grain boundaries was not observed in the molybdenum containing alloys, but was observed in those without molybdenum. However, they did not consider this to be an effect of the cobalt-molybdenum interaction, but rather that molybdenum prevented grain boundary embrittlement analogous to molybdenum minimising temper embrittlement. Whatever the mechanism, it remains undisputed that the 18% nickel maraging steels do exhibit excellent fracture toughness.

2.2 Fracture Toughness

The fracture toughness of maraging steel and how it is affected by welding are the concern of this research. Before reviewing these specific aspects, some of the fundamentals of fracture must be considered.

The energy absorbed in fracturing an impact specimen is commonly used to indicate the toughness of a material. Such tests provide simple control standards, but the relationship between energy absorbed and the toughness of a component in service is empirical. An energy approach provided the first quantitative treatment of fracture, but the more recent linear elastic fracture mechanics approach has resulted in more useful parameters. These topics will be reviewed, as well as the practical implications of fracture toughness and the relationships between toughness and microstructure.

2.2.1 Surface energy-plastic work approach

Griffith[24], using a stress solution provided by Inglis[25], considers the growth of an elliptical crack of length 2a in an infinite plate of unit thickness. For the crack to advance the release of stored elastic strain energy must be greater than the increase in surface energy. This is shown in Fig. 2.8[26] and the point of instability leads to a definition of a gross fracture stress, σ_f, as

$$\sigma_f = \left[\frac{2E\gamma}{\pi a}\right]^{\frac{1}{2}} \qquad \ldots\ldots 2.1$$

where E is Young's Modulus and γ the surface energy of the plate material. This well known Griffith equation holds well for brittle and semi-brittle materials. The major

Fig. 2.8. Schematic representation of the energy balance of a crack in an infinite plate (after Weiss and Yukawa[26]).

objection in applying the equation to metals arises from plastic deformation that is observed even during cleavage fracture[27]. Orowan[28] and Irwin[29], independently, conclude that in metals the energy balance is primarily between elastic energy release and plastic work. Since the basic Griffith relationship is valid,

$$\sigma\sqrt{a} = \text{constant} \qquad \ldots\ldots 2.2$$

the addition of a plastic work factor, P, was considered sufficient to extend its applicability. The significance of P can be appreciated from the estimate that it is 10^4 to 10^6 times greater than γ. Irwin called the total work consumed per unit area of crack extension G, the strain energy release rate. At the point of instability its value is denoted by G_c and is analogous to $(\gamma + P)$. Thus

$$\sigma_f = \left[\frac{2EG_c}{\pi a}\right]^{\frac{1}{2}} \qquad \ldots\ldots 2.3$$

In short crack situations for ductile materials a fracture stress exceeding the ultimate strength can be predicted. Consequently, the Irwin-Orowan modified equation can only be justified in certain situations. The inadequacy of the energy approach, particularly the surface energy and plasticity aspects has resulted in an alternative approach to fracture. This gives rise to linear elastic relationships and will now be considered.

2.2.2 Stress intensity approach

Irwin[30] has shown that a fracture criterion expressed in terms of energy has its equivalent stress and strain, and

whilst this does not resolve the energy balance problems no statement concerning the use of released elastic energy is required. Paris and Sih[31] show there are three basic modes of crack surface displacement, Fig. 2.9. Irwin has analysed the stress fields for each of these cases. The most common situation of a crack spreading arises under normal stresses, that is mode I, and the stress fields for this mode are:

$$\left.\begin{aligned} \sigma_x &= \frac{K_I}{(2\pi r)^{\frac{1}{2}}} \cdot \cos\frac{\theta}{2}\left[1 - \sin\frac{\theta}{2}\sin\frac{3\theta}{2}\right] \\ \sigma_y &= \quad " \quad\quad " \quad\left[1 + \quad " \quad " \quad\right] \\ \tau_{xy} &= \quad " \quad \sin\frac{\theta}{2}\cos\frac{\theta}{2}\cos\frac{3\theta}{2} \end{aligned}\right\} \quad \ldots\ldots 2.4$$

Fig. 2.10 relates to the above equations and shows the co-ordinates measured from the leading edge of a crack and the stress components in the crack tip stress field. The parameter K_I is called the stress intensity factor and it is important to notice that identical stress fields are obtained for identical K values. Therefore, if for a given material fracture occurs when a critical stress distribution is reached then this is characterised by a critical value, K_c. This material constant K_c, is a material property in the same way as are yield stress and tensile stress.

The essential feature of the stress distribution at the tip of a crack in a flat plate is the highly concentrated longitudinal stress. As Barnby[32] shows, Fig. 2.11, in the important region close to the crack tip where x is small, a uniform applied stress σ_a produces a local tensile stress, σ_y,

Fig. 2.9. The basic modes of crack surface displacement (after Paris and Sih[31]).

Fig. 2.10. Co-ordinates measured from the leading edge of a crack and the stress components in the crack tip stress field (after Paris and Sih[31]).

Fig. 2.11. The stress distribution below the root of a notch (after Barnby[32]).

that is theoretically infinite when x = 0 and decreases as x increases according to

$$\sigma_y = \frac{K_I}{\sqrt{2\pi x}} \qquad \ldots\ldots 2.5$$

K_I depends upon the applied stress, and for a given crack situation K will increase as σ_a increases up to a critical level, K_c, when the local stress level is high enough to allow the crack tip to propagate. Paris and Sih[31] show from strain energy considerations of Irwin that

$$K_I = (EG_1)^{\frac{1}{2}} \qquad \text{for plane stress}$$

and

$$K_I = \left[\frac{EG_1}{1 - \nu^2}\right]^{\frac{1}{2}} \qquad \text{for plane strain} \qquad \ldots\ldots 2.6$$

These equations illustrate that a direct relationship exists between strain energy rates and stress intensity factors. Both the energy concept and the stress intensity concept have been based on infinite plate models, but for practical purposes relationships in specimens of finite width are required. It has been shown[32] that in the general form

$$K_I = Y \sigma_a \sqrt{a} \qquad \ldots\ldots 2.7$$

where Y is a geometrical constant. This shows how, in principle, the material constant K can be measured and will be considered later.

The limitations of the stress intensity approach have been considered by Paris and Sih[31]. They conclude that the only real limitation arises from plastic non-linear,

behaviour at the crack tip. Plastic deformation always occurs during crack propagation, but the linear elastic equations are considered satisfactory provided the crack tip plastic zone is small compared with the crack size. The application of fracture mechanics to the general yield situation, and the crack opening displacement (C.O.D.) concept are at present receiving considerable attention, but this is beyond the scope of this review. The factors affecting the plastic zone size will now be considered.

2.2.3 Constraint stresses and plastic yielding

At the root of a notch in a thick plate the concentrated local stress σ_y gives rise to constraint stresses in the x and z directions because of the Poisson effect[32]. The distribution of these stresses is shown in Fig. 2.12 and they are related by

$$\sigma_z = \nu (\sigma_y + \sigma_x) \qquad \ldots\ldots 2.8$$

Since σ_x and σ_z are the result of geometrical constraint they must be zero at the specimen surface.

Two distinct situations arise from this stress distribution that depend on plate thickness. In thin plates the σ_z stress does not develop. All the stresses lie in the plane of the plate and the situation is termed plane stress. In thick plates σ_z does develop and all the strain displacements lie in the plane of the plate giving rise to the plane strain situation. Theoretically the local stress at the root of a notch is infinite, equation 2.5. In practice the stress distribution is cut off at the yield stress, and for plane stress conditions this is the uniaxial tensile yield

(a) Variation of σ_y and σ_x across width

(b) Variation of σ_z through the thickness

Fig. 2.12. The three dimensional stresses below the root of a notch (after Barnby[32]).

stress σ_{ys}. Under plane strain conditions the Tresca or Von Mises conditions for plastic yielding show that σ_y will be higher than σ_{ys}. Using the Tresca condition for simplicity

$$\sigma_y = \sigma_{ys} + \sigma_3 \qquad \ldots\ldots 2.9$$

where σ_y is the maximum and σ_3 the minimum principle stress.

These stress levels are shown schematically in Fig. 2.12a and indicate that going from plane stress to plane strain conditions reduces the plastic zone size. The fact that σ_y can rise above σ_{ys} is the basic reason for increased brittleness at a notch that generates its own triaxial stresses.

It has been shown[32] that under plane stress conditions the plastic zone size r_y is given by

$$r_y = \frac{1}{2\pi}\left[\frac{K_{Ic}}{\sigma_{ys}}\right]^2 \qquad \ldots\ldots 2.10$$

and for plane strain conditions is

$$r_y = \frac{1}{5.6\pi}\left[\frac{K_{Ic}}{\sigma_{ys}}\right]^2 \qquad \ldots\ldots 2.11$$

During fracture the crack tip is preceded by this plastic zone. The smaller plane strain plastic zone consumes the minimum energy. This means that the toughness increases as thickness decreases, as shown in Fig. 2.13. Under plane strain conditions the fracture toughness is designated K_{Ic} and represents the minimum resistance of a material to crack propagation.

Fig. 2.13. The relationship between plate thickness and fracture toughness (after Barnby[32]).

2.2.4 Fracture toughness testing

The experimental basis for determining the plane strain fracture toughness of metallic materials has been investigated for ASTM committee E-24 by Brown and Srawley[33]. A number of materials have been studied and the specification includes many specimen designs. A general review of this work will not be made, but the relevant details and the recommended procedure for bend specimens[34] will be fully covered in the experimental procedure.

2.2.5 Applied fracture mechanics

The main advantage of the fracture mechanics approach is that results from laboratory tests can be applied to practical situations. It has been shown[35] from the work of Irwin[36] that the critical flaw size for pressure vessels and other structures can be calculated as follows

$$\text{Surface flaws} \quad (a/Q)_{cr} = \frac{1}{1.21\pi}\left[\frac{K_{Ic}}{\sigma}\right]^2 \quad \ldots\ldots \quad 2.12$$

$$\text{Embedded flaws} \quad (a/Q)_{cr} = \frac{1}{\pi}\left[\frac{K_{Ic}}{\sigma}\right]^2 \quad \ldots\ldots \quad 2.13$$

where $(a/Q)_{cr}$ - critical flaw size

a_{cr} - critical flaw depth

σ - the normal applied stress

and Q - the flaw shape parameter.

Values of Q can be obtained for various shapes of flaw and ratios of applied stress to yield stress, as shown in Fig. 2.14.

Tiffany and Masters[37] have demonstrated how this approach can be applied to a variety of practical situations.

Fig. 2.14. Flaw shape parameter curves for surface and internal flaws (after Tiffany and Masters[37]).

They show that measured critical flaw sizes can be predicted from laboratory tests with a reasonable degree of accuracy. They also estimate the life of pressure vessels subjected to cyclic and sustained stresses and conclude that the stress intensity concept can be used in the evaluation of subcritical flaw growth. Cottrell and Langstone[38] reporting on various aspects of fracture toughness, have studied the effect of a flaw in a rocket motor casing undergoing hydraulic proof testing. Using the relevant critical flaw size equation they show good correlation between predicted and actual failure stress.

Even though many practical results support this approach, it is necessary to realise that some problems still exist. One of the most difficult problems is to decide whether a pressure vessel will fail catastrophically, or leak prior to fracture. It is argued[35] that the extremes are generally easy to determine, but an intermediate area exists where prediction is more complex. The difficulty can be demonstrated by considering a subcritical flaw growing under plane strain conditions. On reaching a point of instability and propagating through the material thickness it may then be arrested by the increase in toughness associated with plane stress conditions.

The difficulties of accounting for variations in toughness are also discussed by Cottrell[39] in terms of the zones of welded joints. Variations in K_{Ic} and σ_{ys} from the weld metal, through the heat affected zone and into the parent plate are common in welded structures. For each combination of these parameters there is a corresponding

critical flaw size. This assumes that the stress acting in each zone is the same, but as Cottrell remarks, in a weld which is not fully heat treated there will be local residual stress and this must be taken into account. This illustrates the need for detailed information from each zone and presents further practical difficulties. Nevertheless, as Cottrell shows[39], by considering the problems that arise and accounting for them, applied fracture mechanics presents an extremely useful and valid approach.

2.2.6 Fracture toughness and microstructure

Complex and extremely fine microstructures are typical of materials combining high strength and toughness. Consequently in trying to establish quantitative relationships between microstructure and toughness it is difficult to decide which structural features are important. Few models have been established that can be applied generally, but a considerable amount of work has been carried out in this area.

Grain size is the microstructural variable most often measured and controlled. Grain refinement has the distinction of being the only structural change that almost always increases strength and toughness together. The relationship between yield stress and grain size is given by the well known Petch equation[40]

$$\sigma_{ys} = \sigma_i + kyd^{-\frac{1}{2}} \qquad \ldots\ldots 2.14$$

where σ_i is the friction stress, ky the dislocation locking term and 2d the grain size. The implications of this equation have been well examined and Fig. 2.15 from the work

Fig. 2.15. Yield stress, tensile fracture stress and strain to fracture as a function of grain size in iron. A ductile to brittle transition can be seen at a grain size defined by $d^{-\frac{1}{2}} \simeq 3\ mm^{-\frac{1}{2}}$ (after Low[41]).

of Low[41] indicates how a ductile to brittle transition dependent on grain size is explained in terms of the Petch plot.

In martensitic and bainitic structures quantitative assessments have been attempted in terms of prior austenite grain size. English and Backofen[42] report that the strength of tempered martensite structures and the length of martensite plates have been related to the prior austenite grain size. However, Duckworth et al[43] suggest that the parameter of significance in fracture is the plate width. Further, they show that for a five fold change in prior austenite grain size in Ni-Cr steel, the martensite plate width and toughness are relatively constant. Contrary to this, it is reported[42] that fracture toughness increased with austenitising temperature (larger grain size) but plate width was fairly constant.

Such inconsistency has led to other parameters being selected for measurement and correlation with toughness. A structural unit relevant to fracture could be a region bounded by high-angle boundaries, and the important factor to determine may be whether neighbouring plates or needles are similarly orientated[42]. In iron-carbon martensite the individual needles may be the relevant parameter, but in massive martensite high angle boundaries only arise between blocks of martensite[43]. Birkle et al[44] used this latter parameter but were unable to correlate toughness and block size in maraging steel, which again suggests that the significant structural feature is of some other type.

In high strength steels the obvious "other type" of structural feature is the hardening precipitate. Thin film electron microscopy has enabled the interaction of precipitates and dislocations to be studied and the importance of precipitate size and distribution have been clarified. In general precipitates can be classified into those that are small and coherent with the matrix and those that are larger and incoherent. Incoherent precipitates since they limit slip band lengths on which cracking depends, may improve toughness[45]. However, as many workers have shown[46,47,48] larger particles may be cracked by intersecting slip bands and it is important that particles are not so large that a crack across them would propagate unstably into the matrix.

The effect of coherent precipitates, since they do not limit the length of slip bands, may be embrittlement[45]. However, Floreen and Hayden[49] show that suitable dispersions of small precipitates in maraging steel increase the strength without causing brittleness and explain their findings in terms of the precipitates acting as barriers to slip. Floreen[9] reports workers in agreement who have observed precipitates causing tangles and bowing of dislocations, whilst in opposition others who suggest shear through the precipitate occurs. It is generally accepted that the precipitates in maraging steel are coherent[42], and it is undisputed that high strength and toughness are obtained. However it is equally clear that the exact mechanism of dislocation-precipitate interaction has not been established.

Extension of electron microscopy to the study of replicated and real fracture surfaces has introduced other parameters through which fracture toughness and microstructure can be related. Beacham and Pelloux[50] discuss this approach, and present a classification of fracture mechanisms. In high strength materials crack propagation takes place by the formation and coalescence of microvoids giving rise to characteristic dimples on the fracture surface. The voids form at precipitates or inclusions during plastic deformation and can arise as microcracks in the matrix or particles, or by decohesion. Coalescence occurs by internal necking between the voids and crack tip as well as between voids removed from the crack tip.

Roesch and Henry[51] have studied the relationship between precipitation and dimpled fracture in maraging steel. In overaged structures they show correlation between the two. However, K_{Ic} measurements were not made and little could be said about the influence of the normal hardening precipitates. Floreen[9] discusses the problems of studying these precipitates and suggests that the excellent toughness found in maraging steel may be a result of Ni_3Mo being metastable. Conceivably this may start going into solution during the normal ageing treatment and give a structure of Ni_3Mo precipitates with adjoining austenite. This could be very effective in preventing void formation at the precipitates, but as yet remains a theory.

The role of ductility in void formation and coalescence must be of some significance. Tetelman and McEvily[52] show that a measure of ductility can be obtained from a tensile

test in terms of uniform elongation or reduction in area, but to relate either quantitatively to fracture is difficult. Krafft[53] has attempted this through the strain hardening exponent n and shows that increased toughness correlated with increased n for a range of steels. Krafft suggests that discreet units ahead of the crack go through a full stress-strain cycle resulting in tensile instability and the nucleation and coalescence of voids. Each unit represents a process zone size, d_T, and was found to be constant for a given material. The model gives

$$K_{Ic} = En(2\pi d_T)^{\frac{1}{2}} \quad \ldots\ldots 2.15$$

This has been modified to account for triaxial stresses[54] to

$$K_{Ic} = E\left[(\sigma_{ys} + \sigma_{uTS})/E + n/2\right](2\pi d_T)^{\frac{1}{2}} \quad \ldots\ldots 2.16$$

On the basis of this model, the process zone size should be related to microstructural features such as inclusions or precipitates. Birkle et al[55] have analysed fracture surfaces in Ni-Cr-Mo steels of different sulphur contents and heat treatments. In all cases as the sulphur content increases, sulphide spacing, dimple size and toughness decreased. A detailed analysis of one heat treatment showed good agreement between the sulphide spacing and d_T predicted from Krafft's original model. Spitzig[56] has applied the modified equation to the same results, although they are not attributed to Birkle et al by the author, and includes some of the heat treatments not fully analysed. The correlation

obtained at one heat treatment[55] is considered fortuitous, and shown not to hold generally.

The crack opening displacement (C.O.D.) model proposed by Wells[57] relates the onset of fracture to a critical displacement at the crack tip $2V_c$, thus

$$K_{Ic} = \left[2E\sigma_{ys}(2V_c)\right]^{\frac{1}{2}} \qquad \ldots\ldots 2.17$$

From the failure mode of high strength materials it may be possible to relate K_{Ic} to dimple depth assuming this to represent $(2V_c)$. Spitzig[56] records that a relationship has been suggested between $(2V_c)$ and microstructural Features[58], but finds no correlation with sulphide spacing. Having disposed of two models Spitzig proposes one based on stretched zone size, this being a region between the fatigue crack and microvoid regions. A degree of correlation between fracture toughness and this parameter is suggested but the validity of this is not clearly demonstrated. From the fractographs shown the zone is not clear, and its proposed relationship to the C.O.D. model[59] does not agree with the results presented. Finally, only nine results are reported[56] and in five of these stretched zones were either not observed or not detected because of insufficient material.

The difficulties encountered in applying models and interpreting results has been shown. Precise and complete agreement between theory and experiment is rare. Consequently in any further attempt to relate microstructure and toughness it is probable that such difficulties and disagreements will be encountered.

2.3 The Microstructure and Properties of Welded Maraging Steel

The toughness and strength offered by maraging steels has stimulated much work toward utilising these alloys. In many applications, fabrication techniques involving welding are used, and a considerable amount of work has been carried out in this area. Welding processes from electron beam[60] to submerged arc[61,62] have been studied and it appears that maraging steels can be welded by most of the conventional processes.

Although few practical difficulties arise in producing a welded maraging steel joint, problems have been reported in obtaining satisfactory joint properties, particularly fracture toughness. These arise both in the weld metal and the H.A.Z. In certain cases the weld metal represents the weakest region of the joint and some consideration will be given to this area and the methods of overcoming these problems. However, it is the main purpose of this review to cover the H.A.Z. regions and in particular two major phenomenanthat are connected with property variations will be considered.

2.3.1 Weld metal

An extensive study of the plane strain fracture toughness of welded maraging steel has been made by Romine[63]. Various regions of the welded joint were tested and comparisons made with the longitudinal and transverse properties of the parent plate. In almost every case the weld metal fracture toughness was lower than that of the parent plate. Typical values ranged between 62 and 70 ksi$\sqrt{in}$ for M.I.G.

weld metal and 90 to 120 ksi√in for the parent plate. These agree with the trend reported in earlier work by Romine[64] where fracture toughness values in T.I.G. welds ranged between 46 and 63 ksi√in as compared with parent plate values of 73 and 93 ksi√in. Corrigan[65], studying M.I.G. and T.I.G. welds, also indicated that the weld metal was the weakest region of the joint.

In a study of M.I.G., T.I.G. and electron beam welds Adams and Travis[66] show that in terms of tensile strength joint efficiencies averaging 96% can be obtained. However, in electron beam welds low ductility was reported. Further work on electron beam remelted material indicated that loss of strength and embrittlement could be related to directional solidification and the consequent distribution of inclusions. D'Annessa[67] has made a detailed study of the solidification dependent aspects of fracture in T.I.G. maraging steel welds. Macroscopic and microscopic features of fracture varied depending on the orientation of the fracture path with respect to the welding direction, but the significance of this in terms of mechanical properties is not reported. In all cases fracture occurred by ductile dimple formation and it was considered to be the result of void formation at solute rich areas and inclusions. This conclusion was also reached by Kenyon[68]. The details of Kenyon's work are particularly relevant to another section and consequently will be considered later.

In most cases, the problems reported in maraging steel welds have been overcome by techniques aimed at controlling the weld metal composition. Witherell et al[69] indicate

that weld metal hot cracking can be prevented by adjusting the filler metal composition to obtain a different weld metal composition. Additions can also be made to the weld metal through fluxes in such cases as submerged arc and manual metal arc welding. Wilson and Wildman[62] have studied submerged arc welding of maraging steel and consider that to obtain the optimum joint properties it is essential to control the recovery of titanium in the weld metal. To achieve this a number of fluxes were developed to give controlled slag-metal reactions and these were used in conjunction with filler wires of various compositions. Although the parent plate ultimate tensile strength of 140 tons/sq.in. could not be matched, strengths up to 120 tons/sq.in. were achieved in the weld metal giving joint efficiencies of 85%. Finally, a factor that must be considered with all welded joints is good fit. Bailey[70] has shown that solidification cracking can occur in M.I.G. and manual metal arc welds in thick plate maraging steel. Although this was partially attributed to sulphur segregation, by ensuring good joint alignment it was possible to produce weld metal having sufficient strength and toughness to match the parent plate.

2.3.2 Weld heat affected zone

The microstructure and properties of a weld H.A.Z. often differ from those of the parent material. Since the weld H.A.Z. is a region subjected to a range of thermal and mechanical cycles such differences are not surprising. The important factor is that the nature of any structural change, and the resulting properties, should be fully understood and their significance assessed in terms of joint reliability.

In the work of Romine[63] the H.A.Z. fracture toughness of maraging steel was measured in three regions, immediately at the fused metal interface, at the dark etching band (the 650°C peak temperature isotherm), and at an intermediate position. A considerable range of results was obtained, both for different processes and different testing orientations. In the case of a T.I.G. weld, the dark band and intermediate region fracture toughness values, parallel to the plate rolling direction, were 118 and 116 ksi√in respectively whilst the parent plate was 130 ksi√in. Similar figures for a M.I.G. weld were 100, 107 and 120 ksi√in tested transverse to the rolling direction. The reverse of this situation is reflected in the results taken from another T.I.G. weld H.A.Z. tested transverse to the rolling direction, the values being 121 and 128 ksi√in whilst the parent plate was 92 ksi√in. In general the region immediately at the fused zone interface had a toughness greater than the parent plate. A major objective of this work was to obtain a practical basis for evaluating fracture toughness in welds. Consequently, metallographic examination was not carried out and the significance of the results is not discussed in terms of microstructure.

Similar variations in properties have been reported by Salmon Cox et al[71], although in general the H.A.Z. properties were higher than those of the parent plate. Peterson[72] reports increases in Charpy v-notch impact resistance from 22 to 30 ft.lbs. for specimens thermally cycled to peak temperatures between 700°C and 1300°C. Only brief detail concerning the microstructures is given and

although some decrease in strength and toughness is reported these are considered to be of little practical significance. Alternatively, Duffey and Sutar[61] have found that in certain areas of the H.A.Z. the tensile properties could be up to 10% less than the parent plate. The fracture toughness measurements in this work were confined mainly to the weld metal, but investigations carried out at Bristol Aerojet Ltd indicate that fracture toughness variations do occur both in the parent plate and the H.A.Z.[73,74] and that catastrophic failures can result from reduced fracture toughness[75].

It would appear that the H.A.Z. problems arise in two distinct regions. Each has a different thermal history, experiences a different peak temperature and results in distinct structural features. In the high temperature region adjacent to the weld metal the problem appears to be related to constitutional liquation, whilst at peak temperatures of about 650°C the formation of reverted austenite affects the properties. The mechanisms behind these phenomena and their effects on properties will now be considered.

2.3.2.1 Constitutional liquation

Constitutional liquation has been proposed as a mechanism that can result in microsegregation in the weld H.A.Z. of maraging steel by Pepe and Savage[76]. This work was designed to study the effects of constitutional liquation and indicates that it may produce structures susceptible to H.A.Z. hot cracking. The hypothesis of constitutional liquation has been confirmed experimentally. However, since

such work is unpublished Pepe and Savage include an explanation of the phenomenon which they consider can occur in any material consisting of a high melting point intermetallic compound distributed as a second phase in a solid matrix.

The phenomena can be explained by considering the heating of such an alloy at various rates. With slow rates of heating the second phase dissociates and diffuses into the adjacent material to form a high alloy content solid solution, which then diffuses into the matrix to produce a single phase homogeneous solid solution. Melting does not occur until the solidus temperature is reached. With rapid heating however, the high alloy content envelope formed around the second phase may not have time to diffuse away before the temperature reaches its melting point. Thus a liquid film forms around the remaining second phase particle at a temperature below the bulk solidus of the alloy. As grain size increases with rising temperature the moving grain boundaries intercept the liquid, which penetrates the boundaries forming films around the grains. Such penetration tends to arrest further grain growth until the liquid phase has had time to interact with the matrix to form a homogeneous solid solution. If sufficiently high thermal or applied stresses are imposed whilst the liquid phase exists, hot cracks will result, but even in the absence of stress the formation of brittle grain boundary films alone will subsequently prove detrimental in service.

Pepe and Savage[76] found this theory applied to maraging steel and constitutional liquation was the result of a reaction between titanium sulphide and the matrix. It was apparent in stressed and unstressed T.I.G. welds that

the amount observed increased as the heating and cooling rates increased. From thermal simulation studies they showed evidence of constitutional liquation in specimens heated to 1300°C and above in 2.2 secs and immediately quenched. At temperatures less than 1300°C, and in specimens held for sufficient time at 1300°C or above, constitutional liquation was not detected. Further work by Pepe and Savage[77] has shown that anomalous grain size distribution occurring in the H.A.Z. of the maraging steel welds previously studied[76] can be attributed to grain boundary pinning by a liquid film produced by constitutional liquation. Also, a "ghost" boundary structure was produced because of incomplete homogenisation of this film.

The ease of dissociation and rapid diffusion of interstitial solutes, such as carbon in Fe_3C makes constitutional liquation unlikely except with extremely rapid heating and cooling rates[76]. In the case of alloy carbides, or compounds involving substitutional solutes, lower rates of dissociation make constitutional liquation unavoidable except for welding conditions producing extremely slow heating and cooling rates. Krantz[78] substantiates this by reporting evidence of constitutional liquation surrounding M_6C carbides in a H.A.Z. in Hastalloy X. Similar behaviour has been reported by Owczarski et al[79] in other high temperature alloys.

The inclusions present in maraging steel have been identified by T. and E. Boniszewski[80] who suggest that titanium carbide networks present at prior austenite grain boundaries can be deleterious to fracture resistance. The effects of constitutional liquation on these and other

inclusions, and the mechanism that may result in grain boundary films have been considered by investigators at Bristol Aerojet Ltd.

Langstone[74], using thermal and mechanical simulation, detected constitutional liquation of titanium carbides at temperatures between 1100°C and 1200°C. At 1300°C the titanium carbides were taken completely into solution and constitutional liquation of Ti(CN) was detected. No evidence of titanium sulphide liquation was found, but the sulphur level in this steel was less than the specification maximum 0.010% whereas in the work of Pepe and Savage[76,77] sulphur levels of 0.010% and 0.024% were present. The fracture toughness of the thermally cycled specimens varied little with peak temperature and appeared to be unaffected by an applied stress of 0.2 tons/sq.in. However in all cases it was lower than in the parent material. Hot cracking was detected in elevated temperature tensile tests and at temperatures where liquid films were present a considerable drop in ductility was recorded.

Fracture toughness was reported to decrease as cooling rates decreased from temperatures where solution of titanium carbide had occurred. This was related to grain boundary precipitation of the titanium carbide. Increasing the cooling rate or introducing a small stress to induce precipitation within the grains reduced the amount of grain boundary precipitation and improved toughness. In a parallel investigation by Wildman[73] grain boundary networks were found in the H.A.Z. of welds produced under no external restraint. These networks were observed from the fusion line through the regions experiencing peak temperatures greater than

1000°C and were related directly to constitutional liquation of titanium sulphide and titanium carbide. It was shown that vacuum induction melted steels contained less inclusions and had better toughness, 102 ksi√in, than vacuum arc melted steels, 71 ksi√in. Groome[75] indicated that constitutional liquation of Ti(CN) produced grain boundary networks and reiterated the recommendation of Wildman to use vacuum induction melted steels.

2.3.2.2 Reverted austenite

The effects of this phase can best be discussed after its mechanism of formation has been considered. Allen and Early[81] investigated the decomposition of iron-nickel martensite, referred to as the low temperature b.c.c. phase α_2, in a binary 18% nickel iron alloy. They suggested that decomposition occurs by two distinct reactions:

(1) $\alpha_2 \rightarrow \gamma'$

(2) $\alpha_2 \rightarrow \alpha' + \gamma'$

where α' is a low nickel form of α_2 and γ' is a nickel rich form of the f.c.c. phase γ. Reaction (1) is a shear transformation, reversible on cooling, whilst reaction (2) is a diffusion transformation.

It has been suggested that similar reactions occur in maraging steel (5) and Sedriks and Craig[82] confirm this. The effect of temperature on the amount of metastable γ' sufficiently enriched to be retained at room temperature, as well as the total austenite content was studied using x-ray diffraction techniques and the results are shown in Fig. 2.16. These are explained in terms of the reactions proposed previously[81]. Up to 650°C reaction (2)

Fig. 2.16. Variation of volume % of austenite with temperature; double lines indicate scatter of experimental results (after Sedriks and Craig[82]).

predominates. At higher temperatures the proportion of α_2 consumed by reaction (1) increases with temperature, and in addition re-homogenisation, as proposed by Decker[83], of γ' to the unstable γ takes place. Both factors reduce the amount of γ' detected at room temperature. It is also recorded that the temperature at which reaction (2) starts varies between 600°C and 650°C depending on heating rates, and can be completely suppressed by heating rates in excess of 200°C per sec.

It has been shown by Salmon-Cox et al[84] that sufficient alloying element segregation may be present in maraging steel to produce reverted austenite during the normal ageing treatment. This appears as characteristic banding and is a consequence of the microsegregation of nickel, molybdenum and titanium which originates as interdendritic segregation during ingot solidification. Kenyon[68] records similar findings in maraging steel welds where reverted austenite pools were not present when examined in the as welded condition, but formed on ageing. Kenyon also shows that reverted austenite most readily forms if ageing is carried out at 650°C. In view of the above comments this would appear to be the combined effects of weld metal segregation and segregation by diffusion.

The implication of this in terms of welding is that the H.A.Z. regions experiencing a peak temperature of 650°C invariably contain reverted austenite. Heat treatment trials[4] have shown that this phase prevents satisfactory hardening but detailed information on its effect in the H.A.Z. is limited. Boniszewski et al[85] showed a hardness

peak in the H.A.Z. of maraging steel welded in the annealed condition coincident with the 650°C isotherm. This was related to rapid ageing that would be expected at this temperature. After subsequently ageing the complete weld no peak could be found. It was concluded that normal ageing was sufficient to fully restore the properties but no confirmatory mechanical tests were made. Saperstein et al[86] report that toughness deficiencies in the H.A.Z. of M.I.G. welds did not appear to be such a problem as in the weld metal. The results reported do not specify where in the H.A.Z. tests were made, but it is stated that "every effort was made to avoid the reverted austenite regions". As reported earlier, variations in properties have been recorded by several authors. In submerged arc weld H.A.Z.s up to 45% reverted austenite was detected and this resulted in decreased strength and increased toughness[71]. In other cases minor variations in structures and properties were considered of little practical significance[71] but not fully evaluated.

For detailed information of the effect of reverted austenite on properties it is necessary to consider work other than H.A.Z. studies. Kenyon[68] shows that during the fracture of maraging steel welds voids formed only in the reverted austenite. It appears that the austenite cracks preferentially because slip can take place in this phase at stresses too low to produce slip in the matrix. Tetelman[87] has pointed out that in such a two phase structure, the soft phase will deform preferentially and may reach its critical strain for fracture at an early

stage. Hence the soft phase cracks, forming a series of microcracks in a hard matrix. Kenyon[68] continues by altering the filler metal composition to produce welds relatively free from austenite, and in these welds the fracture toughness is increased. These observations appear to contrast with the suggestion proposed by Floreen[9], that a film of austenite around the strengthening precipitates would be very effective in preventing void formation and increasing toughness. Obviously the scale of the reverted austenite observed by Kenyon[68] is greater than that envisaged by Floreen[9], and this could account for any dual role reverted austenite might play.

Salmon Cox et al[84] have recorded variations in fracture toughness related to banding. The banded structure consisted of high and low alloy concentration and austenite. It was shown that for through thickness tests on plate, the fracture path deviated abruptly and that the bands appeared to act as crack arresters resulting in increased fracture toughness. For tests where the crack front was parallel to the rolling plane, fracture occurred along the bands, involving considerably less plastic deformation and having lower fracture toughness. These observations may have little relevance to H.A.Z. studies, but they serve to show the morphology of a phase can either increase or decrease fracture toughness. Clearly, there appears to be some difference of opinion as to the exact effect of reverted austenite on the weld H.A.Z. properties of maraging steel.

2.4 Weld Heat Affected Zone Studies

The weld H.A.Z. can be defined as that portion of the base metal which has not melted, but whose microstructure or properties have been altered by the heat of welding. Some ambiguity may arise from this definition when considering the region immediately adjacent to the weld metal which exhibits some melting, but is below the bulk solidus temperature. In general however, this region is also considered to be part of the H.A.Z.

The difficulty in producing a more accurate definition of the H.A.Z. is demonstrated by considering the variations that can occur in H.A.Z. parameters. If peak temperature is selected, it is apparent that a range will arise in any H.A.Z. However, the absolute values vary depending on the material being considered and the solid state reactions possible in that material. In steels, transformations to austenite on heating and ferrite, bainite or martensite on cooling must be considered as well as the effects of recrystallisation and tempering. In precipitation hardening alloys overageing or the resolution of aged structures might occur. For these reasons peak temperatures from 1500°C to 400°C might relate to the extremes of the H.A.Z. in steels, whilst in aluminium alloys the corresponding range would be from 700°C to less than 200°C.

The width of the H.A.Z., however defined, varies with such factors as the thermal properties of the plate, heat input and welding process. In electron beam welding the H.A.Z. width can be less than 0.1" whilst with submerged arc welds this can be 0.5" or more. However, in all cases

a wide range of structures and properties will be contained in this relatively small region constituting the H.A.Z.

The heating and cooling rates experienced in H.A.Z.s will also vary, and in general are much greater than those experienced in conventional heat treatments. These rates will be dependent on the factors that affect the peak temperature distribution and the H.A.Z. width. In electron beam welding the heat intensity of the source is very high and the heating and cooling rates encountered in the H.A.Z. are correspondingly high. The submerged arc welding process represents a low heat intensity source, and consequently the H.A.Z. heating and cooling rates are low. Since a number of factors affect the heating and cooling rates, the nature of the H.A.Z. thermal cycles is complex. However, analytical and numerical solutions have been developed that enable the effects of these factors to be determined. Hence detailed information can be obtained about the weld H.A.Z. thermal cycles.

During the thermalcycle the material in the H.A.Z. obviously undergoes thermal expansion and contraction. However, these effects are restrained by the surrounding unheated material and hence they produce in the material corresponding compression and tension effects. Since at elevated temperature the yield point invariably falls, this stress cycle is certain to lead to an associated strain cycle as local deformation occurs. These effects of stress changes persist in welded joints as residual plastic strain and well defined internal stress distributions. The latter are in fact well known as the residual stresses characteristic

of welded joints. The outcome of these effects is that the material in a weld H.A.Z. not only experiences a thermal cycle but an associated stress/strain cycle. In some materials where the solid state transformations are sensitive to deformation these effects could have a bearing on the subsequent microstructure and properties. Quantitative evaluation of stress and strain in the weld H.A.Z. is however a very complex problem and at the present time little information concerning the magnitude of the strains involved is available.

Having outlined the general features of the H.A.Z., the difficulties associated with mechanical and structural studies of this region and the techniques used to overcome this will now be considered. In addition, the theoretical aspects of heat flow in welding and the practical value of heat flow expressions will be reviewed.

2.4.1 Weld heat affected zone simulation

In a real weld H.A.Z., the amount of material undergoing a particular thermal cycle is very small. Consequently it is very difficult to carry out mechanical tests in the H.A.Z. that can be said to relate to one particular region. This limitation applies particularly to fracture toughness testing. As Saperstein et al[86] record, in a real H.A.Z. crack propagation would not occur through a single microstructure region, but rather through a microstructural composite. A further difficulty is encountered in locating cracks in such specimens. As a result of these limitations some scatter in results from real H.A.Z. tests is to be expected, and their significance may be limited.

To overcome these problems, and gain more precise information of the effects of welding on the H.A.Z. properties of materials it is necessary to reproduce the thermal cycle uniformly in a specimen large enough for normal testing methods to be applied. A number of simulation techniques have been developed for this purpose, and these are reviewed by Widgery[88]. The principal feature involves generating the thermal cycle in a specimen by its own resistance to the passage of an electric current. In most cases the current is passed by conduction from water cooled copper grips, but other systems utilise inductive heating. Control of the thermal cycle is generally obtained by monitoring the specimen temperature with a thermocouple. The signal from this thermocouple is electronically compared with a reference generator, and the difference used to control the power applied to the specimen.

After simulation the properties and structures can be examined with precision. Developments have led to most simulators having mechanical testing facilities. Savage[89] discusses both the thermal cycling and straining equipment available on the "Gleeble" thermomechanical simulator. With such facilities not only thermal simulation but also strain cycling, transformation studies and hot ductility tests can be performed[88].

Thermal simulation was used by Pepe and Savage[76] in their constitutional liquation study in maraging steel. Many of their tests involved quenching to retain evidence of high temperature structures, and full thermal cycles were not always used. Nevertheless, the results indicated that

the microstructural features of a real weld H.A.Z. could be accurately reproduced by thermal simulation. Later work by the same authors[77] again established this point. However, in both cases only one particular region of the H.A.Z. was studied, and no comparison was made between other structures or real and simulated H.A.Z. properties.

Smith et al[90] have adopted a simulation technique to study the weld H.A.Z. structure and properties of two mild steels. Direct comparison is made between the microstructures observed in four regions of the real weld H.A.Z. and those produced in simulation. Good agreement is found in all cases, but although the tensile and impact properties of the simulated H.A.Z. are determined, no attempt is made to determine the properties of the corresponding real weld H.A.Z.s. A similar situation arises in later work by Smith et al[91] involving the simulation of weld H.A.Z.s in low alloy steels. Again good correlation is obtained between real and thermally simulated H.A.Z. microstructures, but assessment of the mechanical properties is based only on the simulated H.A.Z. The lack of real weld H.A.Z. properties in these investigations is obviously a reflection of the difficulty that simulation techniques are designed to overcome, namely that the size of a real weld H.A.Z. limits the accuracy of mechanical property determination. Even so, some attempt to measure real H.A.Z. properties seems necessary to validate the simulation approach.

An objection to H.A.Z. simulation using thermal cycling alone arises from the possible effects of strain. Measurements of strain and strain cycles in the H.A.Z. are

difficult, but Cargill[92] has shown that strains up to 2% might be expected in fillet welds. The degree of straining in the H.A.Z. during welding and in specimens during simulation may differ, but whether this is significant is debatable. Hrivnak[93] reports that in real weld H.A.Z.s of mild and alloy steels strain increases the dislocation density, and suggests that it is therefore necessary to superimpose strain cycles on thermal cycles in simulation. In materials of low dislocation density such as Hrivnak studied, this may have some effect, but with materials of high dislocation density it is probably less significant. In agreement with this, the work of Watkins et al[94] and Smith et al[90] has shown that varying strain in thermally simulated specimens has little effect on impact properties.

In the work of Pepe and Savage[76,77] and Smith et al[90] temperature gradients were known to exist in the specimens. In one case they were ignored[90], whilst in the others[76,77] the structure at a particular position with respect to the control thermocouple was taken as representative for each specimen. This lack of precise data concerning the temperature distribution is very surprising since the whole basis of the simulation approach is that the thermal history of the specimen is known and accurately controlled. Although Pepe and Savage have accurate records of the temperature in the vicinity of the thermocouple, they present no details of other areas.

The temperature discrepancies mentioned have in general been detected as a result of microstructural comparisons between real and simulated cases, rather than as a direct

result of temperature calibration. Hrivnak has shown[93] that to produce a real H.A.Z. structure by simulation of the thermal cycle it was necessary to alter the peak temperature simulated, but no assessment of the reasons for this is given. However, Dolby and Widgery[95] having found a discrepancy between real and simulated H.A.Z. microstructures devoted considerable attention to this problem.

The primary difference found was that the austenite grain size produced during simulation was greater than the corresponding real situation. It was estimated that thermal cycling to a measured peak temperature of 1210°C would produce an austenite grain size equivalent to a real weld HA.Z. temperature of 1340°C. Two factors were considered to account for this discrepancy. It was shown that errors arise in temperature measurement because temperature gradients exist across the thermocouple bead. The recorded peak temperature could be up to 60°C lower than the true specimen temperature at about 1340°C as a result of this error. Also, considerable scatter was found in temperature measurements from control thermocouples resistance welded to the specimens, and an improved technique of making and attaching thermocouples was considered necessary. It was suggested that the remaining temperature/grain size difference could be explained on the basis that grain growth is restricted in a real weld H.A.Z. because of the temperature gradient, but in the simulated case the restriction is less.

Thermal cycling to an indicated peak temperature of 1210°C reproduced a structure appropriate to a real weld H.A.Z. peak temperature of 1340°C, but at an indicated peak

temperature of 900°C the structure was equivalent to that at the same real weld H.A.Z. peak temperature. Whilst the authors accept that the specimen would still be at a higher temperature than indicated, they consider that the difference had no significant effect on grain size. Although this may be so in this context, the possible temperature error arising at 900°C or even lower may be of considerable significance for example in hot ductility testing. Consequently a fuller analysis of the temperature discrepancy is essential.

As a continuation of the previous work, Dolby[96] compared the fracture toughness and microstructure of a real weld H.A.Z. with those of a thermally simulated H.A.Z. in a low alloy steel. Good correlation between properties and microstructure was found provided the necessary steps were taken concerning temperature control. This work further justifies the simulation approach, but indicates that care must be taken particularly over temperature control.

2.4.2 Theoretical heat flow relationships

The temperature distribution in the heat affected zone of a welded plate is dependent upon many factors such as the welding process and parameters used, and the plate dimensions and physical properties. For any H.A.Z. study it would be ideal to have experimental values of the temperature distribution, but in many cases this is not practicable. However, with the use of heat flow equations and a knowledge of the parameters involved it is possible to calculate the peak temperature distributions and thermal cycles for any point in a weld H.A.Z. The derivation of heat flow equations relating to

the welding of thin plate will now be considered as well as their practical verification and usefulness.

The differential equation of heat flow in a homogeneous isotropic solid in terms of rectangular co-ordinates (x, y, z) is

$$\frac{\partial T}{\partial t} = \frac{K}{\rho c}\left(\frac{\partial^2 T}{\partial x^2} + \frac{\partial^2 T}{\partial y^2} + \frac{\partial^2 T}{\partial z^2}\right) \qquad \ldots\ 2.18$$

where T = temperature increase of the solid

t = time

K = thermal conductivity of the solid

ρ = density of the solid

c = specific heat of the solid.

$K/\rho c$ has been defined as α, the thermal diffusivity. The above equation cannot be applied directly to welding because it applies to steady state conditions. To overcome this, it is necessary to consider the existance of a quasi-stationary state. Rosenthal[97,98] adopts this approach, and states that the quasi-stationary state exists in a plate when the temperature distribution relative to the heat source is stationary. To account for this state in equation 2.18 it is necessary to transfer the origin of the co-ordinates from the plate to the heat source. If x is parallel to the welding direction, the new co-ordinate ξ is given by

$$\xi = x - vt$$

where v is the welding speed. Also the derivative with respect to time, $\partial T/\partial t$, becomes zero, and so the quasi-stationary state of welding is given by

$$\frac{\delta^2 T}{\delta \xi^2} + \frac{\delta^2 T}{\delta y^2} + \frac{\delta^2 T}{\delta z^2} = -2\lambda v \cdot \frac{\delta T}{\delta \xi} \qquad \ldots\ldots 2.19$$

where $\lambda = \frac{1}{2}\alpha$.

To apply this equation to welding situations it is necessary to make the following assumptions.

1. The heat source is concentrated as a point.
2. Heat losses to the atmosphere can be neglected with respect to heat flow in the plate.
3. No heat is generated by the Joule effect.
4. The plate is wide enough to be considered infinite.
5. The plate remains solid and no phase changes occur.
6. The physical coefficients, K, ρ, c, remain constant.

The justification of these assumptions is not that they are accurately realistic, but that they enable useful equations to be derived. The solutions to the heat flow equation for different boundary conditions are covered in detail both by Rosenthal and Myers et al[99] who adopt the use of dimensionless parameters. For the purposes of this review, only Rosenthal's solution to the two dimensional case will be considered.

For 2D heat flow, the plate is considered to be infinite in the ξ and y directions but thin and of thickness g in the z direction. Also, there must be no change in temperature with respect to thickness at any point in the plate. Rosenthal, by substitution of these boundary conditions into equation 2.19, has produced the following temperature distribution equation:

$$(T - T_o) = \frac{Q_o}{2\pi K} \cdot e^{-\lambda v \xi} \cdot K_o(\lambda v r) \quad \ldots\ldots 2.20$$

where T = temperature of interest in the plate

T_o = original plate temperature

Q_o = heat input per unit plate thickness

K_o = modified Bessel function, second kind zero order

and $r = (\xi^2 + y^2)^{\frac{1}{2}}$.

The relationship between temperature, welding parameters and co-ordinates is shown in Fig.2.17. This expression applies to the welding situation where a full penetration weld is achieved in one pass. This generally arises in thin plates, and the heat source is considered to be a line of length g, the plate thickness. By making the appropriate substitutions this equation can be used to calculate the shape of the isotherms around a moving heat source, as well as the peak temperature distribution and thermal cycles in any weld H.A.Z.

2.4.3 Practical use of heat flow relationships

The majority of work carried out in this area has been concerned with obtaining theoretical information, such as the thermal cycle, and correlating this with experimental results. Rosenthal[98] has compared theoretical cooling rates with those measured by Hess et al[100] in steel and shown fairly good agreement for a wide variety of plate thickness, temperature range and welding conditions. Wells[101] simplified the 2D heat flow equation to give

$$Q_o = 8KT\left(\frac{1}{5} + \frac{Vd}{4\alpha}\right) \quad \ldots\ldots 2.21$$

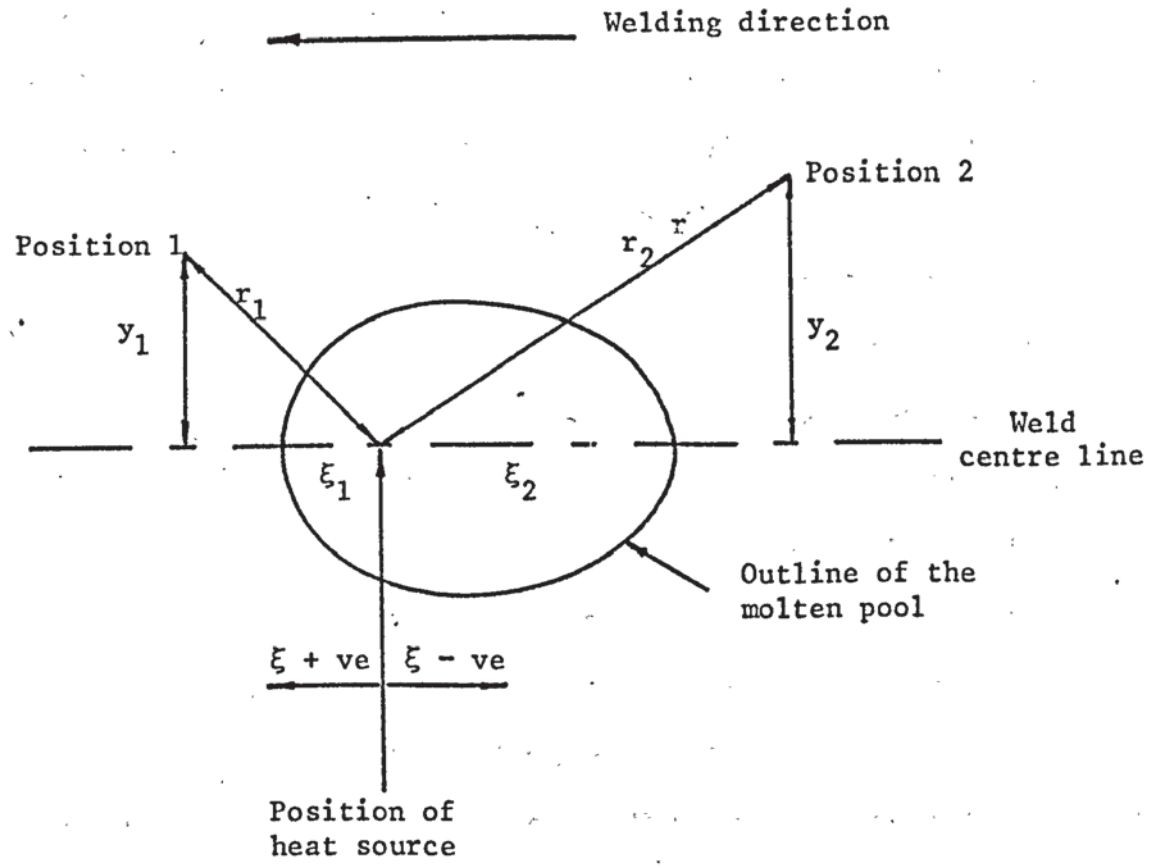

Fig. 2.17. The relationship between the weld H.A.Z. position and the co-ordinates ξ, y and r used in Rosenthal's two dimensional heat flow equation.

where d is either the fused bead width or the width of an isotherm of interest. Wells shows that the non-dimensional term $Vd/4\alpha$ is characteristic of the weld. Values less than 0.1 indicate relatively low cooling rates but distortion might be expected to be large. Values greater than 1 reflect low distortion but high cooling rates. Comparisons between experimental and theoretical isotherm spacings showed reasonable agreement in this work.

For accurate comparisons it is necessary to experiments on plates large enough to be considered infinite. Roberts and Wells[102] considered this using a mathematical approach. They found that a test plate should have a half-width of ten or more fused bead widths to approximate to infinite width. In terms of length, if again ten fused bead widths are ignored at each end then the remaining points can be regarded as in a plate of infinite length.

Apps and Milner[103] extended the Wells approach[101] to a study of several materials and general agreement was found for the fused bead width-heat input relationship. However, for improved correlation between real and theoretical values a latent heat term was added. This was found to be particularly effective for high conductivity metals. Christensen et al[104] have made an extensive study of the three dimensional situation in mild steel and aluminium. In general fused bead width predictions agreed with experiment, but variable H.A.Z. correlation was found.

Ralph[105] adopted Rosenthals two dimensional heat flow equation to predict thermal cycles. In H.A.Z. studies of welded copper-chrome, thermal cycles were computed from

welding parameters and used in simulation to study over-ageing effects. Adams[106] has considered the situation of welding hardenable steels where the possibility of forming martensite in the H.A.Z. increases as the cooling rate increases. Since the highest cooling rates are experienced at the centre line, Adams shows that a study of this region is advantageous. A number of approximations are introduced to improve correlation with experimental findings, and both peak temperature distributions and intermediate heat flow conditions are considered. More recently, Pavelic et al[107] have studied the two dimensional heat flow associated with T.I.G. welding of thin plates. By first predicting the weld pool shape, then using this as a boundary condition for finite difference analysis, extremely accurate peak temperature predictions were made.

Myers et al[99] have reviewed many of the comparisons between theory and experiment. They show that the temperature distribution in plates has received considerable attention. Comparison of thermal cycles indicate that close to the fusion line experimental curves are steeper, whilst at moderate distances from the fusion line better agreement is obtained. In general, reasonable predictions of the H.A.Z. widths can also be made. It would appear that although heat flow theory is not accurate in all cases, it can give acceptable agreement particularly for steels. In such a situation, heat flow theory can usefully indicate the range of thermal cycles, and account for the effects produced by altering the plate and welding variables.

3. EXPERIMENTAL PROCEDURE AND RESULTS

3.1 Assessment of Parent Material

The material for this investigation was supplied as $\frac{1}{4}$" thick plate by Bristol Aerojet Ltd. It was vacuum induction melted and the ingot homogenised at 1250°C for ten hours. The plate was produced by forging to slab, rolling to its full width then cross rolled to its final thickness. Forging and rolling were carried out between 950°C and 1100°C and the plate was given a final solution anneal of one hour at 820°C. The nominal and plate analyses are given in Table 3.1. The standard ageing treatment for maraging steels of three hours at 485°C was used throughout this investigation.

Metallographic specimens were prepared from as received and aged sections using conventional techniques. Repeated polishing and etching in 10% nital was found most suitable to reveal the structures. A Widmanstatten type structure was found in the solution treated material and a darker more diffuse structure in the aged material. These are typical maraging steel martensitic structures and sections parallel to the rolling plane are shown in Fig. 3.1. Sections taken at right angles to the rolling plane revealed banding, again a feature typical of maraging steel. In the solution treated condition an average hardness of 320 Hv was found that increased after ageing to 590 Hv.

3.1.1 Identification of inclusions

Before attempting to study the effects of constitutional liquation it was considered necessary to identify the inclusions present. In the solution treated material two

Table 3.1. The nominal specification for 18% Ni maraging steel (74) and the parent material analysis.

(a) As received.

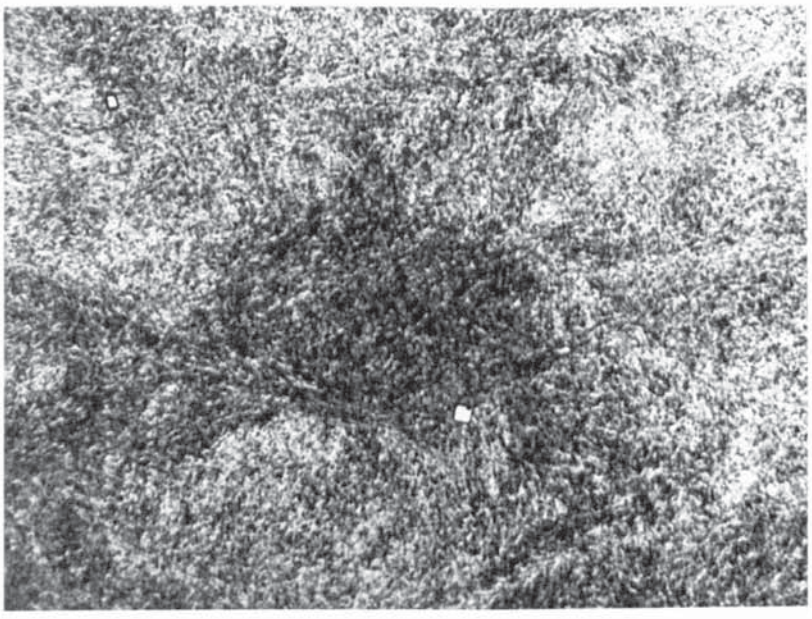

(b) Aged, 3 hrs at 485°C.

Fig. 3.1. Martensitic microstructures of the parent material. Etchant 10% Nital. x 500.

main types were observed: pink tinted cuboids generally present singularly or in pairs, and grey angular and elongated rod-like inclusions, often fractured and present in groups. Examples of these are shown in Fig. 3.2. The material was relatively clean and a normal quantimet inclusion count did not give a meaningful result.

The appearance of the inclusions described was unaffected by ageing, but examination of aged structures in the etched condition revealed small white globular and ribbon-like regions dispersed throughout the structure as shown in Fig. 3.2(c). Comparison of these observations with published work[80] indicates that the cuboids are titanium carbonitrides and the grey inclusions are titanium sulphide. The white etching regions may be titanium carbides, or possibly regions of reverted austenite formed during ageing[84].

To confirm the suspected identity of the inclusions, electron probe microanalysis and electron microscopy techniques were used. Fig. 3.3 contains an optical micrograph of a group of inclusions and the corresponding microanalyser images. These results indicate that the cuboids in the top right hand corner of the field contain titanium whilst the remaining inclusions contain titanium and sulphur. The white regions shown in Fig. 3.2(c) were too small to be detected or analysed, and since a light element kit was not available on the Cambridge microanalyser used, carbon and nitrogen could not be traced.

Carbon extraction replicas were prepared from the parent material and selected area electron diffraction

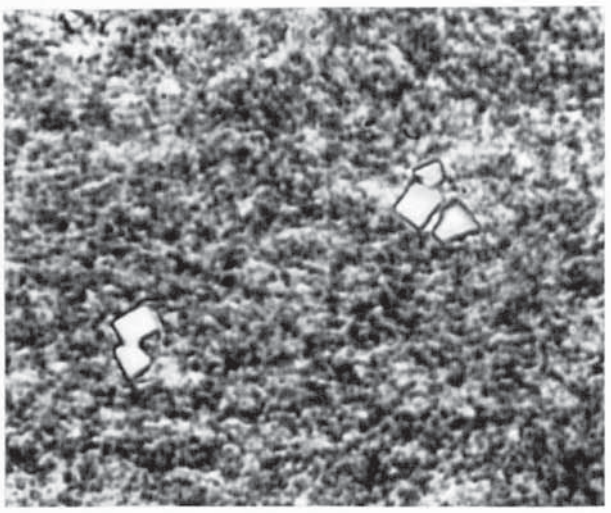

(a) Ti(CN)

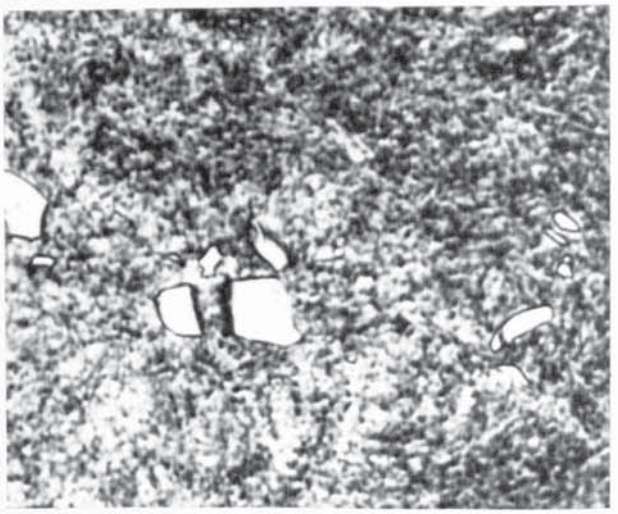

(b) Ti_2S

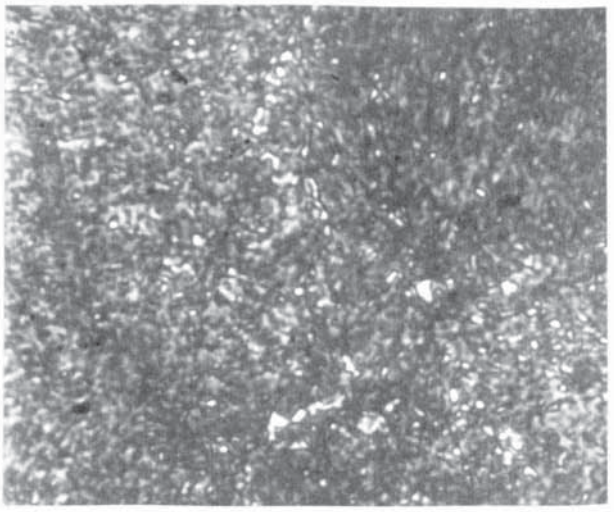

(c) TiC
or reverted
austenite.

Fig. 3.2. The inclusions present in the aged microstructure and their probable identities. x 1000.

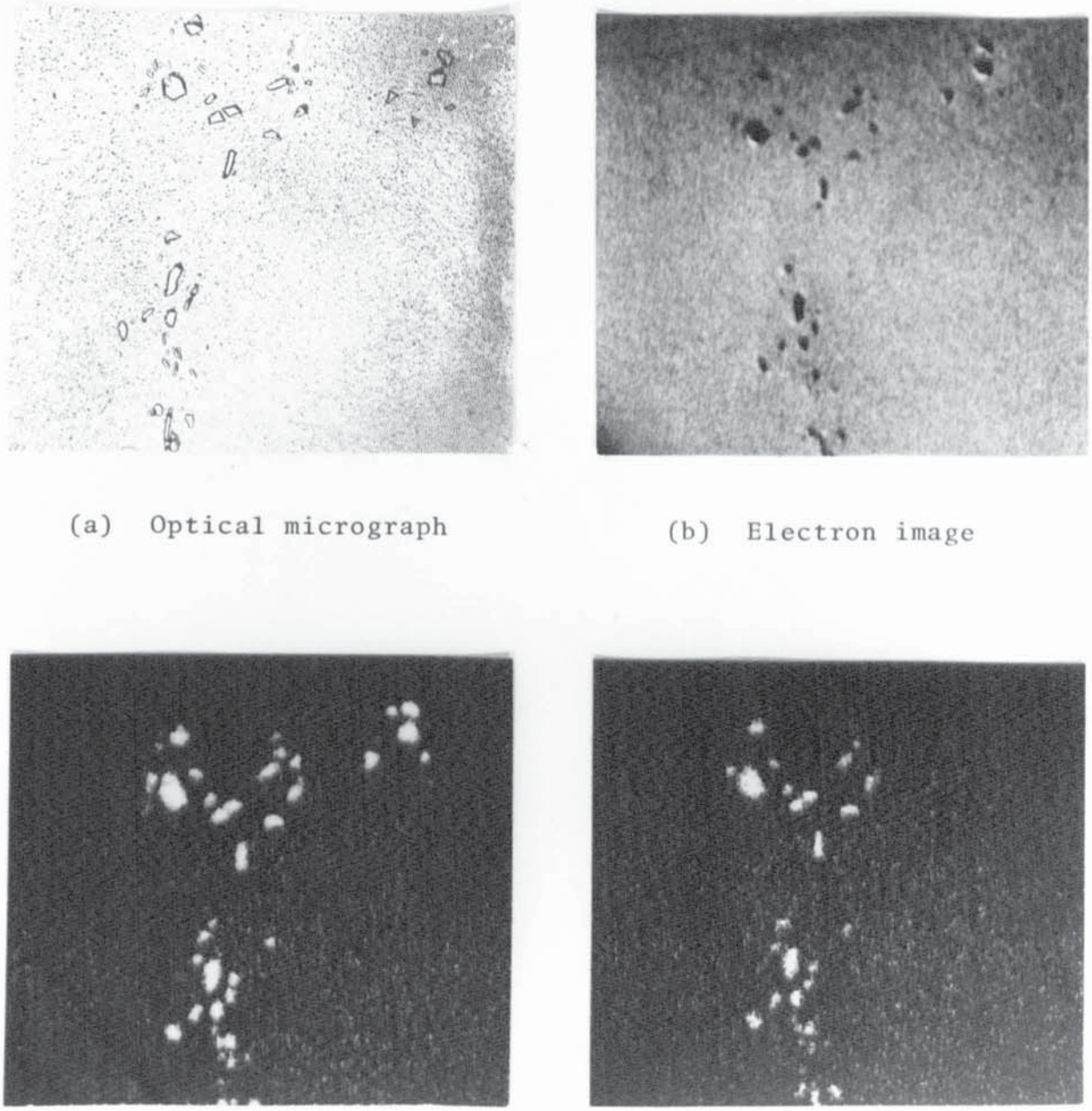

(a) Optical micrograph

(b) Electron image

(c) Titanium

(d) Sulphur

Fig. 3.3. Optical, electron and X-ray images of a group of inclusions in the parent material. x 350.

analysis carried out on the extracted inclusions using an AEI EM 6G electron microscope. Some difficulty was experienced in extracting the inclusions from polished specimens but they were relatively free and consequently easier to extract from the fracture surfaces. A number of replicas were examined but only the cuboid, angular and rod-like types of inclusion could be detected. Typical examples of these as observed in the fracture surfaces using the scanning electron microscope are shown in Fig. 3.4. Single crystal patterns and concentric ring patterns were obtained, and from these the lattice spacing between planes, d, was calculated using the equation

$$d = \frac{\lambda L}{R} \qquad \ldots\ldots 3.1$$

where R is the radius of the spot or ring on the pattern and λL is the microscope constant. The results obtained from the angular inclusions corresponded with those from the elongated inclusions indicating they were of the same type. The results are given in Table 3.2, together with relevant ASTM powder data and confirm that the cuboids are Ti(CN) whilst the other inclusions are Ti_2S. There was no evidence of the small white etching areas on the extracted replicas, and in view of the low carbon content of the alloy and the quantity of this phase throughout the structure, it seems probable that these regions are reverted austenite.

The fracture toughness of the parent material will be considered in the next section after the specimen design and fracture toughness testing procedure have been described.

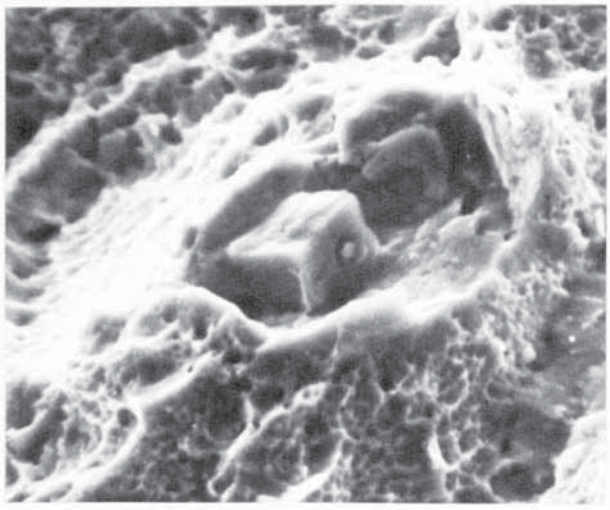

(a) Cuboid (Ti(CN)

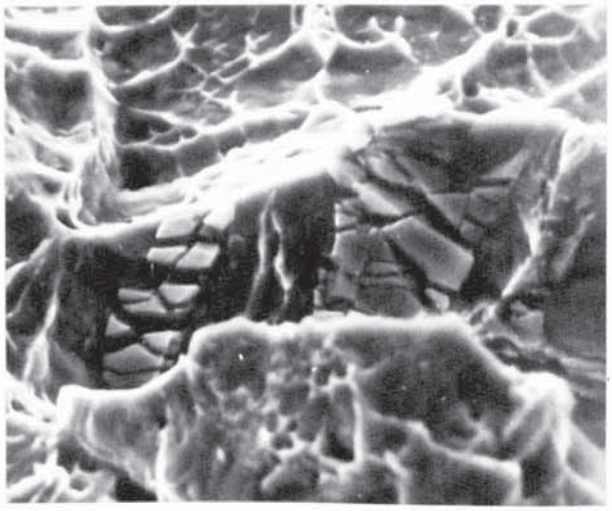

(b) Angular Ti_2S

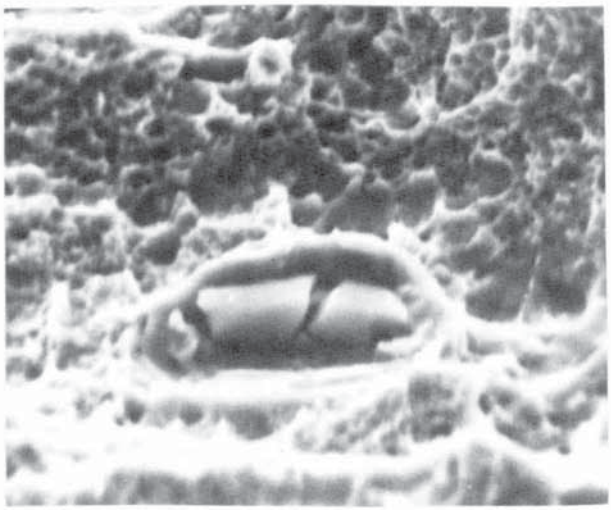

(c) Rod-like Ti_2S

Fig. 3.4. Scanning electron micrographs of the inclusions present in the fracture surfaces of parent material. x 2800

Lattice Spacings from Extracted Inclusions, Å		ASTM Data and File Nos		
Cuboids	Angular and elongated	TiC 6-0614	TiN 6-0642	Ti_2S 11-664
2.46	2.78	2.508	2.44	2.77
2.10	-	2.179	2.12	2.69
1.515	2.20	1.535	1.496	2.22
1.29	-	1.311	1.277	1.963
1.23	1.87	1.255	1.223	1.859
-	-	1.086	1.059	1.736
0.975	1.63	0.997	0.972	1.596
-	1.53	0.971	0.948	1.542
-	1.395	0.884	0.865	1.381

Table 3.2. Selected area electron diffraction results.

3.2 Fracture Toughness Testing

3.2.1 Specimen design

The types of specimens available for fracture toughness testing are fully described in the literature[33]. For the purposes of this investigation it was necessary to select a specimen that satisfied several requirements. The most important factor was that the specimen should be adaptable to thermal cycle simulation. Extensive metallographic and fractographic examination was envisaged and consequently taken into consideration in selecting the specimen design.

The most appropriate design appeared to be the single edge notch bend specimen. The basic features of this specimen are shown in Fig. 3.5, with all the dimensions relating to the width W which was maintained at 0.5" during this investigation. This specimen not only satisfies the requirements detailed above, but utilises a minimum amount of material and is relatively easy to machine. The omission of a chevron notch configuration and the use of attachable instead of integral knife edges further simplifies the machining required.

3.2.2 Testing procedure

A recommended practice for plane-strain fracture toughness testing of high strength materials has been prepared by Brown and Srawley[33]. Details of this practice applied to fatigue cracked bend specimens are contained in a BISRA open report[34]. This practice was adopted in all the testing carried out in this investigation, and the main stages will now be described.

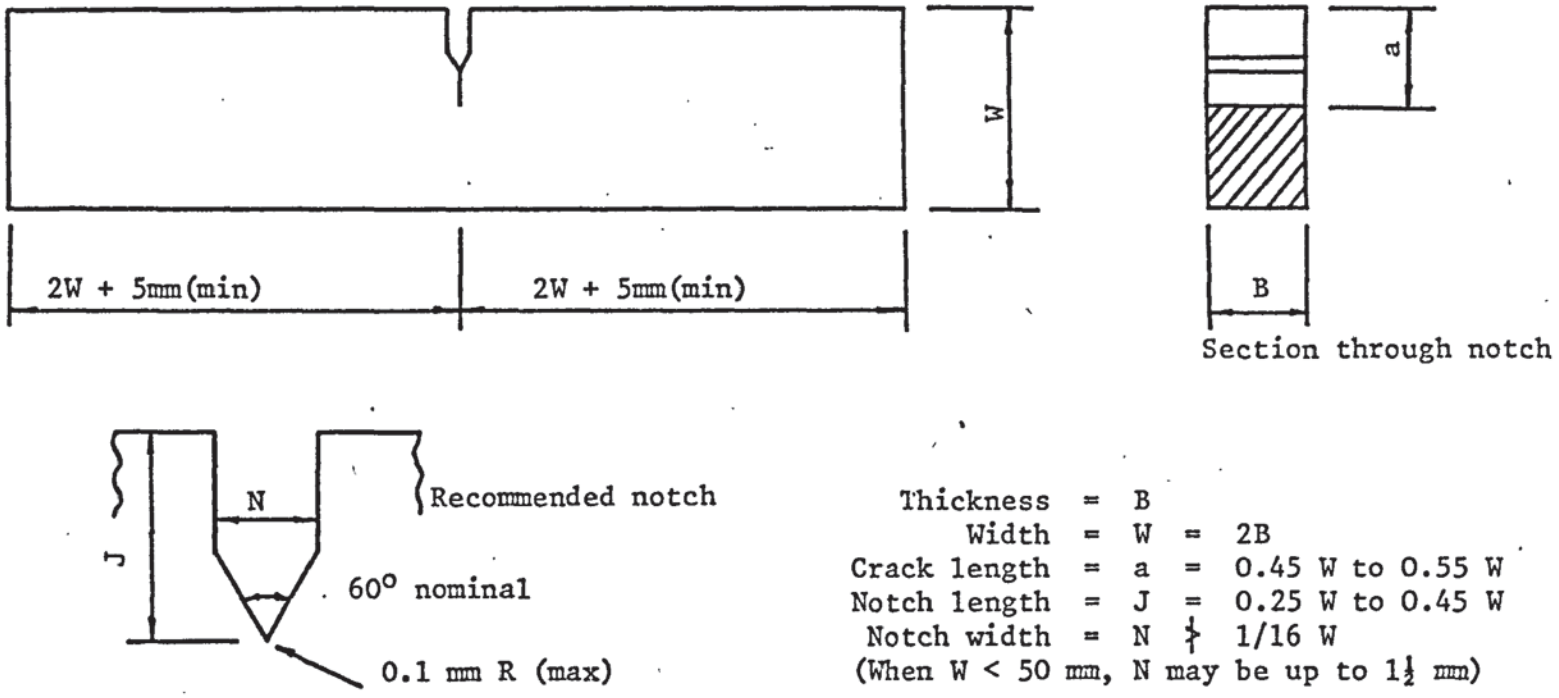

Fig. 3.5. Single edge notch bend specimen.

The radius ρ of a machined notch or crack has a great influence on the local stress produced at its tip. Decreasing ρ increases the level of local stress, but for every material there is a lower limit below which sharpening the crack has no effect because plastic flow causes immediate blunting. In measuring fracture toughness it is essential to produce a crack tip as sharp as a natural crack, otherwise anomalously high values of K_{Ic} are obtained because of the initiation problem. Suitably sharp cracks can be produced by pre-fatigue cracking a machined notch under low stress fatigue conditions.

Fatigue cracking was carried out on an Amsler High Frequency Vibrophore fatigue machine using a three point bending arrangement, as shown in Fig. 3.6. The mean and alternating loads were adjusted to initiate a fatigue crack from the root of the machined notch. Low power binoculars were used to monitor the fatigue crack growth, and the initiation conditions were maintained until the full crack length,"a" in Fig. 3.5, was about 0.2". The load conditions were then reduced such that a final 0.050" of fatigue crack propagated in greater than 50,000 cycles. This ensures that a sharp crack is produced, and gives a final crack length of the order of 0.250".

Fracture toughness testing was carried out in three point bending on and Instron universal testing machine. A double cantilever clip-in displacement gauge, positioned between attachable knife edges located either side of the machined notch, was used to record displacement during testing. The corresponding values of load were obtained

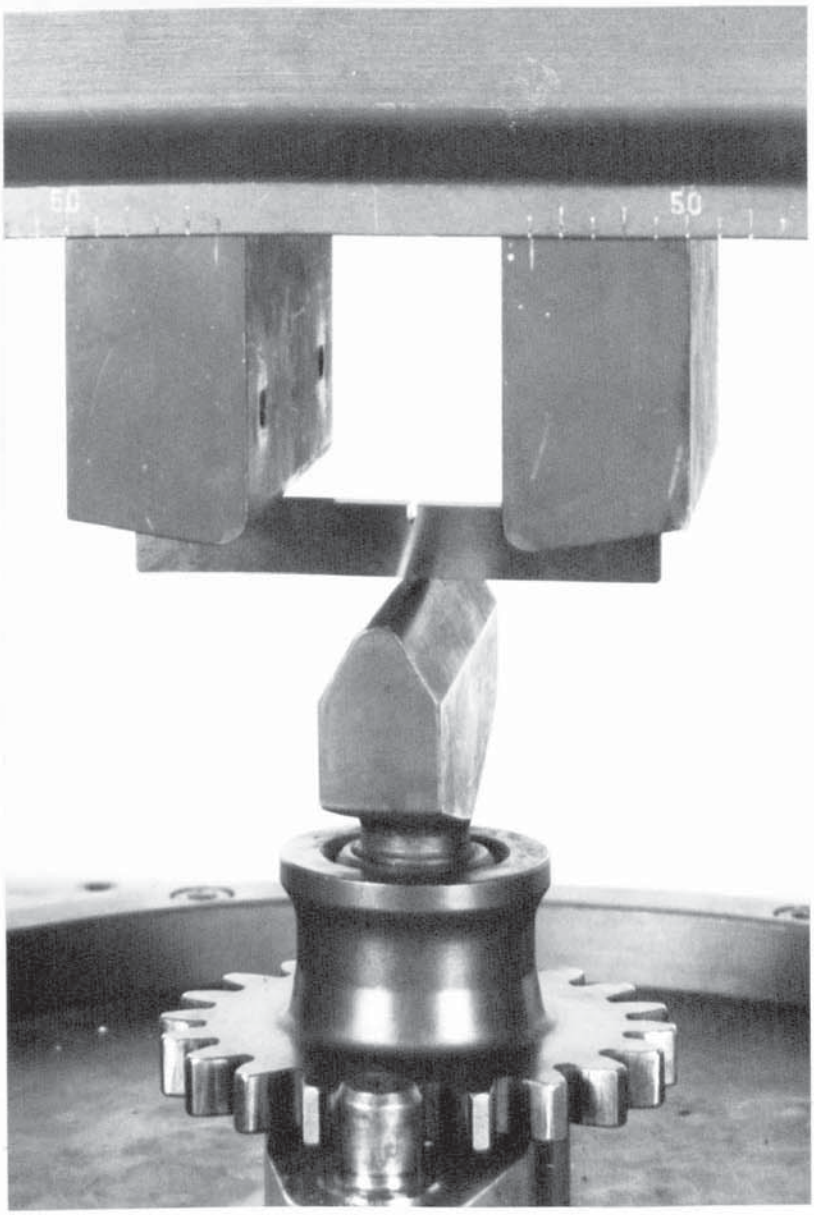

Fig. 3.6. The Amsler three point bending arrangement for fatigue cracking.

from the Instron's 5,000 Kg load cell. The linearity of the displacement gauge and calibration of the load cell were checked prior to testing. Testing was carried out at a crosshead speed of 0.02 cm/min. The displacement gauge output was fed through a Boulton Paul C.52 transducer amplifier to the X axis of a Bryans X-Y co-ordinate plotting table, whilst the load cell signal was fed to the Y-axis. The test record was then analysed to determine the critical load for fracture P_Q which was subsequently used to determine a conditional value of fracture toughness K_Q.

The general arrangement of the testing equipment is shown in Fig. 3.7 with detail of the specimen and displacement gauge shown in Fig. 3.8. To minimise the effects of friction during bending, which tend to increase the measured K_{Ic}, support rollers that can rotate apart are generally used. However, the size of the standard rollers and support pedestals were restrictive with the 2" span specimens used, and prevented attachment of the knife edges and displacement gauge. To overcome this it was necessary to use the fixed bending points taken from the Amsler fatigue machine. Friction effects are difficult to study in three point bending and there appears to be no satisfactory way of correcting for these effects[33]. However, since only small, relatively constant, movements occurred in the fracture toughness tests, the effects of friction were considered to be both small and constant throughout.

In the fracture toughness testing of some materials the fatigue crack extends by a rapid jump when the critical load is reached. This type of crack extension is referred to as "pop-in", and the load for pop-in is clearly defined

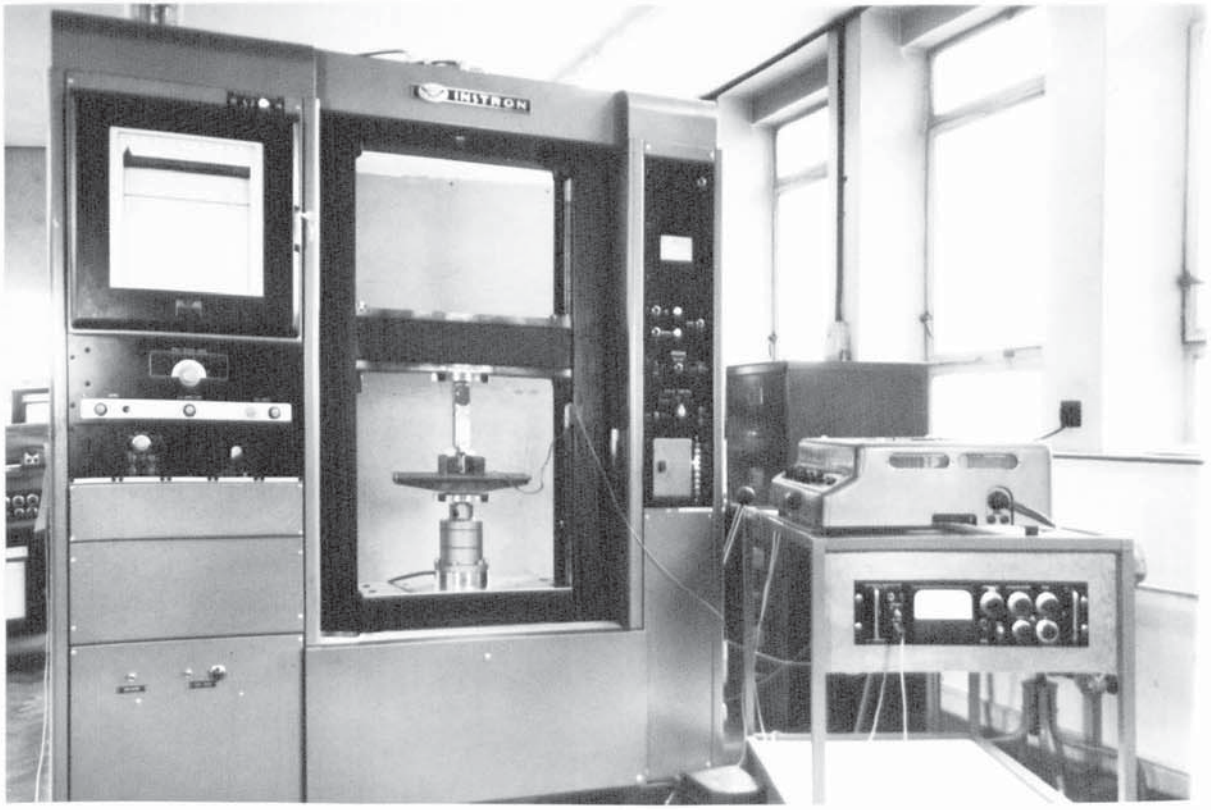

Fig. 3.7. The fracture toughness testing equipment showing the Instron, transducer amplifier and x-y plotter.

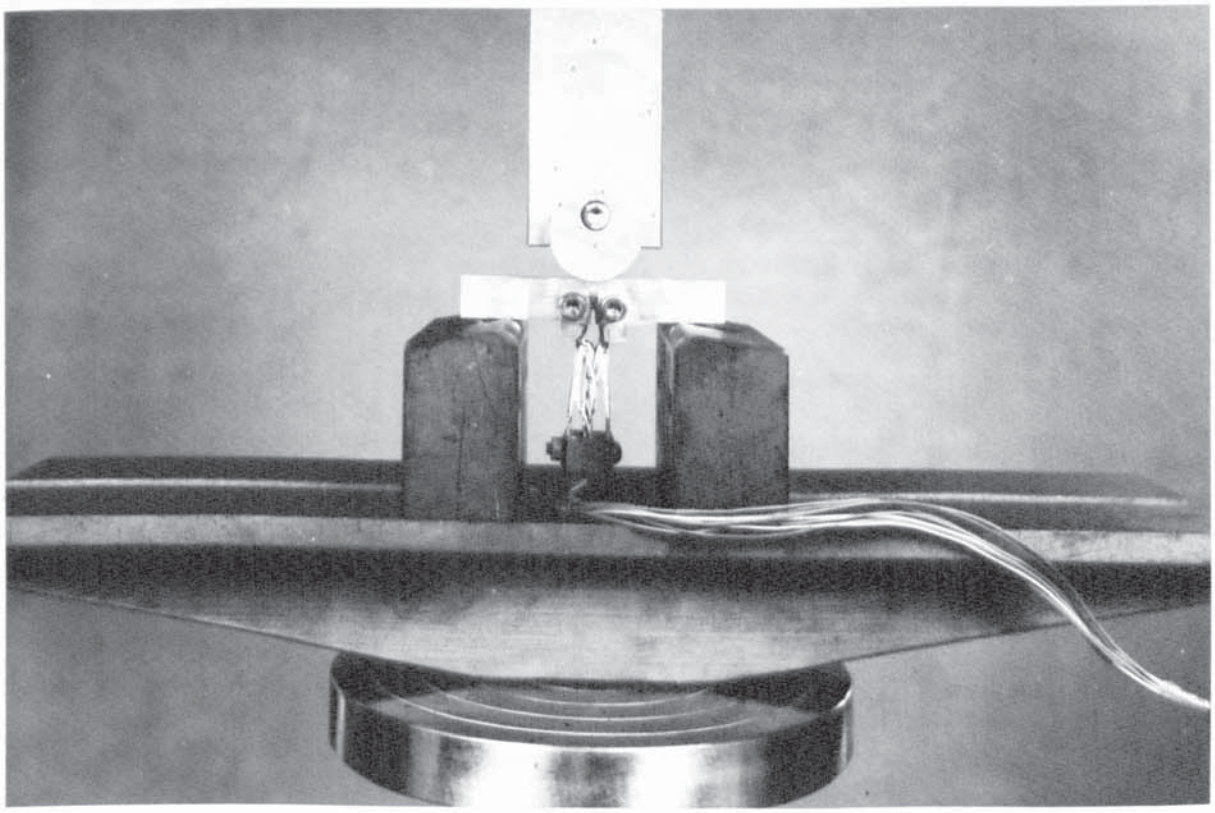

Fig. 3.8. Detail of a single edge notch bend specimen during testing showing the attachable knife edges and displacement gauge.

on the test record. In certain cases this occurs after crack extension by slow growth has taken place, and in other cases no distinct pop-in is observed. Consequently, the records for different materials vary, and to account for this an analytical treatment has been developed to determine the critical load in all cases. The deviation of the test record from linearity is regarded as though it were due entirely to crack extension, and the critical load determination is based on attaining a particular deviation. The appropriate deviation can vary for different specimens, but for bend specimens a secant line with a slope 5% less than the tangent to the initial part of the test record describes the requireddeviation.

Two types of test record were encountered in this investigation, shown schematically in Fig. 3.9, and were analysed as follows.

A secant line OP_5 was drawn through the origin with a slope 5% less than the tangent OA. P_5 is the load at the intersection of the secant with the record. If the load at every point preceding P_5 is lower than P_5, then P_Q is equal to P_5, Fig. 3.9, type I. If a maximum load precedes P_5 then this maximum load is P_Q, type II. To ensure the test is valid, further analysis of the test record is required. At a load equal to 0.8 P_5 the displacement x_1 along a horizontal line from the tangent OA to the record must not be greater than a quarter of the corresponding displacement at P_5.

To determine K_Q it is necessary to know not only P_Q, but also the initial crack length and the compliance

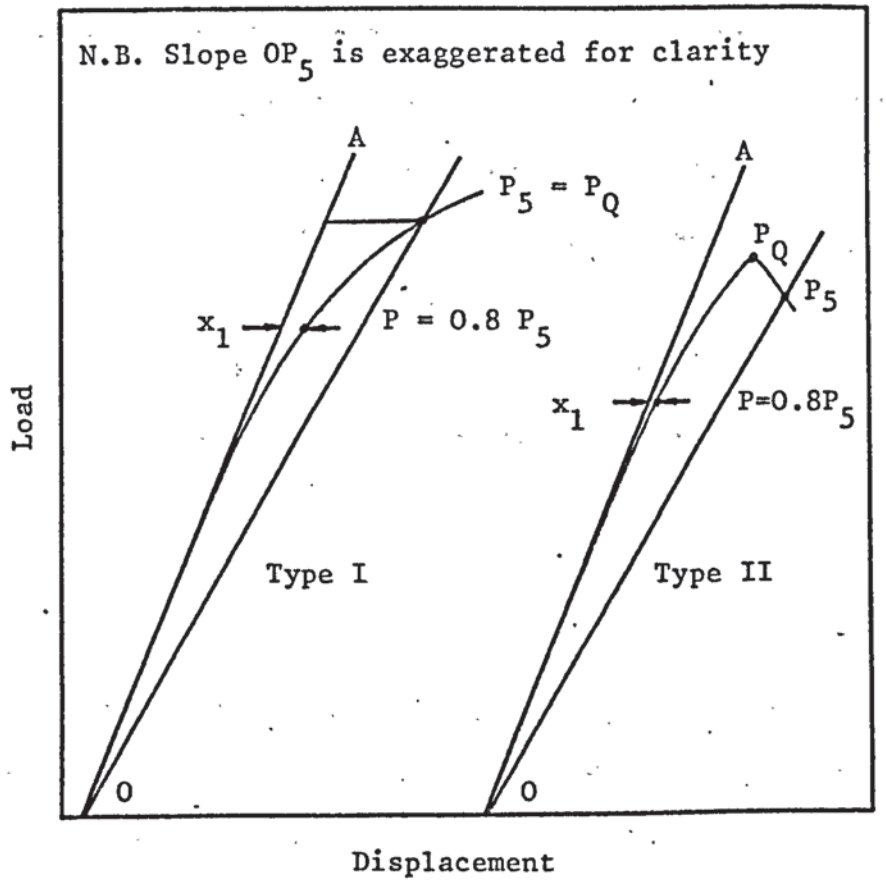

Fig. 3.9. Types of load-displacement records and their analyses.

function at a given $\frac{a}{W}$ for the particular test specimen geometry. The crack length, a, was determined from the fractured bend specimens using a travelling microscope, an average value being obtained by taking one quarter of the total of both surface measurements plus twice the maximum measurement. Values of the compliance or K function can be determined experimentally or by boundary collocation analysis. Walker and May[108] have adopted this latter approach and present tabulated values of compliance function against $\frac{a}{W}$ for a variety of specimen geometries. Using the tables for a single edge notch bend specimen loaded in three point bending with an overall span to width ratio of 4 : 1, values of K_Q were calculated as follows:

$$K_Q = \frac{YP_Q}{BW^{\frac{1}{2}}} \qquad \ldots\ldots 3.2$$

where Y is the compliance function.

To ensure that K_Q is the plane strain fracture toughness, the recommended practice states that

$$a \text{ and } B \geq 2.5\left(\frac{K_Q}{\sigma_{ys}}\right)^2 \qquad \ldots\ldots 3.3$$

In this investigation, tensile strength measurements were made using the Instron machine and No. 11 Hounsfield test pieces. Distinct yield points were not observed in the tensile tests and the limit of proportionality was taken as representing the yield stress. In all cases this value was close to the ultimate tensile stress. Having determined the corresponding values of K_Q and σ_{ys}, if equation 3.3 was

satisfied then the K_Q values were considered to be valid K_{Ic} results.

3.2.3 Parent material fracture toughness

Single edge notch bend specimens were machined transverse and parallel to the final rolling direction from random locations in the parent plate. The procedure adopted in all cases, unless otherwise stated, was to machine the specimens in the as received solution annealed condition, age using the standard treatment of three hours at 485°C, surface grind to final dimensions and pre-fatigue crack before bend testing. Tensile test pieces were machined from the fractured bend specimens.

The fracture toughness and corresponding tensile results are given in Tables 3.3 and 3.4 respectively and indicate that this material is a "300" grade maraging steel. The two groups of fracture toughness results were compared using the "F" test of variances and the students "t" test of means. The means of the longitudinal and transverse results were 54.7 ksi√in. and 54.2 ksi√in. respectively with corresponding standard deviations of 2.9 and 2.8 ksi√in. No statistical difference was found between these results. In all other tests specimens were taken from the transverse direction.

The minimum specimen thickness from which a valid K_{Ic} result can be obtained was calculated from the above data using equation 3.3 to be 0.085". The significance of this in terms of other experimental work was that specimens thinner than the standard design given in Fig. 3.5 might be useful in thermal cycle simulation if a limitation was found

Fracture Toughness ksi√in	
Longitudinal	Transverse
62.0	55.2
57.4	54.5
53.3	59.8
52.6	53.6
53.2	50.5
52.9	49.8
53.9	55.6
55.0	52.7
54.1	55.4
53.0	55.5
Mean: 54.7	54.2

Table.3.3. Longitudinal and transverse fracture toughness properties of aged parent plate.

Specimen	σ_{LP} ton/in^2	σ_{uts} tons/in^2	Elongation %	Redn. of Area %
Longt. 1	129	131	9	42
2	129	131	9	44
3	128	131	10	46
4	128	132	10	44
5	129	131	10	44
6	129	131	10	48
7	130	133	9	43
8	129	133	8	42
9	129	131	9	42
10	128	131	9	44
Mean	129	132	9	44
Trans. 1	130	135	9	42
2	129	133	8	43
3	129	131	10	46
4	129	131	9	42
5	129	135	10	44
6	130	133	9	44
7	129	131	8	43
8	128	131	9	45
9	130	131	10	46
10	129	135	8	40
Mean	129	133	9	44

Table 3.4. The longitudinal and transverse tensile properties of aged parent plate.

to be imposed on the upper heating and cooling rates attainable by the standard specimen geometry. Providing the thickness of such specimens was greater than 0.085", valid K_{Ic} results could still be evaluated. However, it has been shown[38] that with single edge notched tensile specimens of maraging steel, valid K_{Ic} results could be obtained from specimens even thinner then predicted by equation 3.3.

To clarify the position with respect to the material available for this investigation, a series of bend specimens of different thickness were tested and the average values from three tests at each thickness are presented graphically in Fig. 3.10. These results indicate that the plane strain, K_{Ic}, fracture toughness plateau reaches a limiting thickness of 0.150" below which valid K_{Ic} results cannot be obtained. From this value, to ensure K_Q is valid as K_{Ic}, the thickness criterion would need to be

$$B \geq 4 \left(\frac{K_Q}{\sigma_{ys}}\right)^2 \qquad \ldots\ldots 3.4$$

It is emphasized in the recommended practice[33] that the validity factor, 2.5 in equation 3.3, may vary from alloy to alloy. In general 2.5 has been considered more stringent than necessary, and as mentioned this has been shown from some tests on maraging steel[38]. Consequently, the results represented by equation 3.4 are neither in agreement with the recommended practice or with the generally expected trend.

This situation becomes more surprising when it is realised that the recommended practice is based on specimen

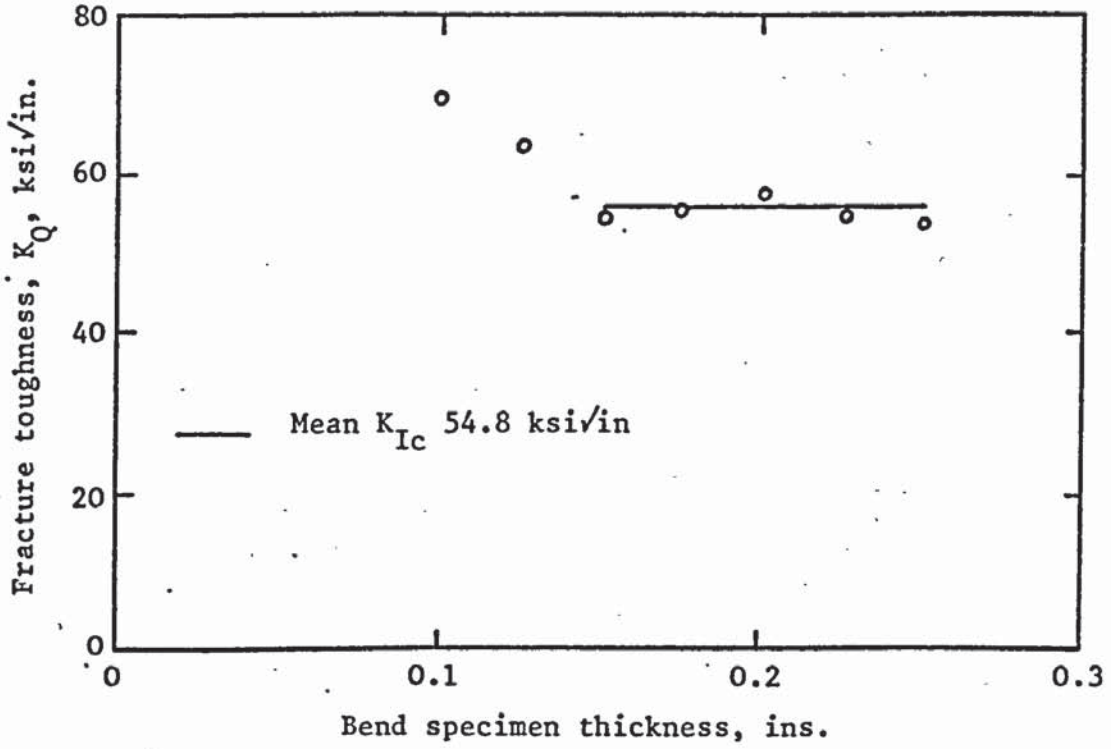

Fig. 3.10. The relationship between bend specimen thickness and fracture toughness.

size studies in various grades of maraging steel, including strength and toughness levels equivalent to the material being used in this investigation. However, close inspection of these particular results revealed that the thinnest specimens tested only confirmed that a validity factor of 3.5 was necessary, and the value of 2.5 was obtained from higher toughness, lower strength grades of maraging steel. A recent review of the developments in plane strain fracture toughness testing[114] presents results from a number of high strength materials. In some cases the recommended practice was shown to be conservative whilst in others it was considered only marginally sufficient. Finally however, the "tentative method of test" outlined in this publication included the same validity factor 2.5.

From the results of this investigation and published work it is apparent that the effects of thickness need further examination. For this investigation, if thermal cycling leads to a decrease in fracture toughness the established limiting thickness 0.150" may be considered as conservative. However, if fracture toughness increases it may be necessary to carry out further limiting thickness experiments.

3.3 Weld H.A.Z. Thermal Cycles

The thermal cycle experienced at a point in the H.A.Z. of a weld depends on the welding process and parameters involved in producing the weld. In this investigation numerous processes and parameters were selected in order to produce a comprehensive range of H.A.Z. thermal cycles. To overcome the difficulties in measuring H.A.Z. temperatures in the practical situation, the thermal cycles have been evaluated using Rosenthal's two-dimensional heat flow equation 2.20. Details of the computer programme, welding parameters and resulting thermal cycles will now be considered.

3.3.1 Computed thermal cycles

To obtain a complete thermal cycle from Rosenthal's equation it is necessary to evaluate the temperature for a number of positions, equivalent to increments of time. To do this for a range of parameters involves a large number of calculations. For this reason it was decided to programme a computer to generate the thermal cycles required.

Ralph[105] has prepared a programme in Elliot 803 Algol language based on Rosenthal's equation. This programme was not applicable to the present investigation for a number of reasons. Firstly it was designed to calculate the thermal cycles at any distance y parallel to the weld centre line, rather than the thermal cycles to particular H.A.Z. peak temperatures. Secondly it was found that the basic Bessel function formulae contained in Ralph's programme, involved two series expansions. As a result of this and the values of the maraging steel thermal constants involved, the

magnitudes of (λvr) and $K_o(\lambda vr)$ were such that ridiculous high and low temperatures were computed. Finally, the computing facilities changed since the Elliot 803 was replaced by an ICL 1905 A computer and this involves a change in the form of the Algol language. For these reasons it was decided to write a completely new computer programme.

A full print out of the new programme and details of the data input and printout are given in the Appendix, but the general form can be described with reference to the programme flow chart in Fig. 3.11. Once the computer has been programmed it accepts the input data and prints out the thermal and welding constants to be considered as a heading to each thermal cycle. To compute a thermal cycle having a particular peak temperature it is necessary to estimate the y distance corresponding to the peak temperature of interest. This has been achieved by utilising the simplified Well's equation 2.21[101],

$$q = 8KT\left(\frac{1}{5} + \frac{Vd}{4a}\right)$$

where d is the width of the isotherm of temperature T and equals 2y.

Having estimated the appropriate value of y, the next step is to select the Bessel function procedure best suited to the material being considered. Two alternatives have been written into the programme to make it applicable to any material. One alternative contains the full Bessel function formulae as contained in Ralph's programme. As a second choice it was necessary to include a formulae to

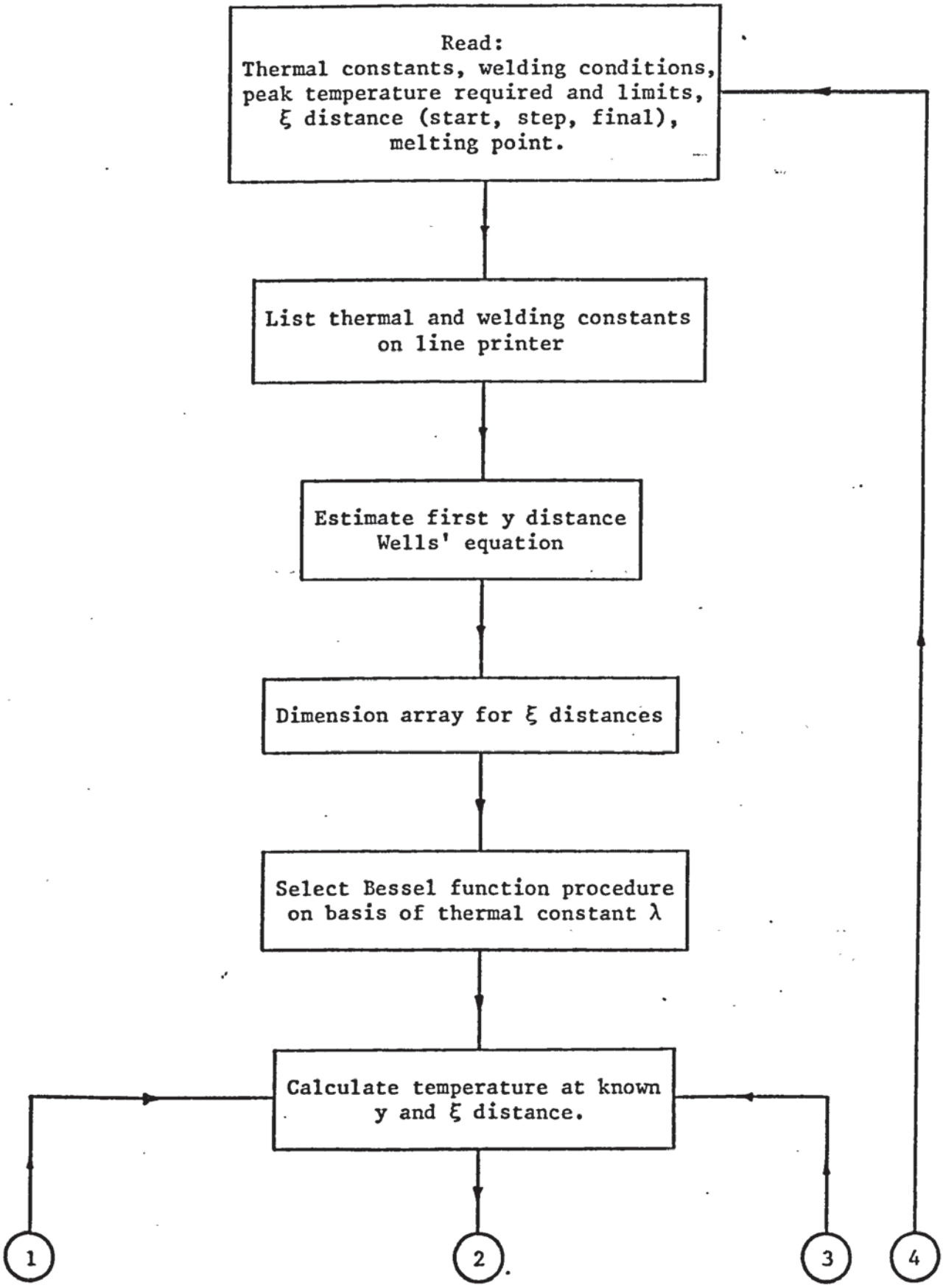

Fig. 3.11. Computer programme flow chart.

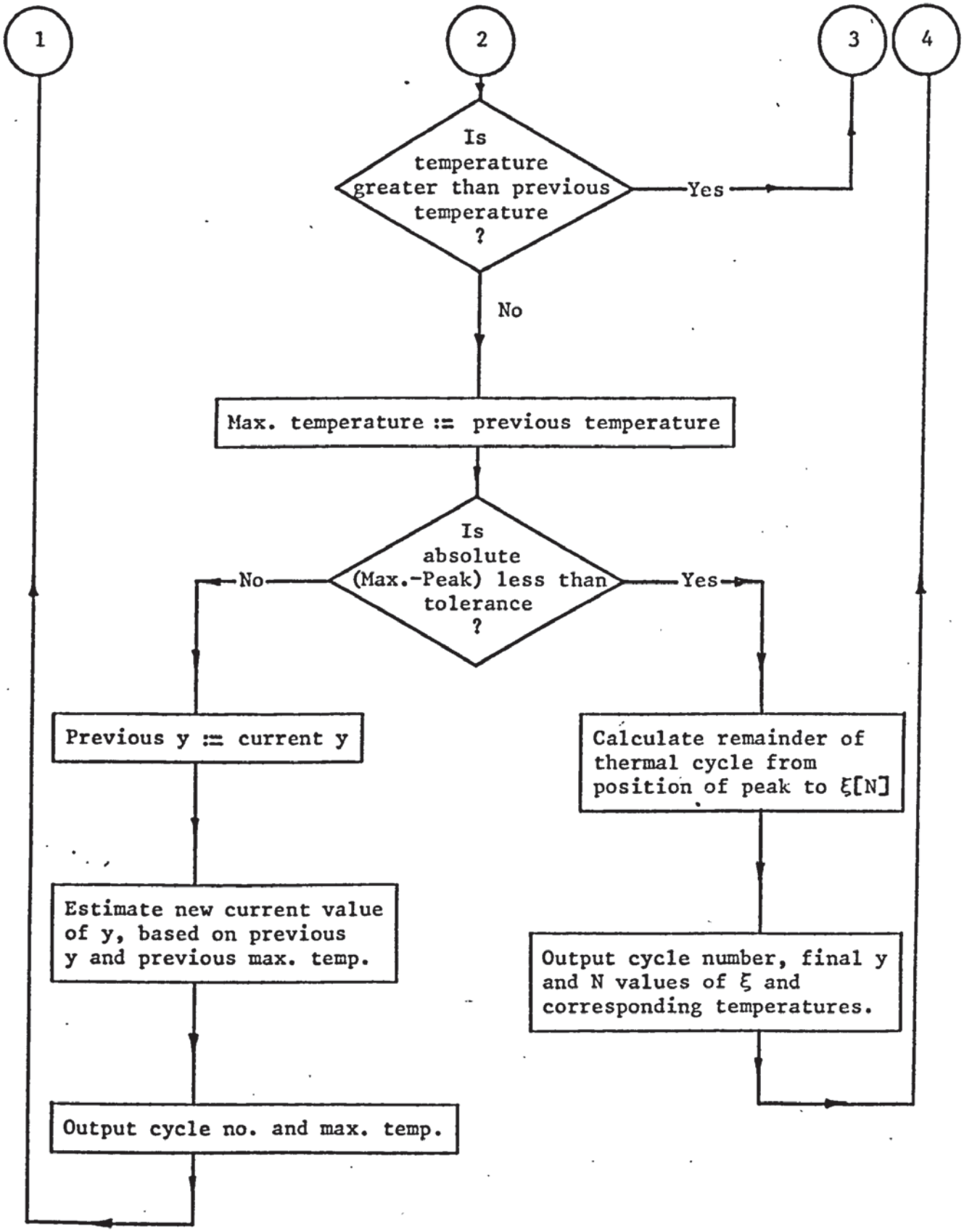

Fig. 3.11 (contd)

handle large values of the argument (λvr). Whittaker and Watson[109] and Roberts and Wells[102] both provide simplified formulae for this purpose. The results of thermal cycle calculations using these formulae were compared with those obtained using the full formulae for a range of (λvr) values that could be handled by both. It was found that the Whittaker and Watson formulae produced results very close to the full formulae results and consequently this was incorporated into the programme as the alternative Bessel function formulae. Either this or the full formulae is then selected by the computer on the basis of the value of λ. At present the deciding value has been set on the basis of a number of computations involving different materials at 3, and with λ below or above this value either the full or simplified formulae is selected respectively.

The thermal cycle calculation then proceeds until a peak temperature is reached. This is compared with the required peak temperature and if the difference is within the specified limits the full thermal cycle is computed and printed out. If the required limits are not satisfied, a new estimate of y is made based on the previous values of y and peak temperature, and a new thermal cycle calculated. This sequence is repeated until the required limits on the peak temperature are satisfied at which stage the full thermal cycle is computed and printed out. The programme is then designed to completely recycle and search for new data or end. Consequently, a whole series of thermal cycles to different peak temperatures can be readily calculated for one or many sets of welding parameters.

3.3.2 Welding parameters

Most of the conventional welding processes are used in practice to weld maraging steel. Experimental welding trials were carried out to determine the parameters for some processes, but a number were obtained from published data or by private communication. In all cases they were selected on the basis that they represent practical values that give full penetration welds in a single pass.

To satisfy the requirements of the Rosenthal equation, the heat input per unit thickness, Q_o, was calculated from the welding parameters using the equation

$$Q_o = \eta \frac{E.I}{4.18g} \qquad \ldots\ldots 3.5$$

where η - the arc efficiency

E - the welding voltage

I - the welding current

g - the material thickness

4.18 - joules equivalent.

Values of η for the microplasma and T.I.G. processes were determined using a simple calorimetry experiment. The values for M.I.G. and submerged arc welding processes were obtained from published data[104]. The electron beam process efficiency was assumed to be 100%, this being the value generally accepted and considered to be applicable for welds that just penetrate the plate thickness[110]. The maraging steel physical constants used in the thermal cycle calculations were also based on published data[111] and are given in Table 3.5. These values relate to a temperature of 100°C and although it is realised that they

Property	Symbol	Value	Units
Thermal conductivity	K	0.05	cals per (cm sec. ^{o}C)
Density	ρ	8.00	gms per cc.
Specific heat	C_p	0.101	cals per (gm ^{o}C)
Thermal diffusivity	α	0.062	sq.cm. per sec.
Lamda	λ	8.08	sec. per sq. cm

Table 3.5. Maraging steel physical constants

vary with temperature, this was the highest temperature for which published data were available.

The welding parameters and thermal constants were then used in conjunction with the computer programme to generate a series of thermal cycles to peak temperatures of 650°C and 1200°C. Although other peak temperatures were studied, these were selected initially as representative of the areas of particular interest. The heating and cooling rates associated with each set of welding variables were deduced from the computed thermal cycles. It was apparent that different combinations of heat input and welding speed resulted in very similar thermal cycles. In such cases only one of the set of conditions was used for thermal cycle simulation. Also, the cooling rates associated with a number of the welding parameters were such that they could not be simulated. Consequently these were deleted from the range of parameters to be studied. (Details of the limitations on cooling rate during simulation will be given later.) The welding parameters finally selected for simulation are given in Table 3.6 together with references where applicable. Throughout the tables of results the welding parameters will be referred to in terms of the process and numbers listed in this table.

In carbon steels the cooling rates associated with welding are particularly critical through the transformation temperature range. For this reason it is usual to quote H.A.Z. cooling rates for a temperature range of about 800°C to 500°C. With maraging steel no comparable range exists and consequently arbitrary ranges were chosen to

Welding Process		Ref.	η_0 %	Thickness cms	E volts	I amps	V cm/sec	Heat input cals/sec. cm thick
Micro plasma	1	-	45	0.165	20	29	0.250	384
	2	-	45	0.165	21	36	0.500	500
TIG	1	-	65	0.076	14	10	0.212	285
	2	-	65	0.076	38	12	0.424	926
	3	-	65	0.317	85	10	0.085	414
	4	-	65	0.317	210	12	0.508	1228
MIG	1	(112)	75	0.127	20	95	1.52	2690
	2	(112)	75	0.127	21	110	1.52	3260
	3	(112)	75	0.081	16	90	1.69	3180
Sub. Arc.		(62)	95	0.635	28	340	0.847	3400
Elect. beam		(110)	100	0.173	10,000	0.070	0.466	968

Table 3.6. Welding processes and parameters

indicate the heating and cooling rates to be studied. The average heating rates were determined from the peak temperature and total time of the heating cycle, and cooling rates were taken from the temperature drop over the first eight seconds of the cooling cycle. These values are given in Table 3.7 for the welding parameters to be simulated to peak temperatures of 650°C and 1200°C. Thermal cycles representative of the fast, intermediate and slow heating and cooling are given in Figs 3.12 and 3.13 for peak temperatures of 650°C and 1200°C respectively.

It can now be seen that the programme can be used to generate a range of thermal cycles representative of the weld H.A.Z.s produced in maraging steel by various welding processes. The availability of this data makes possible the simulation study of the weld H.A.Z. structures and properties.

Welding Process		650°C		1200°C	
		Heating rate	Cooling rate	Heating rate	Cooling rate
Micro plasma	1	80	14	180	65
	2	200	28	600	88
TIG	1	64	18	158	73
	2	60	6	260	42
	3	7	1	20	6
	4	50	4	230	36
MIG	1	140	10	660	56
	2	76	8	460	44
	3	98	9	570	52
Sub. arc.		22	2	140	13
Elect. beam		70	8	300	45

Table 3.7. The heating and cooling rates associated with different welding processes and thermal cycle peak temperatures, (°C per sec.)

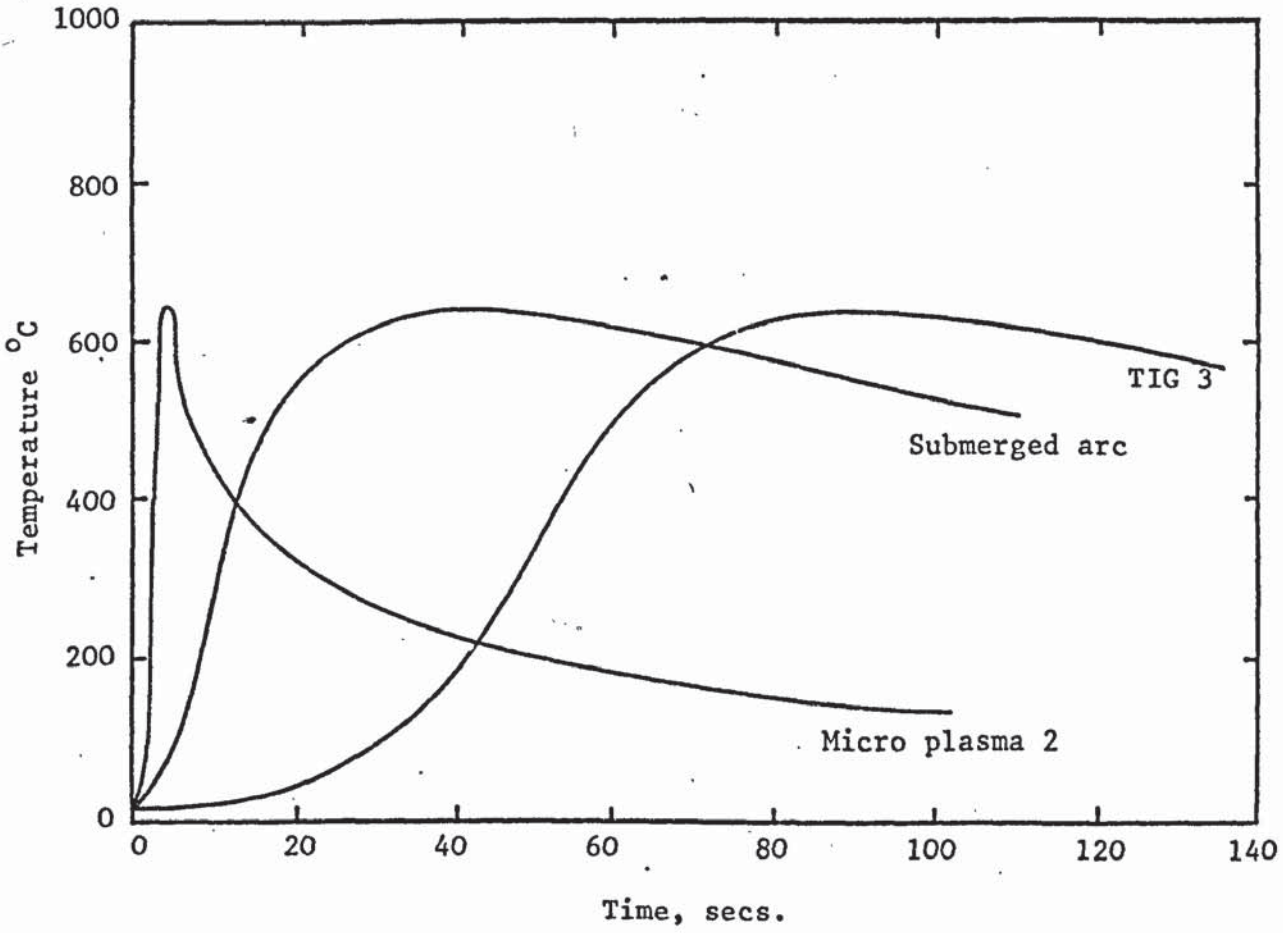

Fig. 3.12. Computed thermal cycles to a peak temperature of 650°C for a range of welding parameters.

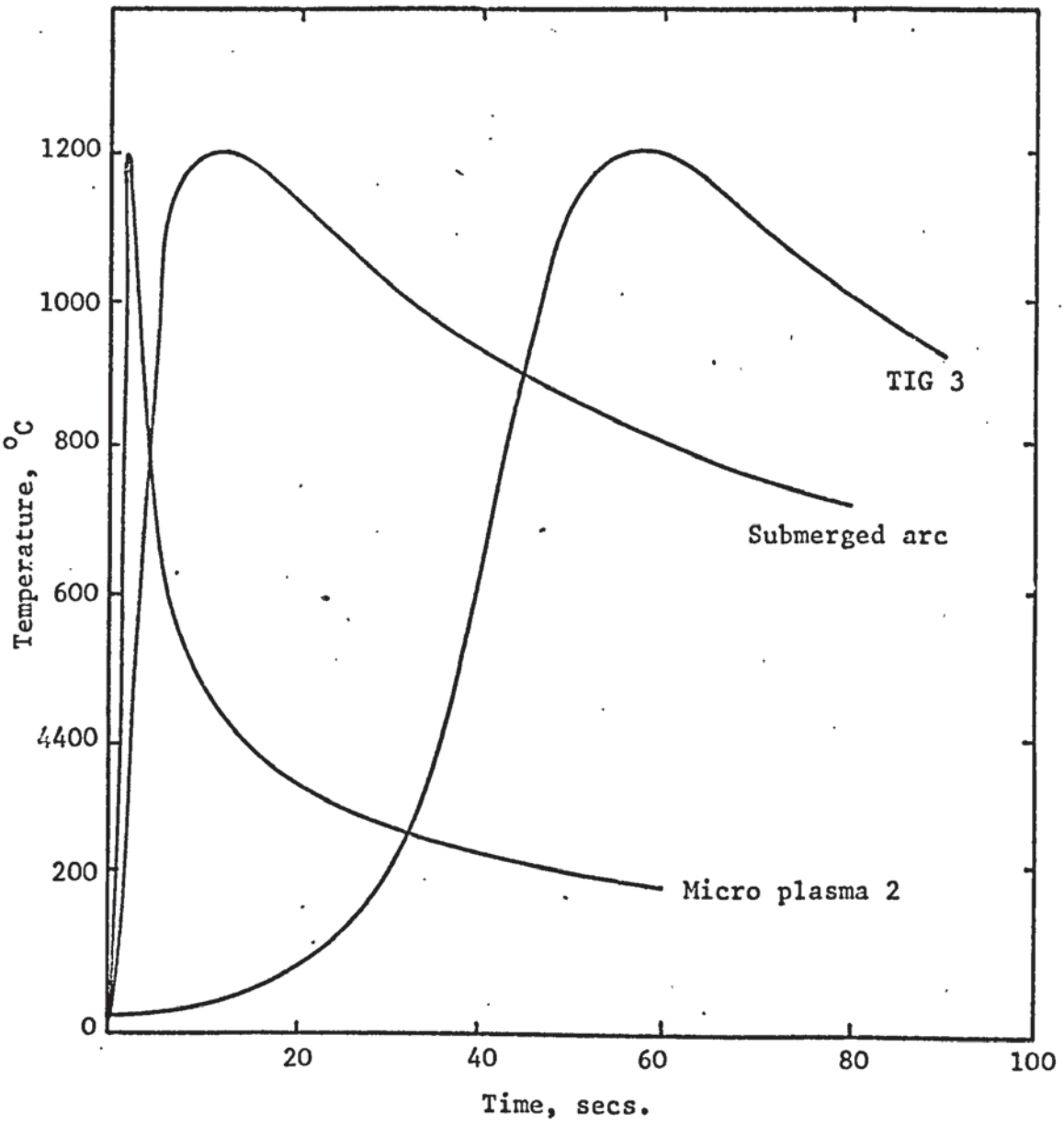

Fig. 3.13. Computed thermal cycles to a peak temperature of 1200°C for a range of welding parameters.

3.4 Thermal Cycle Simulation

Thermal cycle simulation was carried out using the Gleeble thermomechanical simulator manufactured by Duffers Associates. A general view of the equipment is shown in Fig. 3.14 with the reference generator and control-recording equipment in four console units and the specimen thermo-mechanical testing equipment on the right. The specimen is gripped between massive water cooled copper chucks and submitted to a prescribed thermal cycle by the combined effects of resistance heating and conduction cooling at rates controlled by a thermocouple percussion welded to the centre of the specimen. One copper chuck is fixed whilst the other remains free to slide. Strain can be applied if required using pneumatic hydraulic equipment via a load cell attachable to the sliding copper chuck. Testing can be carried out in a controlled atmosphere chamber completely enclosing the specimen, but this was not used during this investigation. Details of the testing equipment including the specimen, control thermocouple, copper chucks and load cell are shown in Fig. 3.15.

Before any computed H.A.Z. thermal cycles were simulated it was essential to investigate rigorously the thermal conditions in the specimens during cycling.

3.4.1 Temperature calibration

The temperature of a specimen heated in the Gleeble is measured and controlled by a thermocouple percussion welded on to the surface of the specimen. Due to radiation and convection the surface temperature may not be the same as the internal temperature. Also, the thermocouple bead

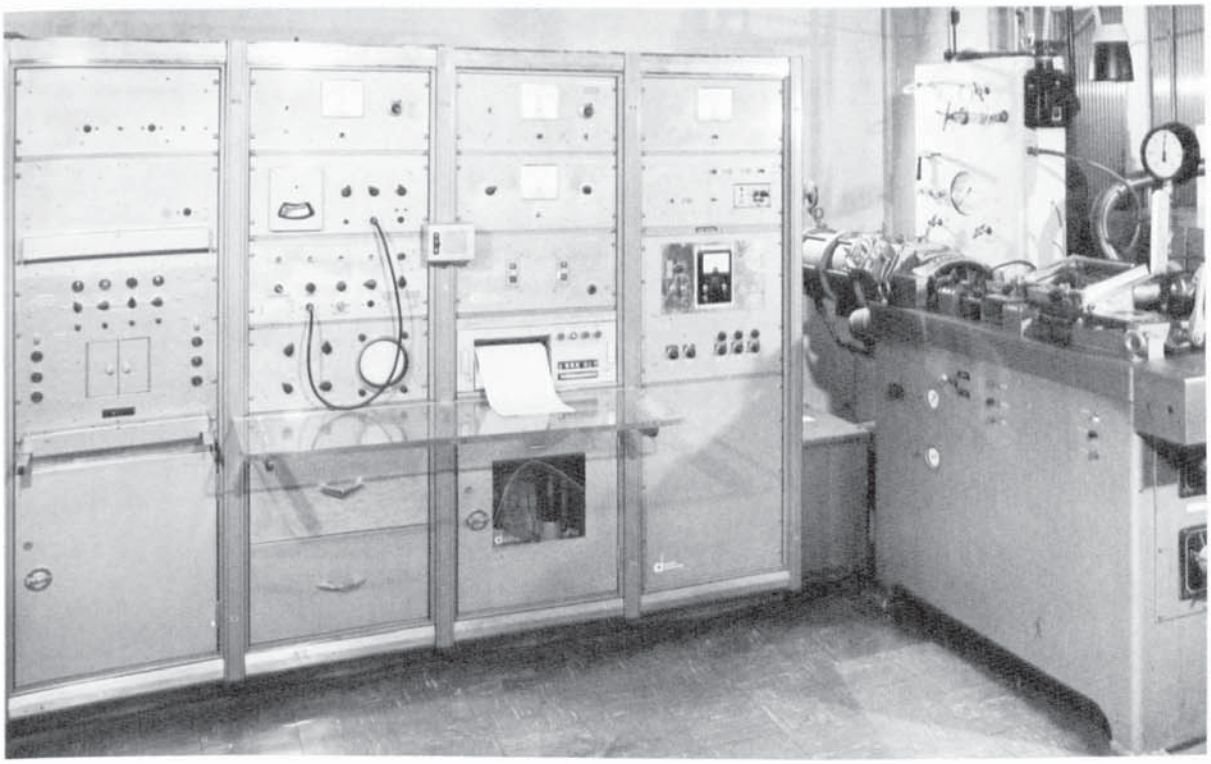

Fig. 3.14. General view of the Gleeble thermo-mechanical simulator.

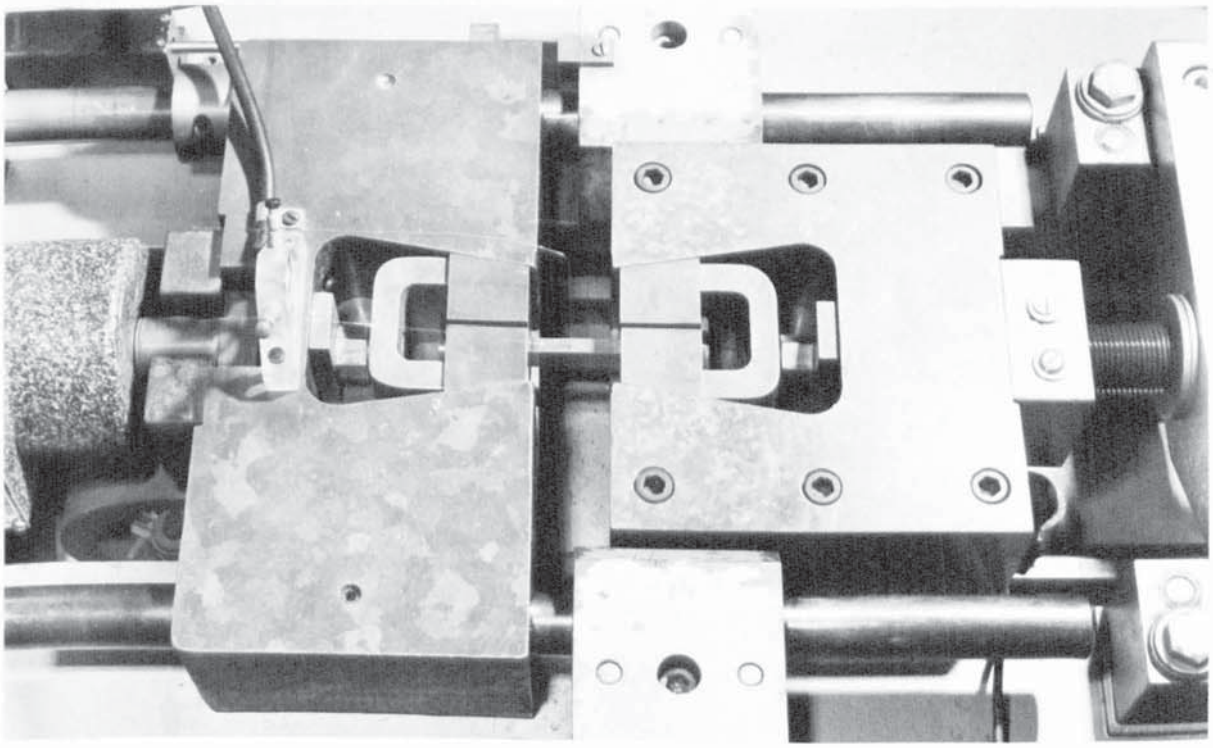

Fig. 3.15. The Gleeble thermo-mechanical testing head with specimen and control thermocouple in position.

has a chilling effect on the specimen in its immediate vicinity due to conduction. Consequently, a temperature difference exists between the temperature indicated by the control thermocouple and the temperature of the bulk of the specimen. This difference will vary depending on a number of factors including the size of the thermocouple wires and bead, and the temperature of the specimen. Before continuing with any simulation work it was essential to establish the magnitude of this temperature difference.

Chromel/Alumel thermocouples were used throughout this investigation. The thermocouple wires were 0.010" diameter, and were joined prior to attaching adjacent to the top mid-surface position of the specimens. The specimens used in all the simulation work were three point bend specimen blanks. These were unnotched and $3\frac{1}{2}$" long to allow sufficient material to be held in the copper chucks. The specimens were gripped with the $\frac{1}{2}$" cross section dimension parallel to the vertical in all cases.

The temperature of the bulk of the specimen was measured using a sheathed 0.020" diameter chromel/alumel thermocouple. This was inserted in a close fitting blind hole drilled to the centre of the specimen from the top mid-surface position. During the course of this work insulated and non-insulated types of junction were used. It was found that over the range studied both produced the same level and rate of response for the same programmed thermal cycle.

An arbitrary thermal cycle was programmed on the Gleeble's reference generator for the purposes of temperature calibration. The peak temperature was preset using the

Gleeble's control millivoltage potentiometer and whilst the full thermal cycle was generated in the specimen the control and sheathed thermocouple temperatures were indicated and recorded on the Gleeble's U.V. recorder. The thermal cycle was then repeated but held at the peak temperature. During this time the control and sheathed thermocouple temperatures indicated on the U.V. recorder were closely compared. The object was to detect any increase in the sheathed thermocouple temperature that was not due to an increase in the control temperature and might consequently be a result of localised heating at the tip of the drilled hole. No such effect was found and it was concluded that the locally increased current density had negligible effect.

The signal from the sheathed thermocouple was then switched to an independent potentiometer circuit and measured whilst remaining steady. The control thermocouple millivoltage was then checked against the preset value and hence corresponding control and bulk specimen temperatures were deduced. This was repeated using different thermocouples at the same temperature and at different peak temperatures. The control thermocouple temperature versus specimen temperature calibration graph was established by regression analysis of the results and is given in Fig. 3.16.

3.4.2. Temperature distribution

The object of H.A.Z. thermal simulation is to reproduce H.A.Z. structures and properties in a specimen sufficiently large enough to test using conventional techniques. To determine how much of the specimen has been subjected to the required thermal cycle it is necessary to know the temperature

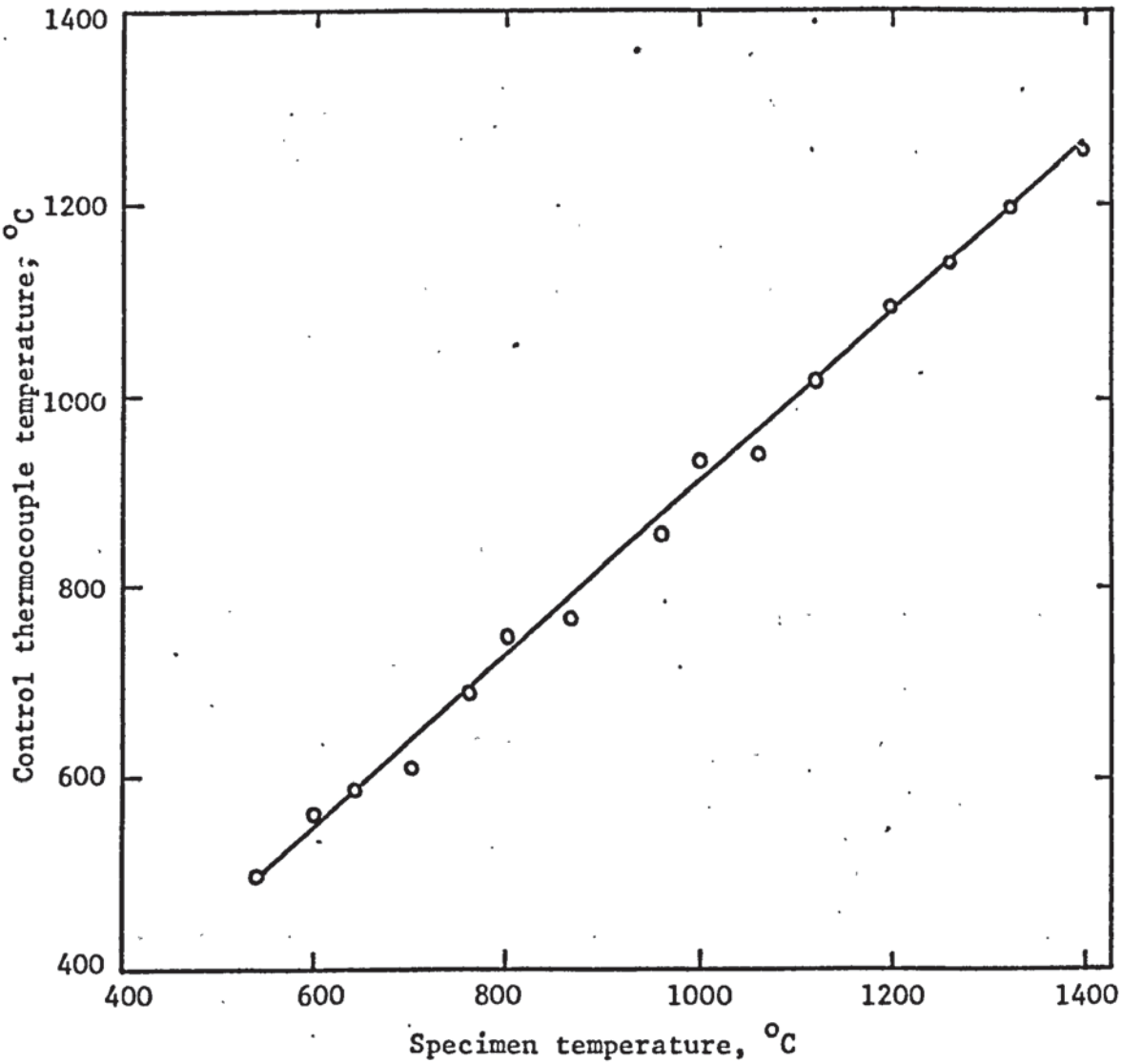

Fig. 3.16. Specimen temperature versus control thermocouple temperature.

distribution in the specimen. For a particular cross sectional area this will depend on the peak temperature to be considered and the gauge length of the specimen, that is the length gripped between the copper chucks. Peak temperatures of 650°C and 1200°C with gauge lengths the minimum possible ½" and maximum required 1" were selected as representative of the ranges to be used. The temperature distributions corresponding to these conditions were then examined. For a fixed cross section of ½" by ¼".

The longitudinal temperature distribution was measured using a second chromel/alumel thermocouple percussion welded at different positions along the top surface longitudinal centre line of the specimen. The temperature calibration established in the previous section was used to convert the surface temperature measurements into bulk specimen temperatures. The results obtained are shown in Fig. 3.17 and indicate the considerable effect of gauge length on the temperature plateau.

The transverse temperature gradients were measured using a series of specimens containing 0.020" diameter clearance holes drilled to different depths through the width of the specimen from the top mid-surface position. A chromel/alumel sheathed thermocouple was used to measure the temperature at the bottom of the holes for bulk specimen temperatures of 650°C and 1200°C. A gauge length of ½" was used since this was expected to produce the severest, if any, gradients. The results obtained are shown in Fig. 3.18 and indicate that a uniform temperature distribution exists through the thickness. The impression of a

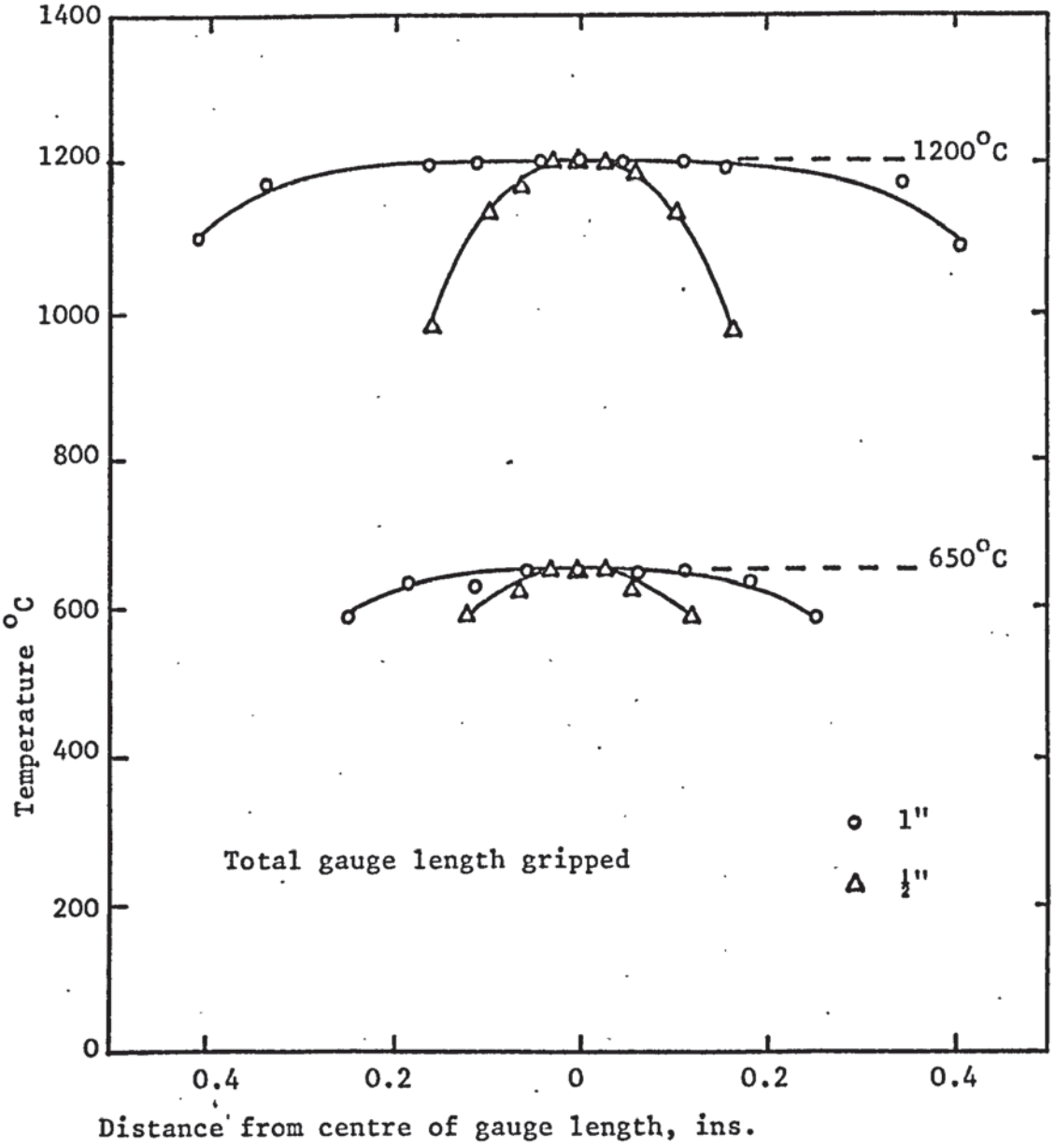

Fig. 3.17. Longitudinal peak temperature distribution for thermal cycles to peak temperatures of 650°C and 1200°C.

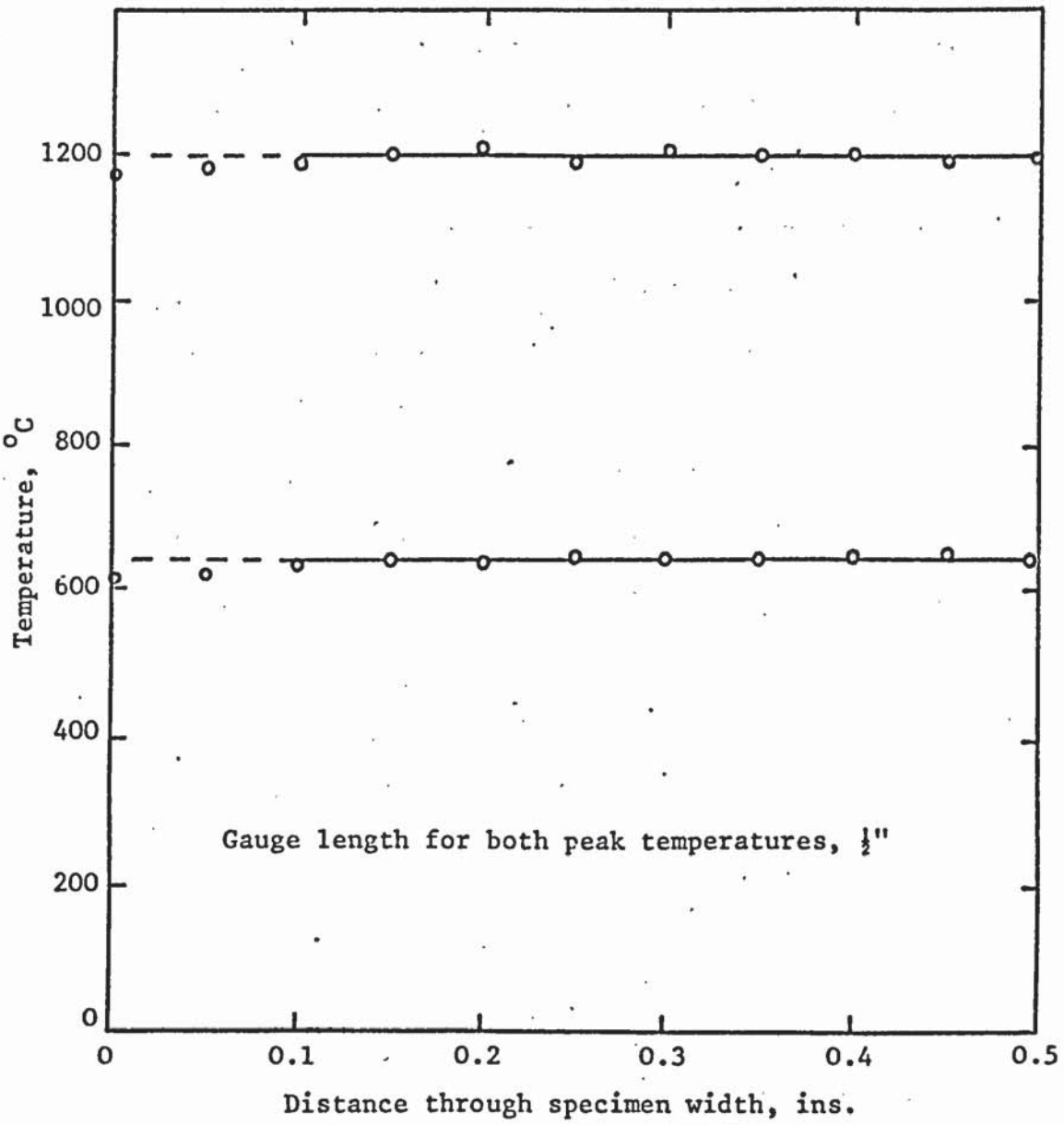

Fig. 3.18. Transverse peak temperature distribution for thermal cycles to peak temperatures of 650°C and 1200°C.

temperature gradient between the specimen surface and 0.1" through the specimen was considered to arise because insufficient of the sheathed thermocouple was immersed in the specimen for an accurate reading. Consequently the thermocouple was approaching a surface welded position, resulting in a chilling effect.

In both the longitudinal and transverse temperature measurements, full thermal cycles as well as peak temperatures were measured. These indicated that positions experiencing the same peak temperature also experienced the same thermal cycle. From these results it was deduced that even with the shortest gauge lengths and highest peak temperatures, sufficient material could be thermally cycled to permit accurate assessment of structure and properties.

3.4.3 Heating and cooling rates

The thermal cycles produced by the welding processes and parameters under investigation cover a wide range of heating and cooling rates. To ensure these conditions could be simulated it was necessary to carry out a number of heating and cooling rate trials. From published data[89] it was apparent that the required heating rates could be obtained, but the position with respect to cooling rates was not as clearly defined because they are dependent upon the thermal constants and geometry of the specimen used.

Cooling in the Gleeble is achieved by conduction of heat away from the specimen by massive water cooled copper chucks. Controlled cooling rates are obtained by balancing resistance heating and conduction cooling to give the cooling cycle programmed on the reference generator. Slow

cooling rates are easily obtained but fast rates present a problem. If the programmed cooling rate is greater than can be achieved by conduction, uncontrolled cooling proceeds at the maximum natural rate for that situation. For accurate thermal cycle simulation it is therefore necessary to ensure that the factors affecting cooling rate are adjusted to give a natural cooling rate greater than the required cooling rate.

The factors affecting the Gleeble cooling rates of a particular material are

(1) specimen cross sectional geometry

(2) specimen gauge length

(3) thermal cycle peak temperature.

A series of experiments were conducted to determine the combined effects of these variables. Peak temperatures of 650°C and 1200°C were again selected as representative of the regions of interest. Specimens $\frac{1}{2}$" wide by 0.250" and 0.150" thick were used with gripped gauge lengths between 0.5" and 1". The specimens were heated to peak temperature and then allowed to cool naturally. The cooling rates were measured over the first eight seconds after the peak temperature from the control thermocouple U.V. chart record.

The results obtained are presented graphically in Fig. 3.19. This indicates that reducing the specimen thickness increases the cooling rate by about 5°C per sec for a peak temperature of 650°C and 10°C per sec for a peak temperature of 1200°C. However, a greater increase in cooling rate can be achieved in both cases by reducing the gripped gauge length. As mentioned in section 3.3.2, a

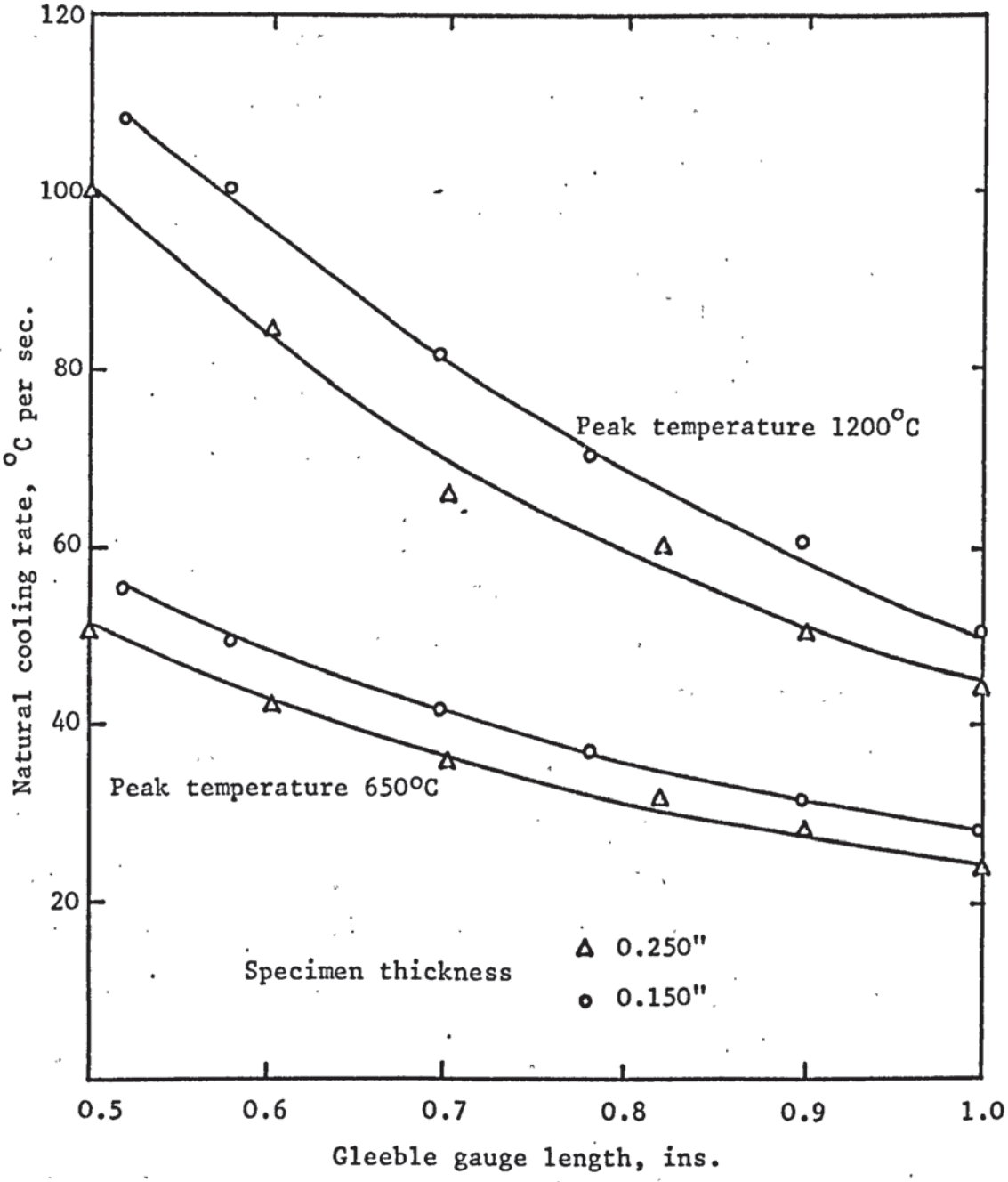

Fig. 3.19. The effect of Gleeble gauge length on natural cooling rate, measured over the first eight seconds of the cooling cycle, for different peak temperatures and specimen thickness.

number of welding parameters originally selected for simulation were deleted on the basis of these cooling rate results. The remainder can be simulated under controlled conditions, with the required cooling rates obtainable even using 0.250" thick specimens. For any particular cooling rate, longer gauge lengths can be used with 0.150" thick specimens than with 0.250" thick specimens. This would result in more material following the required thermal cycle and could prove a useful factor particularly at shorter gauge lengths. This section completed the necessary preliminary work and subsequently the H.A.Z. thermal cycle simulation was commenced.

3.4.4 Computed H.A.Z. thermal cycle simulation

The thermal cycles to be simulated were programmed in turn on the reference generator. The temperature ordinate of the reference generator programme board was designed to operate on a percentage basis, with the thermal cycle peak temperature representing 100%. This position was adjusted, through the Gleeble control potentiometer, to correspond with the required peak temperature millivoltage using the calibration graph Fig. 3.16. All other temperatures were pegged according to the percentage they represented of the peak temperature millivoltage. Consequently, it was necessary to convert the computed temperature - time cycles into firstly millivoltage-time then percentage-time cycles.

The instantaneous reference generator millivoltage that controls the required specimen temperature at any time is taken from the programme board by a rotating drum. The speed at which this drum rotates governs the rate at which

the time base of the programme board is covered and consequently controls the heating and cooling rates in the specimen. A number of drive speeds were available and could be altered during thermal cycling by preset control switches. These were adjusted as required for each thermal cycle to be simulated. A general view of the reference generator programme board, rotating drum and drive speed controls is given in Fig. 3.20 and shows a typical thermal cycle programmed for simulation.

Initially, thermal cycles to peak temperatures of 650°C and 1200°C were simulated. The specimen gauge lengths were adjusted according to the data presented in Fig. 3.19 to give the required controlled cooling rates. The thermal cycle experienced by each specimen was monitored on the U.V. recorder and compared with the programme cycle to ensure the required conditions had been simulated. Six specimens were thermally cycled for each set of welding parameters, three for fracture toughness testing and metallography, and three for tensile property measurements. Unlike the parent material tests, tensile test pieces could not be machined from the broken fracture toughness specimens because the positions of interest are contained only in the central regions of the thermally cycled blanks. On the basis of these results thermal cycles to a number of other peak temperatures were studied. The information required to determine the gauge lengths for controlled cooling from these peak temperatures was obtained by interpolation or extrapolation of the 650°C and 1200°C peak temperature data. The estimated gauge for each new thermal

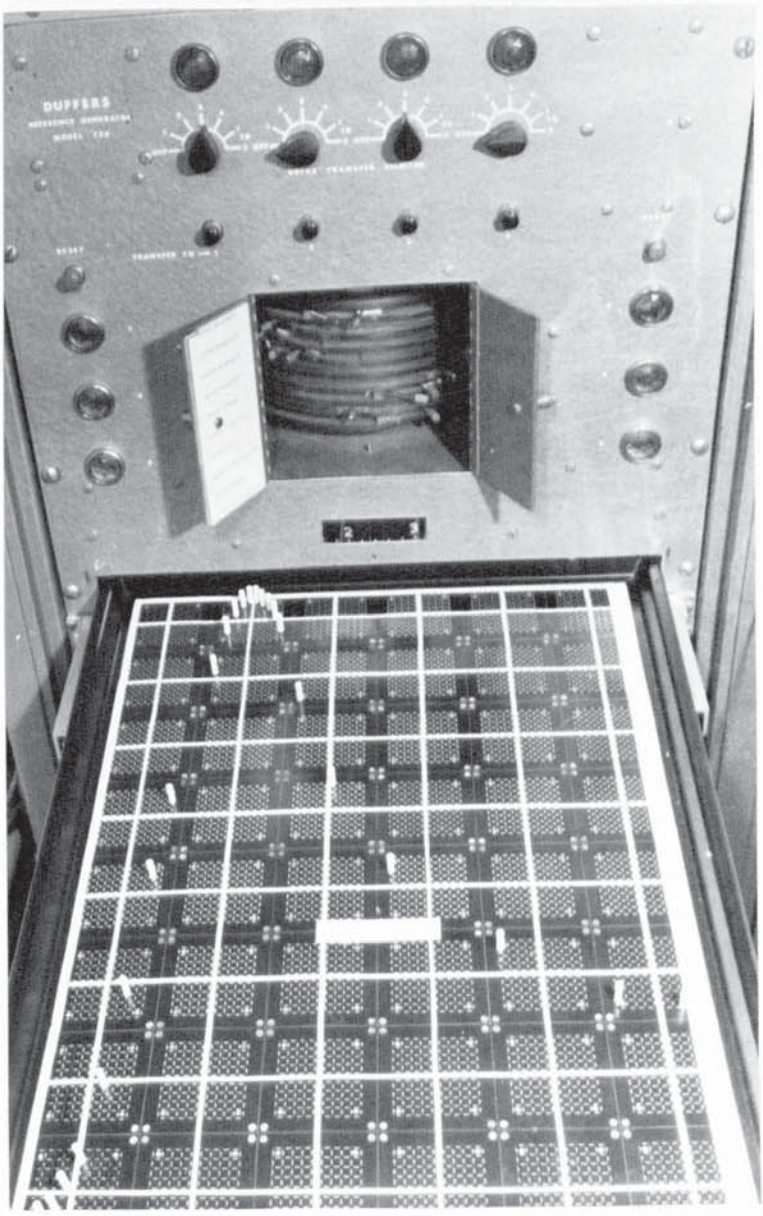

Fig. 3.20. The Gleeble thermal cycle reference generator.

cycle was tested using a trial specimen to ensure that controlled cooling was achieved. Six specimens for each condition were then thermally cycled and subsequently tested.

The programmed thermal cycles were accurately reproduced in the specimens by the Gleeble controls throughout this investigation. From the U.V. records, the peak temperatures were generally within $\pm$ 5°C of the required values, and at all stages of the heating and cooling cycles a similar degree of accuracy was obtained. With some faster heating rates to high peak temperatures, the accuracy and reproducibility were more variable. However, even in these cases, where the peak temperatures tended to overshoot the required level, careful adjustment enabled the peak temperatures and reproducibility to be maintained within the satisfactory limits of $\pm$ 10°C.

3.5 Simulated H.A.Z. Fracture Toughness and Tensile Properties

3.5.1 Testing procedure

The thermally cycled specimens were in the form of $\frac{1}{2}$" by $\frac{1}{4}$" by $3\frac{1}{2}$" blanks, with the simulated H.A.Z. contained in the central portion of the blank. The specimens for fracture toughness testing were machined such that the notch position coincided with and removed the thermal cycle control thermocouple bead. The specimens were then aged at 485°C for three hours and surface ground to the final dimensions. Fatigue cracking and fracture toughness testing were carried out as described in section 3.2.2.

During fracture toughness testing the crack propagation was arrested in one specimen from each batch of three. These were used for metallographic examination, and an estimate of the crack length a in these specimens, required to determine the fracture toughness, was based on the surface crack lengths. The remaining specimens in each batch were fractured completely and the fracture surfaces preserved for examination using the scanning electron microscope.

The thermally cycled specimens selected for tensile testing were aged in the blank form prior to machining. The hardness of the simulated H.A.Z. was measured before and after ageing using a Vickers hardness testing machine, and the results recorded for later correlation. Standard number eleven Hounsfield test pieces were then machined from the aged specimens such that the centre lines of the thermally cycled regions coincided with the centre of the

tensile test piece gauge length. The specimens were tested on the Instron and examined to ensure fracture had occurred at the centre of the gauge length. Measurements of reduction in area and elongation were made from the fractured test pieces.

3.5.2 Fracture toughness results

The results obtained from simulated H.A.Z. structures corresponding to peak temperatures of 650°C and 1200°C are presented graphically in Figs 3.21 and 3.22 respectively. The heating rates have been plotted as indicative of the range of welding parameters covered, corresponding to those listed in Table 3.7, and each point represents the average of three measurements. Full details of the tensile properties will be given later, but the mean values of yield strength were 115 tons per sq. in. and 123 tons per sq. in. for the peak temperatures of 650°C and 1200°C respectively. Using these values, the fracture toughness results were confirmed to be valid K_{Ic} measurements according to the recommended practice equation 3.3. However, if equation 3.4 which includes the validity factor 4 is used, the fracture toughness results for the 650°C peak temperature are not valid as K_{Ic}. In view of this and because fracture toughness has increased as a result of thermal cycling, it was decided to carry out further limiting thickness tests. Since fracture toughness appears to be independent of the welding parameters, the microplasma 1 conditions were selected for this work as representative of the range covered.

The results of the limiting thickness tests for thermal cycles to 650°C and 1200°C are given in Table 3.8. These

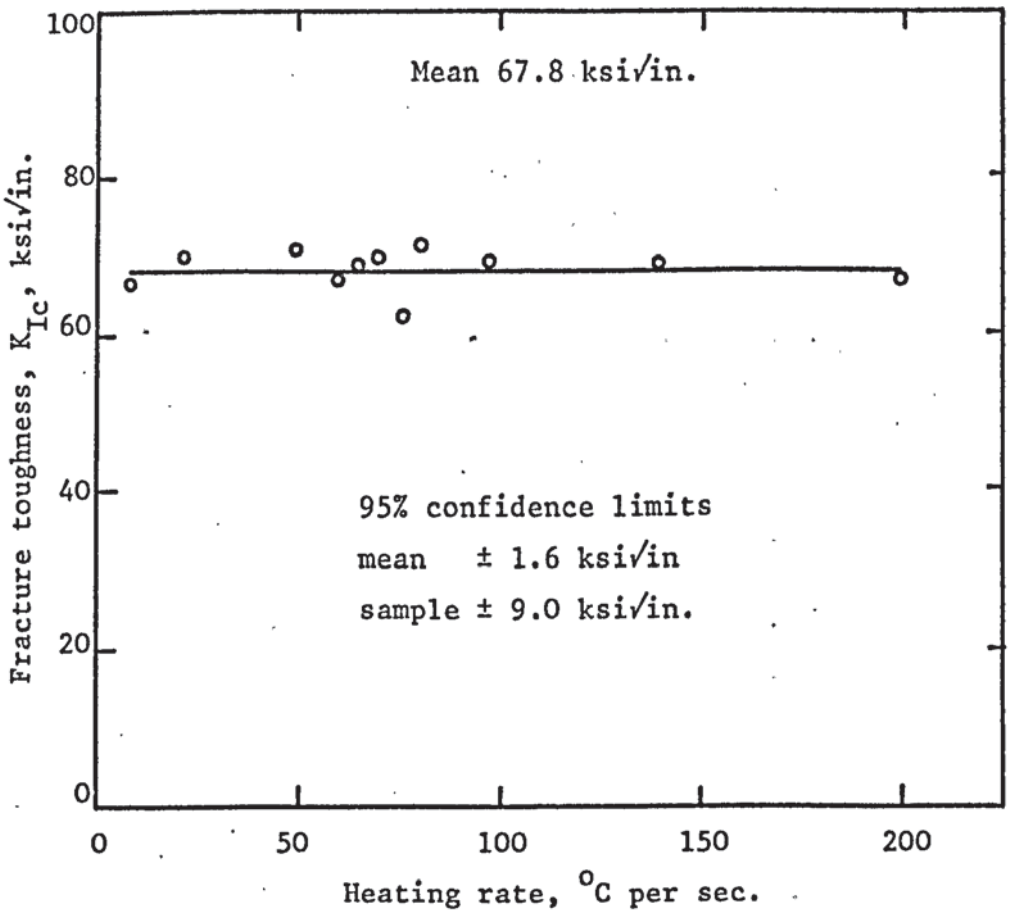

Fig. 3.21. The relationship between heating rate and fracture toughness for simulated H.A.Z. thermal cycles to a peak temperature of 650°C.

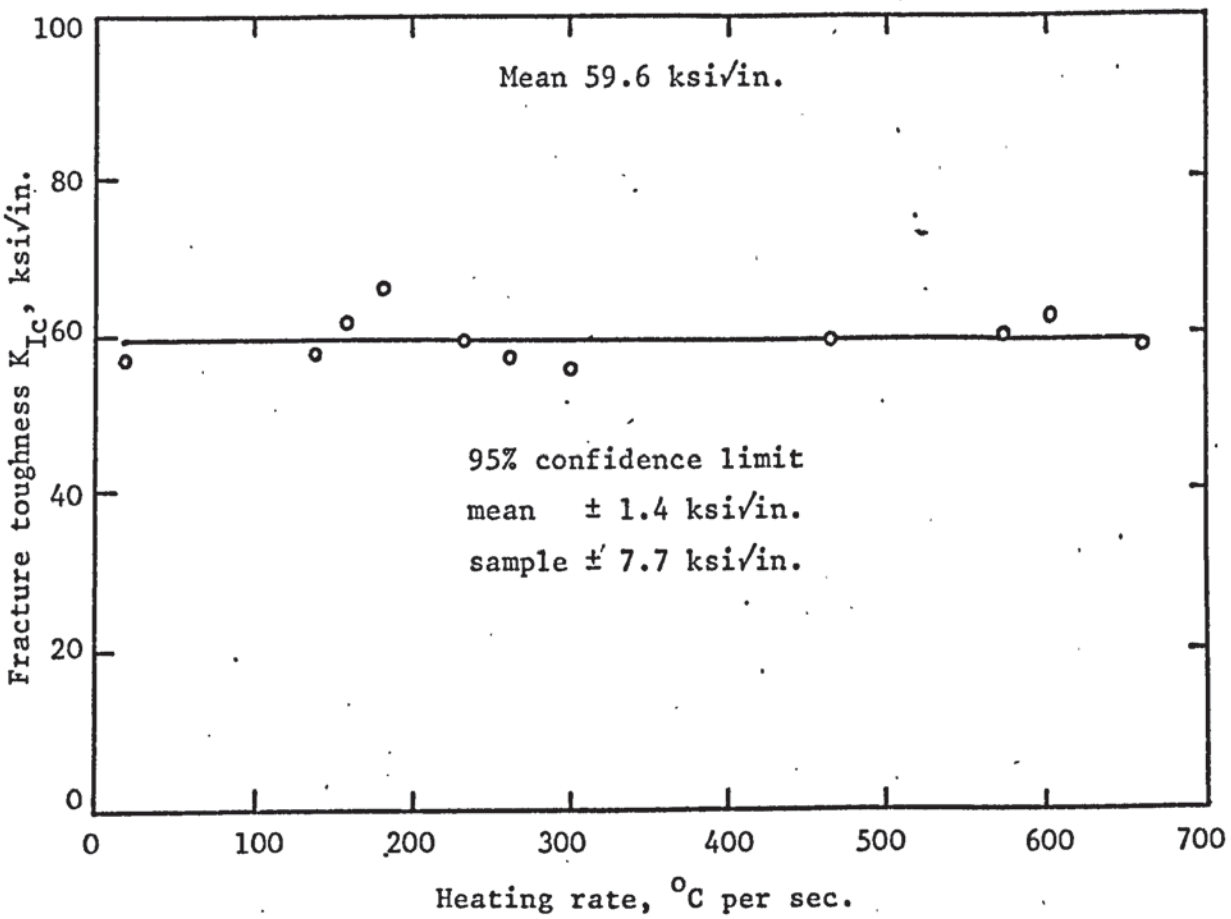

Fig. 3.22. The relationship between heating rate and fracture toughness for simulated H.A.Z. thermal cycles to a peak temperature of 1200°C.

Specimen Thickness ins	Fracture Toughness ksi√in	
	650°C	1200°C
0.250"	69.1	66.5
	74.2	66.9
	72.4	64.1
	66.4	68.8
	Mean 70.5	66.5
0.200"	71.5	68.6
	70.5	67.8
	70.8	65.4
	68.4	68.0
	Mean 70.3	67.4
0.150"	77.8	68.6
	71.4	71.6
	72.3	72.7
	81.2	70.2
	Mean 75.6	70.8

Table 3.8. The fracture toughness, K_Q, of specimens of different thickness thermally cycled to peak temperatures of 650°C and 1200°C.

indicate that for both peak temperatures a valid K_{Ic} result can be obtained from specimens 0.200" thick, but 0.150" appears to be below the limiting thickness. The minimum thickness requirements according to equations 3.3 and 3.4 were calculated from the mean value of the fracture toughness results for each thickness and are presented in Table 3.9. These indicate that the limiting thickness determined by inspection of the results in Table 3.8 is confirmed by the recommended practice equation 3.3, but if equation 3.4 is used only the results obtained from the 0.250" thick specimens thermally cycled to 1200°C are valid. The agreement between the limiting thickness measurements and the recommended practice contradicts the parent material findings and represents further evidence of the variation of thickness effects with strength and toughness. However, since the recommended practice has been shown to hold for the thermally cycled condition this will be applied to all future results, and the specimen thickness will be maintained at 0.250" unless otherwise stated.

Correlation and regression analysis was carried out on the results presented in Figs 3.21 and 3.22 and although the correlation coefficients were not statistically significant, the factor that emerged was that fracture toughness was independent of the welding parameters involved, but varied with peak temperature. A statistical comparison of the two sets of results and as received data was carried out. Taking any pair of sets of results, the "F" test of variances indicated that there was no evidence of any difference in the variances and consequently the students

Specimen thickness ins	Thermal cycle peak temperature °C	Limiting thickness ins.	
		$2.5\left(\frac{K_Q}{\sigma_{ys}}\right)^2$	$4\left(\frac{K_Q}{\sigma_{ys}}\right)^2$
0.250	650	0.187	0.299
0.200		0.186	0.297
0.150		0.215	0.344
0.250	1200	0.146	0.234
0.200		0.150	0.240
0.150		0.165	0.264

Table 3.9. The limiting thickness required for valid K_{Ic} results from thermally cycled specimens, based on K_Q results given in Table 3.8 and different validity factors.

"t" test of means could be applied. Again, taking any pair of sets of results it was found that the probability of obtaining these results by chance was less than 1 in 1000, indicating that a very highly significant difference exists between any pair of the three sets of data.

Further H.A.Z. thermal cycle simulation was carried out to peak temperatures of 600°C, 800°C, 1000°C, 1325°C and 1400°C. The first three temperatures were selected to give a more complete coverage of the H.A.Z. The peak temperature of 1325°C was selected on the basis of published data[74,76] in an attempt to produce embrittlement as a result of either constitutional liquation or complete solution and precipitation of inclusions. The highest temperature, 1400°C was designed to exaggerate these effects if they occurred and to cover the possibility that in previous published work the temperatures recorded were lower than the true specimen temperature. Since the heating and cooling rates appeared to have no significant effect in the previous thermal cycles the extended series of tests were carried out by simulating welding parameters giving slow, intermediate and fast rates only. Other parameters could be simulated as and when required. The welding parameters used and their corresponding heating and cooling rates for the peak temperatures concerned are given in Table 3.10.

Fracture toughness testing was carried out as before, and the fracture toughness results are given in Table 3.11. The fracture toughness of specimens thermally cycled to peak temperatures of 600°C, 800°C and 1000°C appear no

Welding parameters	Peak temperature °C	Heating rate °C per sec	Cooling rate °C per sec
Sub arc	600	18	1
TIG 2		50	5
MIG 1		94	8
Sub arc	800	42	3
TIG 2		100	13
MIG 1		220	20
Sub arc	1000	81	5
TIG 2		172	25
MIG 1		415	36
Sub arc	1325	180	17
TIG 2		316	53
MIG 1		830	69
Sub arc	1400	220	21
TIG 2		350	60
MIG 1		875	79

Table 3.10. The heating and cooling rates associated with different welding parameters and thermal cycle peak temperatures.

Thermal cycle peak °C	Fracture toughness ksi√in			
	Sub arc	TIG 2	MIG 1	Mean
600	57.4	56.9	50.9	56.7
	56.8	60.2	59.0	
	57.1	55.5	56.4	
800	58.0	54.5	52.5	56.7
	59.0	58.1	57.5	
	56.6	56.1	56.4	
1000	52.9	52.5	54.1	52.8
	53.4	52.5	52.9	
	52.6	52.2	52.2	
1325	60.8	61.0	60.3	61.1
	61.9	61.6	61.1	
	62.8	59.4	61.2	
1400	66.5	69.8	72.2	70.1
	71.2	69.1	70.0	
	73.5	69.3	69.2	

Table 3.11. The fracture toughness of simulated H.A.Z. structures for different welding parameters and thermal cycle peak temperatures.

different from the as received material and this was confirmed statistically. However, for peak temperatures of 1325°C and 1400°C the toughness increased progressively and in both cases is statistically very highly significantly different from the as received material. No evidence of a reduction in fracture toughness was found associated with any of the H.A.Z. thermal cycle peak temperatures simulated.

3.5.3 Tensile properties

The tensile properties obtained from simulated H.A.Z. structures corresponding to peak temperatures of 650°C and 1200°C are given in Table 3.12. Each result represents the average of three tests carried out on the thermally cycled specimens and correspond to the welding parameters listed. The values were used in conjunction with the respective fracture toughness measurements to ensure valid plane strain results had been obtained in accordance with the recommended practice.

The results given in Table 3.12 indicate that thermal cycling has affected the tensile properties, in particular the limit of proportionality and the ultimate tensile stress. These effects are more marked in the specimens thermally cycled to a peak temperature of 650°C. The elongation and reduction of area are affected in some cases, but to a lesser degree. As with the fracture toughness results, the tensile properties appear to be independent of the weld H.A.Z. thermal cycles, but dependent on the peak temperature reached.

The tensile properties relating to the remaining thermal cycle peak temperatures studied are given in Table 3.13, each result representing the average of three

Welding Parameters	Thermal cycle peak temperature, 650°C				Thermal cycle peak temperature, 1200°C			
	σ_{LP} tons/in^2	σ_{uts} ton/in^2	Elong. %	Redn. area %	σ_{LP} ton/in^2	σ_{uts} ton/in^2	Elong. %	Redn. area %
Micro plasma 1	113	117	10	48	121	126	12	51
Micro plasma 2	123	128	10	44	124	133	11	47
TIG 1	114	119	10	46	124	132	11	47
2	121	127	10	45	122	131	12	48
3	103	113	12	50	123	130	10	43
4	114	121	11	46	125	133	11	48
MIG 1	122	127	10	46	123	132	10	47
2	112	117	10	46	123	132	12	50
3	123	129	10	43	123	129	10	47
Sub. arc	117	128	10	43	120	129	11	48
Elect. beam	111	118	10	46	123	133	11	49
Means:	115	121	10	45	123	132	9	44

Table 3.12. Tensile properties of simulated H.A.Z.s for thermal cycle peak temperatures of 650°C and 1200°C.

Welding Parameters	Peak Temperature °C	Tensile Properties			
		σ_{LP} ton/in^2	σ_{uts} ton/in^2	Elong. %	Redn. area %
Sub. arc.	600	122	129	10	46
TIG 2		120	129	10	44
MIG 1		124	132	10	43
Sub. arc.	800	124	132	10	41
TIG 2		128	137	10	40
MIG 1		128	136	10	41
Sub. arc	1000	128	135	10	44
TIG 2		126	136	10	43
MIG 1		126	136	10	44
Sub. arc	1325	122	131	6	25
TIG 2		122	132	5	10
MIG 1		120	129	10	44
Sub. arc.	1400	114	124	9	29
TIG 2		119	125	9	30
MIG 1		122	128	10	46

Table 3.13. The tensile properties of simulated H.A.Z.s for different welding parameters and thermal cycle peak temperatures.

measurements. These also indicate a similar dependence on peak temperature. For the peak temperatures 600°C, 800°C and 1000°C, the full range of tensile properties compare with the as received, aged parent plate properties, Table 3.4, apart from slightly lower strength levels in the case of specimens thermally cycled to peak temperatures of 600°C. The two higher peak temperatures 1325°C and 1400°C, have lower tensile properties than the original material as well as reduced elongation and reduction of area values for some of the thermal cycles simulated.

The results of the hardness measurements, before and after ageing, are presented graphically in Fig. 3.23 plotted against the simulated thermal cycle peak temperature. Each point represents the average result of nine measurements, three measurements being made on each specimen selected as representative of slow, intermediate and fast heating rates. The results show that complete hardening after ageing was not achieved in all the specimens.

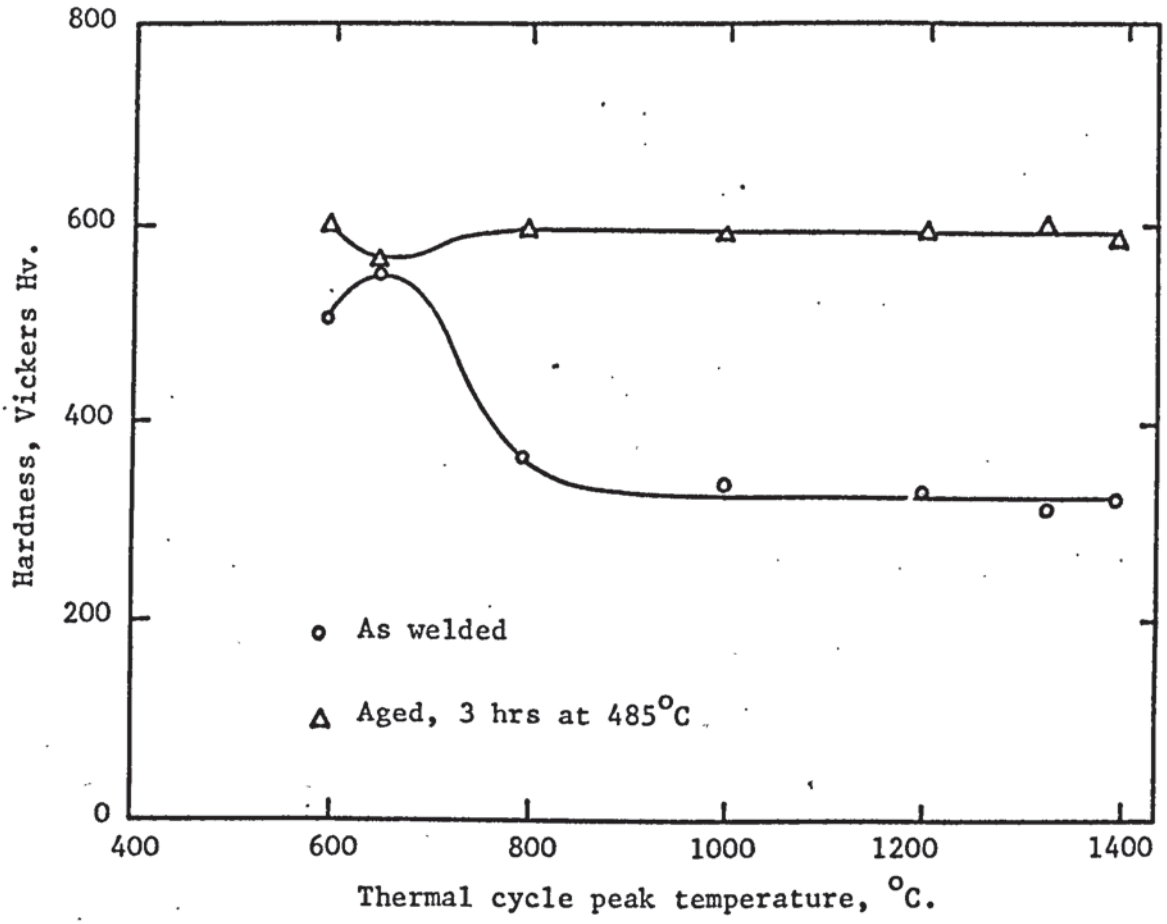

Fig. 3.23. The variation of hardness with thermal cycle peak temperature in the simulated H.A.Z.s.

3.6 Real Weld H.A.Z. Fracture Toughness and Tensile Properties

To establish the validity or otherwise of the thermal simulation approach to H.A.Z. studies a number of real weld H.A.Z.s were examined. The areas studied in the real weld H.A.Z.s were those relating to thermal cycle peak temperatures that produced property changes in the simulated H.A.Z.s. The processes and testing procedure adopted, and the results obtained will now be described.

3.6.1 Welding and testing procedure

The processes selected were required to satisfy a number of conditions in order that the results obtained could be related to the simulated H.A.Z. findings. Firstly, full penetration welds produced in a single pass were required to generate two dimensional heat flow conditions. Secondly, in order that plane strain fracture toughness tests could be carried out it was necessary to use the full $\frac{1}{4}$" thickness of the parent plate. Finally, wide H.A.Z.s were required in order that property measurements from any particular notch location could be related as closely as possible to a single peak temperature.

The submerged arc and M.I.G. welding processes were selected on the basis that they satisfied the above requirements. In order to establish the welding parameters a number of preliminary welds were made using $\frac{1}{4}$" thick mild steel plate. A BOC universal welding head positioned over a traversing table was used for both welding processes with the plates clamped on the traversing table against a copper backing bar. The weld bead widths produced in the mild steel trial welds were measured and used in conjunction with

the conclusions of Roberts and Wells[102] to determine the plate size necessary to ensure two dimensional heat flow conditions. The full plate dimensions used for both maraging steel welds were 20" by 12". The plates were welded in the solution annealed condition, with the weld centre line transverse to the final rolling direction.

During welding H.A.Z. thermal cycles were measured using sheathed chromel-alumel thermocouples inserted in blind-holes drilled to the plate mid-thickness. To measure temperatures close to the weld metal - H.A.Z. interface some holes were drilled into the plate at an angle. This was necessary to ensure that the exposed region of the thermocouple was not melted by the welding arc. The thermal cycles were measured using a u.v. recorder, and results for submerged arc welding of mild steel and submerged arc and M.I.G. welding of maraging steel were obtained. These were then compared with thermal cycles computed from the welding parameters in order to assess the accuracy of the theoretical approach.

The central regions of the welded plate were machined into specimen blanks for property measurements. The location of notches for fracture toughness specimens was based on examination of macro cross sections and knowledge of the peak temperature distribution obtained from the thermal cycle measurements. The macro sections were also used for transverse H.A.Z. microhardness measurements before and after ageing. The machining, heat treatment and testing procedures used were as previously described, with six specimens being tested for each notch location selected.

Also, in accordance with established procedure, metallographic and fractographic specimens were selected for examination from the fracture toughness specimens.

3.6.2 Submerged arc weld

The submerged arc weld was produced using a BOC MCRA 200 rectifier, $\frac{3}{32}$" diameter maraging steel wire type TML 131, and Metrode MARA 55 flux. The welding parameters used were 430 amps, 28 volts and 20 ins. per min. travel speed. The thermal cycles corresponding to the maximum and minimum peak temperatures measured in the mild steel H.A.Z. are shown in Fig. 3.24 together with the corresponding computed thermal cycles. Similar data for the maraging steel submerged arc weld H.A.Z. is given in Fig. 3.25. In this case the peak temperatures of 1075°C and 640°C were measured at the plate mid thickness, 0.12" and 0.37" from the weld metal H.A.Z. interface respectively.

The macro specimen prepared from a cross section of the submerged arc weld and H.A.Z. was examined and three H.A.Z. positions were selected for fracture toughness testing as indicated in Fig. 3.26. The first position relates to the region of reverted austenite and corresponds to the thermal cycle peak temperature 650°C. The second position utilises the full thickness of the parent plate and incorporates some of the structure appearing as coarse grained after macro etching. From the thermal cycle measurements it was estimated that this position covered a peak temperature range from about 1000°C to 1300°C. The third position was chosen such that the structures tested were almost entirely coarse grained. To accomplish this, and reduce the amount

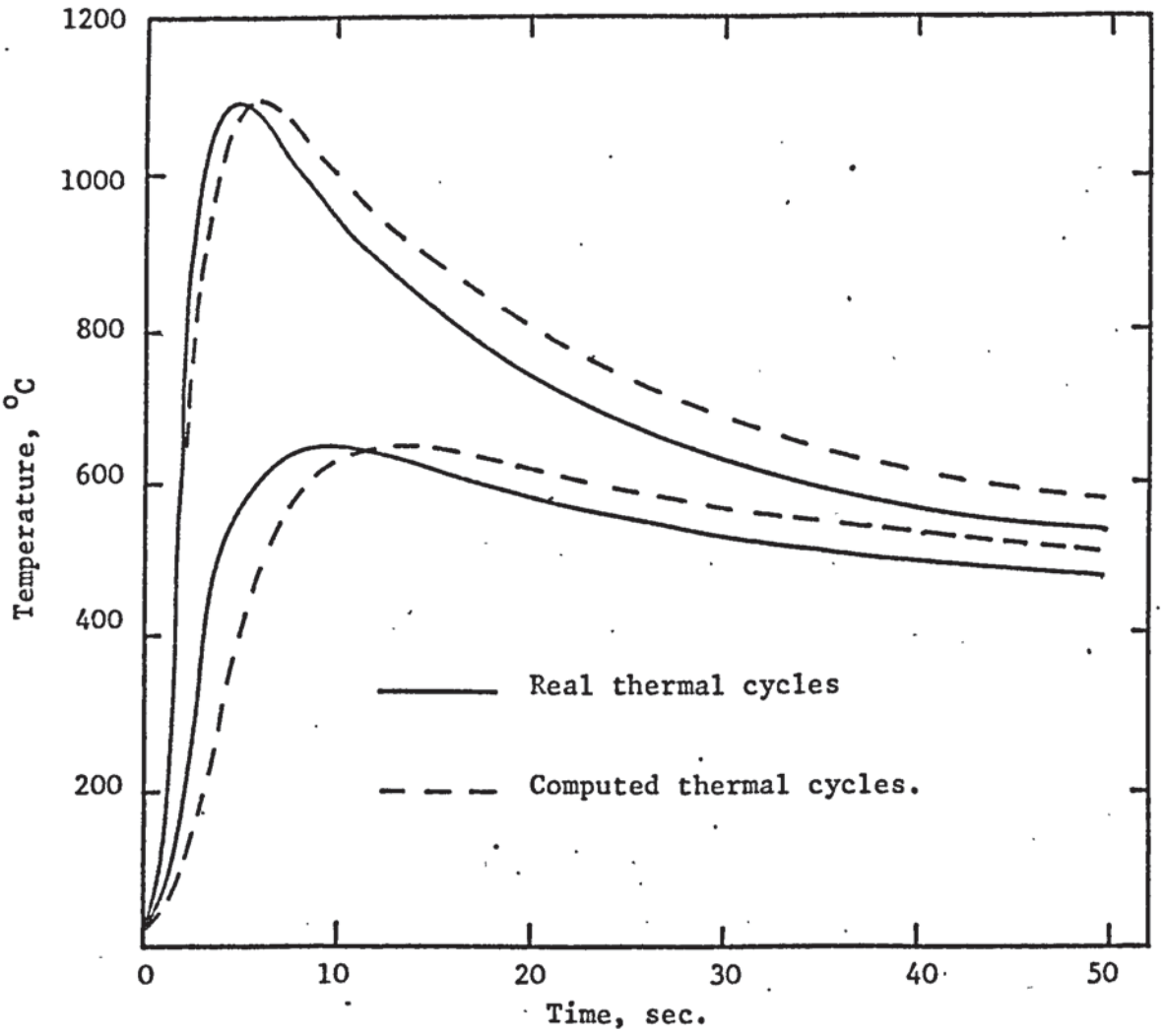

Fig. 3.24. Real and computed submerged arc weld H.A.Z. thermal cycles in mild steel plate.

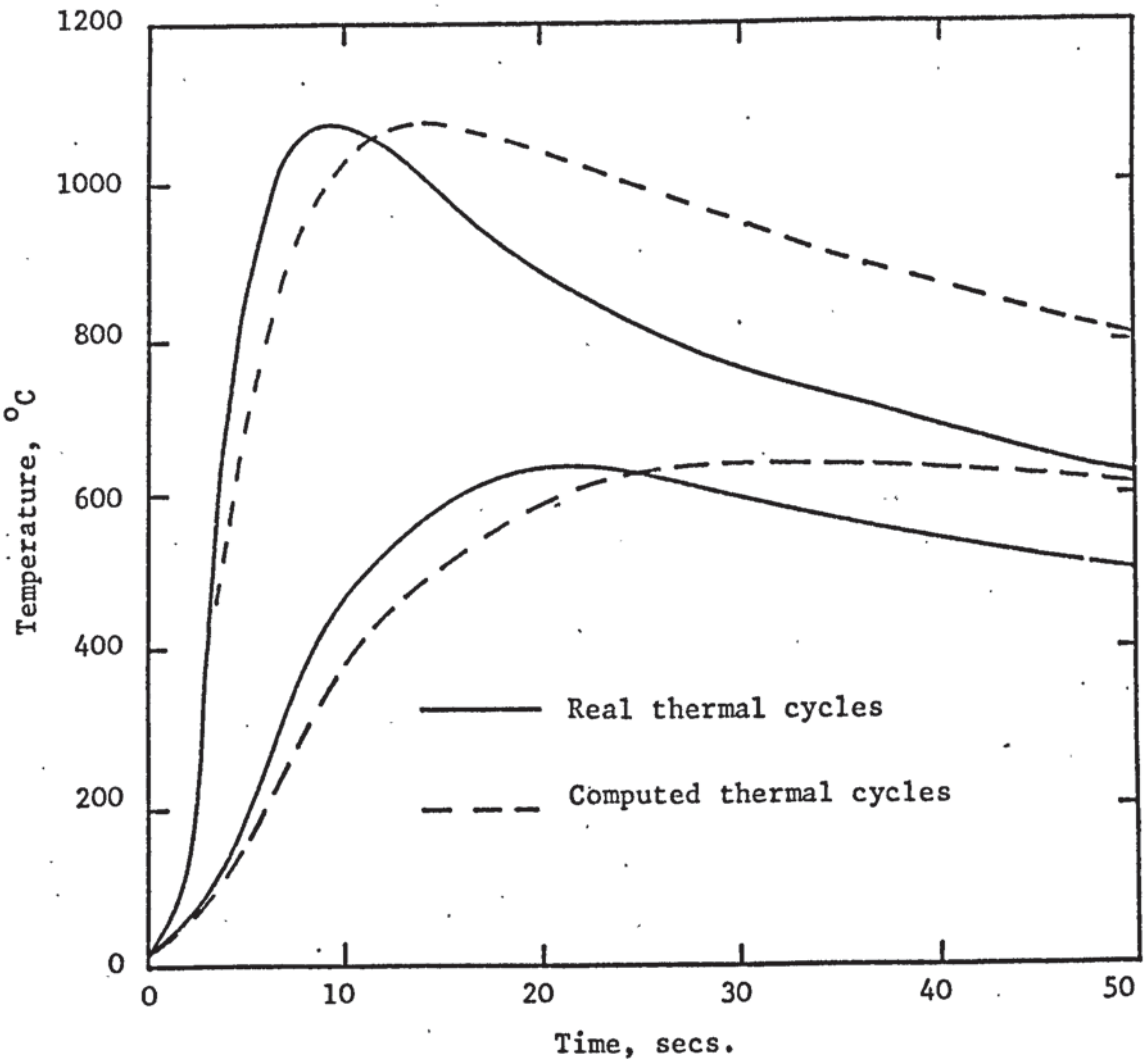

Fig. 3.25. Real and computed submerged arc weld H.A.Z. thermal cycles in maraging steel plate.

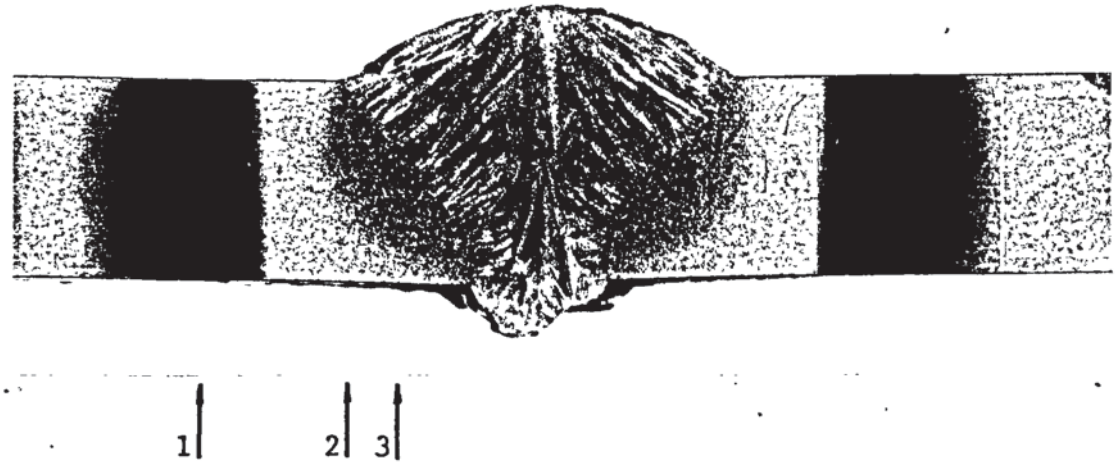

Fig. 3.26. Macro cross section of the submerged arc weld and H.A.Z. Etchant 25% nitric acid. x 4.

Fracture toughness at various H.A.Z. positions ksi√in		
650°C	1000-1300°C	1200-1460+°C
64.3	56.5	62.0
69.6	59.6	59.2
67.5	58.3	59.5
69.5	57.7	61.0
63.4	58.6	57.6
70.6	57.0	58.5
Means: 67.5	58.0	59.6

Table 3.14. The fracture toughness at various thermal cycles peak temperature positions in the submerged arc weld H.A.Z.

of weld metal contributing to the test results, it was necessary to use specimens 0.200" thick. From the thermal cycle measurements and the position of the weld metal interface it was estimated that this location covered a peak temperature range from 1200°C to 1460+°C. The fracture toughness results for these three positions are given in Table 3.14.

Tensile test pieces were machined from positions in the H.A.Z. corresponding to the fracture toughness specimens. However, useful results could only be obtained from positions 1 and 2. Test pieces taken from position 3 produced a considerable scatter of results, frequently failing outside the gauge length. This was probably a result of the unavoidable presence of some weld metal in the test pieces. The tensile properties for positions 1 and 2, relating to peak temperatures of 650°C and 1000°C to 1300°C are given in Table 3.15

3.6.3 M.I.G. weld

The M.I.G. weld was produced using a BOC SMR 400 rectifier, $\frac{3}{64}$" diameter maraging steel wire and Argon 1% Oxygen shielding gas. A 60° included angle weld preparation was used with a $\frac{1}{16}$" root face and the welding parameters were 370 amps, 33 volts and 24 ins. per min. traverse speed. The thermal cycles corresponding to the maximum and minimum peak temperatures measured are shown in Fig. 3.27 together with the corresponding computed thermal cycles. The peak temperatures of 1050°C and 540°C were measured at the plate mid thickness, 0.10" and 0.38" from the weld metal-H.A.Z. interface respectively.

H.A.Z. peak temperature 650°C				H.A.Z. peak temperature 1000-1300°C			
σ_{LP} tons/in^2	σ_{uts} tons/in^2	Elong. %	Redn. area %	σ_{LP} tons/in^2	σ_{uts} tons/in^2	Elong. %	Redn. area %
117	125	11	48	123	133	11	47
121	127	10	45	126	134	11	48
112	118	11	46	122	130	11	46
114	121	11	46	128	133	10	40
108	116	11	45	124	129	11	45
114	120	10	44	129	131	10	44
115	121	11	45	125	131	11	45

Means

Table. 3.15. Tensile properties for different thermal cycle peak temperature positions in the maraging steel submerged arc weld H.A.Z.

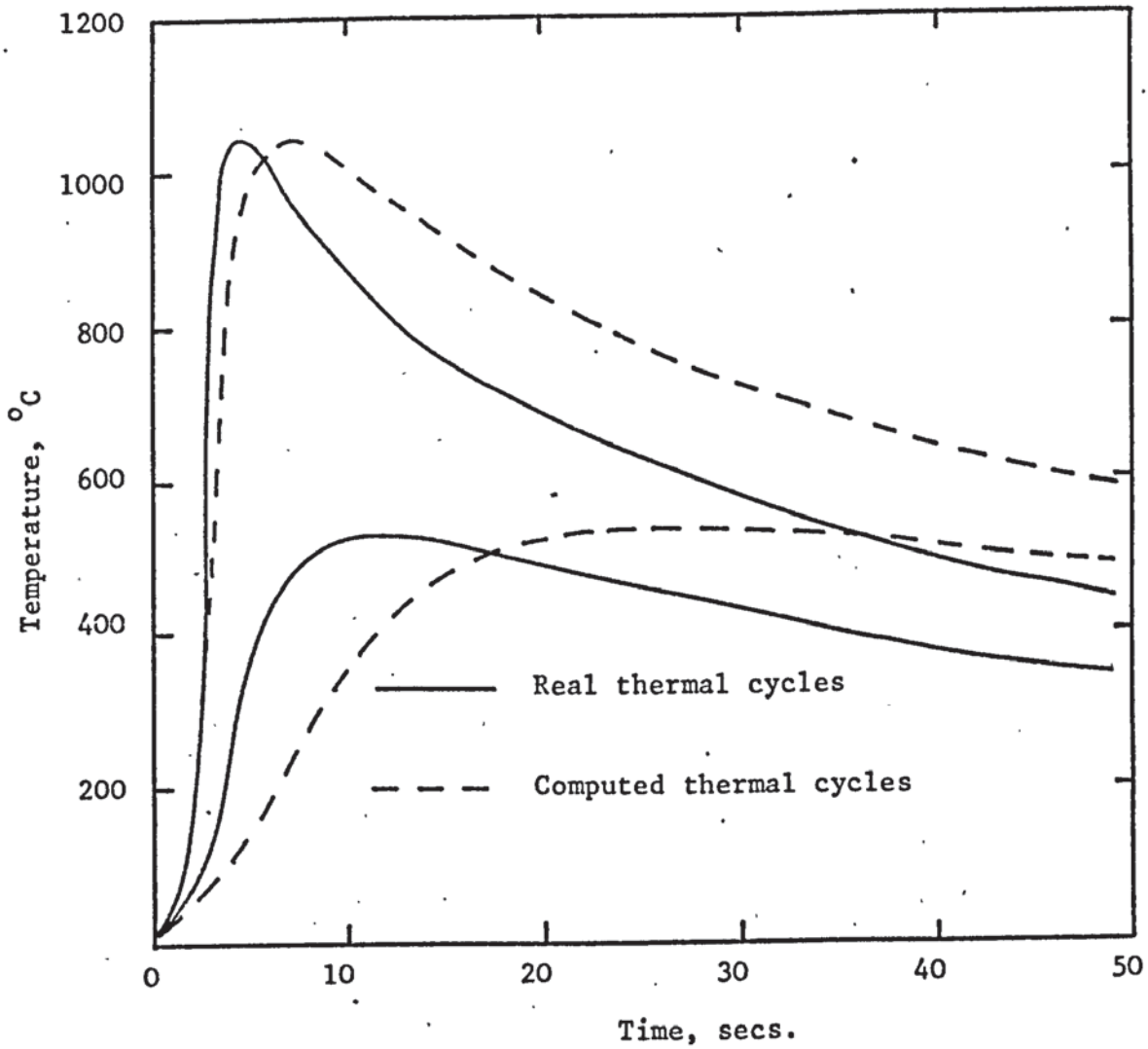

Fig. 3.27. Real and computed M.I.G. weld H.A.Z. thermal cycles in maraging steel plate.

A macro specimen was prepared from a cross section of the M.I.G. weld and H.A.Z., and fracture toughness tests were carried out on selected areas of the H.A.Z. as with the submerged arc weld H.A.Z. However, since the width of the M.I.G. weld H.A.Z. was less than that of the submerged arc weld H.A.Z., it was possible to test only one high temperature coarse grained region. In this case a specimen thickness of 0.200" was used to minimise the amount of weld metal contained in the specimen. The macro cross section is shown in Fig. 3.28, and from examination of the macro structure and knowledge of the peak temperature distribution the fracture toughness testing positions indicated, 1 and 2, were considered to relate to peak temperatures of 650°C and 1000°C to 1460+°C respectively. The fracture toughness results for these positions are given in Table 3.16.

The difficulties encountered in measuring the submerged arc weld H.A.Z. tensile properties also occurred with the M.I.G. weld H.A.Z. measurements. Useful results could only be obtained from position 1, the region of reverted austenite. The mean limit of proportionality and ultimate tensile strength were found to be 116 tons per sq. in. and 121 tons per sq. in. respectively, with an elongation of 10% and 44% reduction of area.

3.6.4 Microhardness results

The microhardness measurements made across the H.A.Z.s of the submerged arc and M.I.G. welds are given in Figs 3.29 and 3.30 respectively. The results for the as welded plate and the aged plate are included for both weld H.A.Z.s. The results indicate that a region is present in both weld

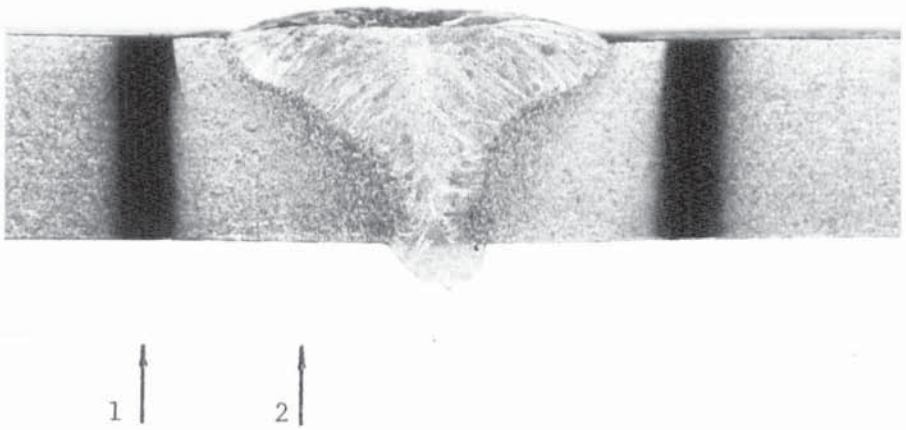

Fig. 3.28. Macro cross section of the M.I.G. weld and H.A.Z. Etchant 25% nitric acid. x 4.

Fracture toughness at various H.A.Z. positions ksi$\sqrt{in}$	
650°C	1000-1460+°C
64.2 71.0 65.8 63.1 66.7 70.4	57.5 59.1 58.9 60.6 57.4 60.0
Means: 66.9	58.9

Table. 3.16. The fracture toughness at various thermal cycle peak temperature positions in the M.I.G. weld H.A.Z.

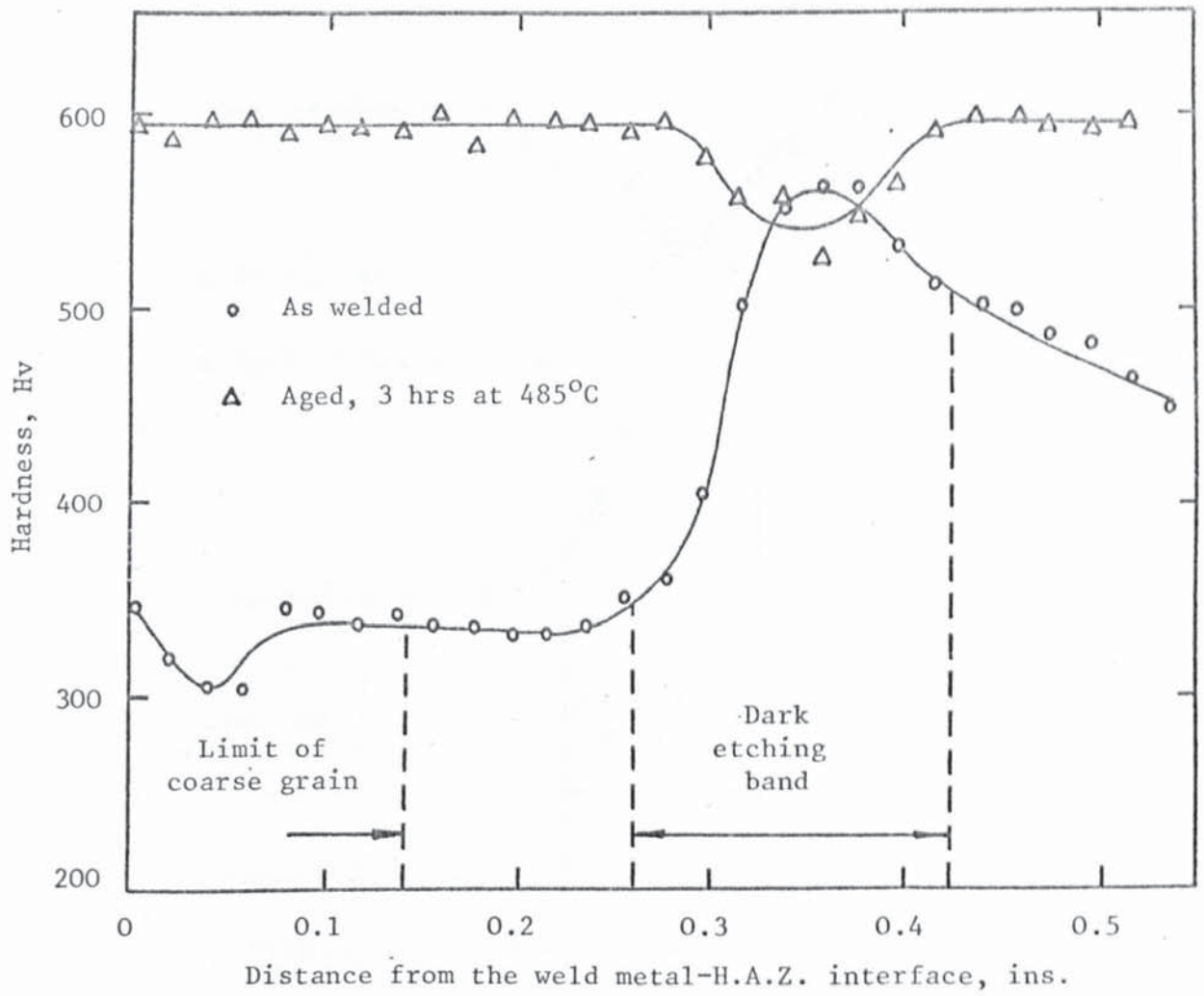

Fig. 3.29. Variation in hardness across the maraging steel submerged arc weld H.A.Z.

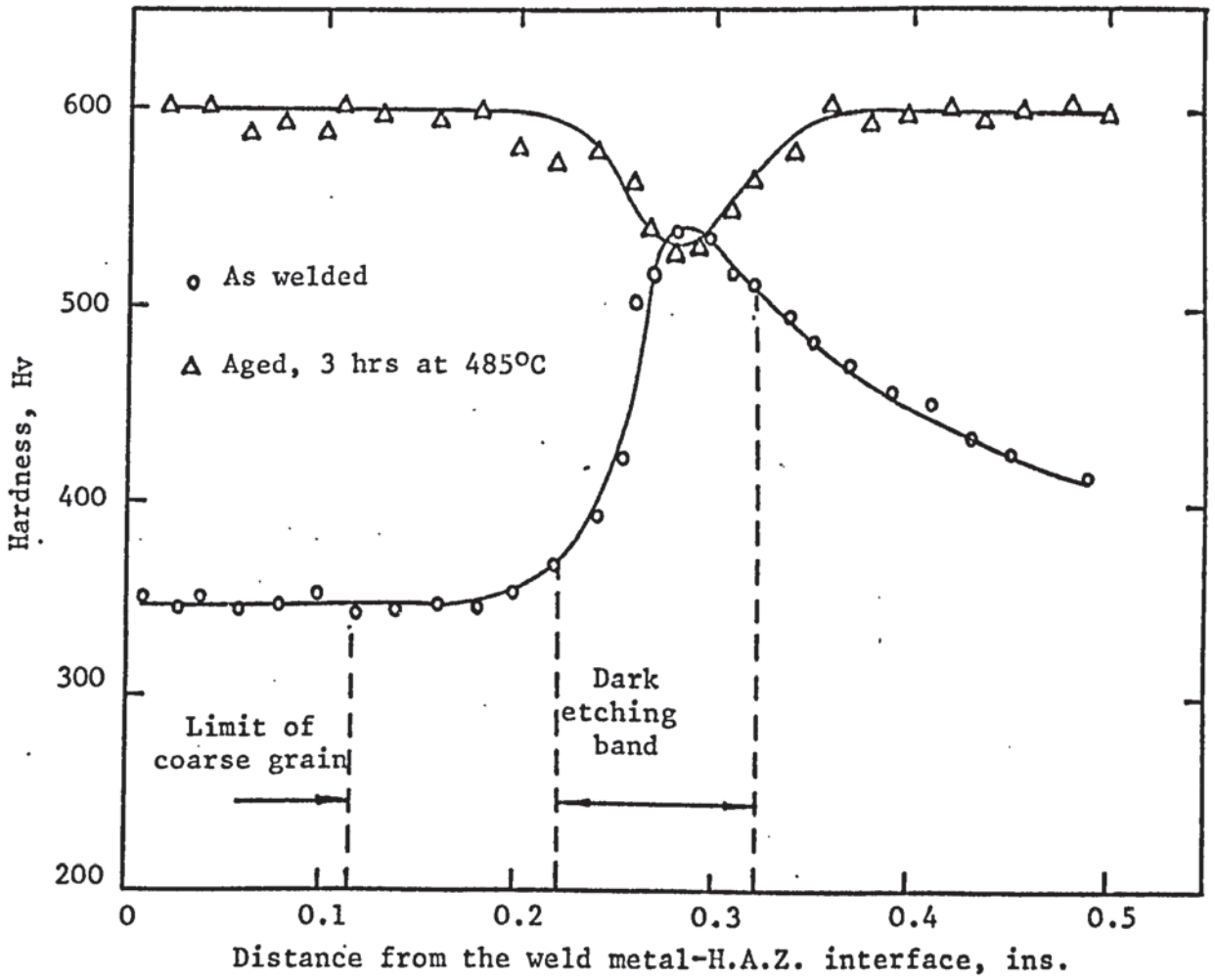

Fig. 3.30. Variation in hardness across the maraging steel M.I.G. weld H.A.Z.

H.A.Z.s where complete hardening has not occurred during ageing. The position of this region relates to the dark etching bands in each H.A.Z. and serves to indicate how the width of the H.A.Z. differs for the welding processes concerned.

3.7 Metallography and Fractography

3.7.1 Specimen preparation and examination

The fracture toughness specimens selected for metallographic examination from the simulated and real weld H.A.Z.s were machined to form $\frac{1}{2}$" squares containing the notch and fracture path across the centre. These were surface ground to half the tested thickness such that the fracture examined was from the plane strain region. The specimens were mounted in thermo setting compound and polished using conventional techniques. Repeated polishing and etching in 10% nital was found most suitable to reveal the microstructures. Preliminary metallographic examination was carried out using bench microscopes, and higher magnifications and photomicrographs were obtained using the Vickers projection microscope.

Examination of the simulated weld H.A.Z. structures was confined to the region immediately adjacent to the fracture path since this represents the central region of the temperature plateau produced during thermal cycling in the Gleeble. The real weld H.A.Z. structures were examined on a more general basis, particularly the regions close to the weld metal where, through the thickness of the specimen, the fracture path traverses a number of structures. Grain sizes were determined using the linear intercept method.

The scanning electron microscope, SEM, was used to examine fracture surfaces from fracture toughness specimens representative of each simulated and real weld H.A.Z. The microscope's specimen chamber and traversing controls were such that by sectioning the specimens $\frac{1}{8}$" from the parallel

to the fracture surface the full cross section could be examined complete. The specimens were prepared accordingly, ultrasonically cleaned and mounted in the conventional manner on SEM stubs.

The central region immediately ahead of the fatigue crack was examined in detail in each specimen since this represents the plane strain region of fracture. Since the specimens had produced plane strain results, the shear lips plane stress region was small in all cases, and in general about 70% of the cross sectional area consisted of plane strain fracture. The specimens taken from the real weld H.A.Z.s adjacent to and in some cases containing the weld metal were carefully examined at a number of positions realising that these related to different thermal cycle peak temperatures and structures. Photographic records were made of representative areas and features of the fracture surfaces and characteristic fracture measurements were taken from these records. In all cases photographs were taken with a specimen tilt angle of 45° and the direction of crack propagation from left to right.

3.7.2 X-ray diffraction analysis

This technique was used to detect and determine the quantity of the reverted austenite in the structures examined, in particular those that had experienced thermal cycle peak temperatures of $650^{\circ}C$. The object of this work was to relate fracture toughness and properties quantitatively to the volume fraction of reverted austenite. Metallographic techniques using the Quantimet were inadequate because of the fine dispersion of the phase and lack of distinct contrast with the matrix.

The basic principles of quantitative multiphase analysis using X-ray diffraction are outlined by Cullity[113]. The direct comparison method was used in this investigation, assuming the existence of only two phases, f.c.c. reverted austenite γ and b.c.c. martensite α. The integrated intensities I for any pair of diffracted lines can be related to the volume fractions V of the phases as follows

$$\frac{I_\alpha}{I_\gamma} = \frac{R_\alpha}{R_\gamma} \frac{V_\alpha}{V_\gamma} \qquad \ldots\ldots 3.6$$

where the values of the constants R depend on the Bragg angle θ, the diffracting plane hkl, and a number of other phase factors.

Any planes from the two phases can be selected for comparison, but for maximum accuracy it is usual to select those giving the greatest intensities as well as being of sufficiently different Bragg angle to have distinct intensity distributions. A number of full scans were carried out on two phase maraging steel specimens and it was found that using a chromium target the (110) b.c.c. and (111) f.c.c. reflections adequately satisfied the above criterion. The value of the constants has been obtained from published data for these planes in maraging steel[82] and equation 3.6 becomes

$$\frac{I_\alpha}{I_\gamma} = 1.316 \frac{V_\alpha}{V_\gamma} \qquad \ldots\ldots 3.7$$

This assumes a completely random structure, but since most materials contain crystallographic texture it was necessary to account for this factor.

A Siemens X-ray diffractometer with a wide angle goniometer was used and K_α radiation generated from a chromium target using an accelerating voltage of 30 Kv and tube current of 14 MA. Integrated intensity measurements were made using a step scanning system, counting for 6 secs every 0.02°. To determine the texture of the parent material a composite specimen was prepared from sections of the parent plate selected at random. The integrated intensities for a number of planes were compared with the integrated intensities from a known random sample and a "times random" factor was determined for each plane. Only b.c.c. reflections were detected from the parent material and the factor for the (110) reflection was found to be 1.22, indicating that values of I_α for this plane were 22% too large. The texture of the reverted austenite was not determined because only one strong peak was detected. However, since it forms as a result of segregation and diffusion it was considered to be random.

Taking texture into account equation 3.7 becomes

$$\frac{V_\alpha}{V_\gamma} = \frac{0.82}{1.316} \cdot \frac{I_\alpha}{I_\gamma} \qquad \ldots\ldots 3.8$$

I_α and I_γ can be measured and the right hand side of equation 3.8, say Z, determined. Knowing that

$$V_\alpha + V_\gamma = 1 \qquad \ldots\ldots 3.9$$

then the volume fraction of reverted austenite can be determined from

$$V_\gamma = \frac{1}{(Z + 1)} \qquad \ldots\ldots 3.10$$

The specimens for X-ray diffraction analysis were selected on the basis of the metallographic findings and fracture toughness results. Both sides of the completely broken fracture toughness specimens were used to provide sufficient material for a strong reflection hence increasing the accuracy of the analysis. The fractured ends were cut from the bend specimens and the fracture surfaces carefully ground back until the sides of the machined notch were just skimmed. The two sides were then mounted to provide a $\frac{1}{2}$" square specimen. This was polished and heavily etched in 10% nital prior to positioning on the goniometer specimen stage for analysis.

3.7.3 Parent material structures

For the purpose of comparison with H.A.Z. structures, more detail concerning the parent material was necessary. Grain size measurements on the as received material were difficult, but after ageing the prior austenite grain boundaries became more apparent as shown in Fig. 3.31(a). The grain size varied from 30μ to greater than 100μ with the average value being 50μ. Metallographic examination of the fracture revealed a ductile dimple form of crack propagation as shown in Fig. 3.31(b). The dimples varied in length between 5μ and 10μ and in general were less than 5μ wide. The fracture path deviated little from one plane and appeared unaffected by any microstructural features.

Examination of the fracture surfaces clearly revealed the ductile dimples. The fractures were macroscopically

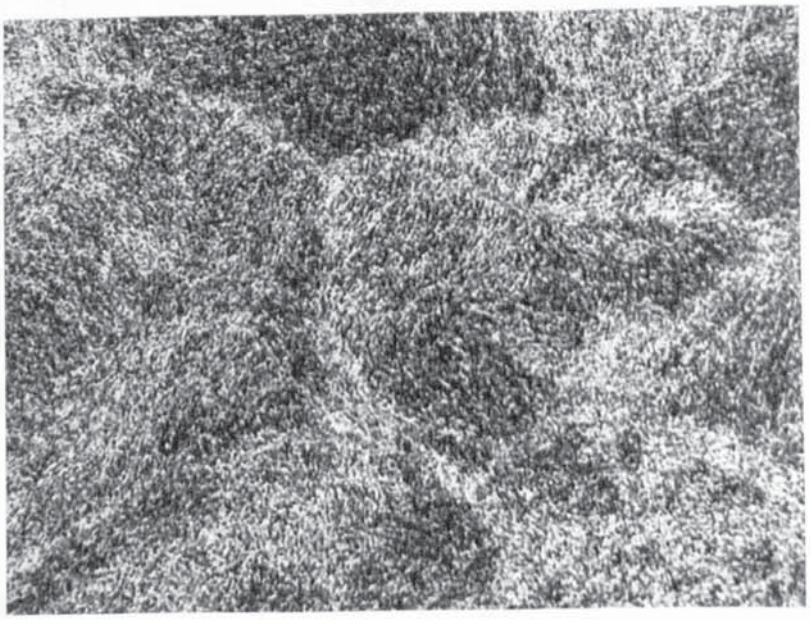

(a) General microstructure

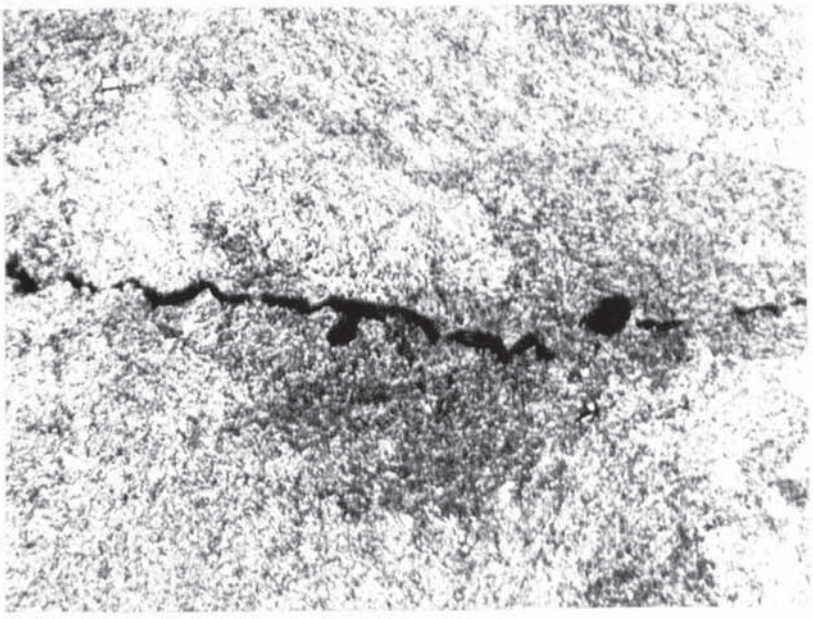

(b) Fracture path through the microstructure

Fig. 3.31. Aged parent material martensitic structures. Etchant 10% Nital. x 500.

flat, apart from some abrupt changes in topography associated with stringers of inclusions. The dimpled size measured metallographically was not readily detected in the fracture surface, Fig. 3.32(a), but at higher magnification a uniform dimple size of about 1μ was found throughout the fracture surface, Fig. 3.32(b).

3.7.4 Reverted austenite structures

The simulated weld H.A.Z.s involving thermal cycles to peak temperatures of 650°C were found to contain considerable amounts of a white etching phase. X-ray diffraction confirmed this phase to be austenite, and since it formed on heating to below the transformation temperature it was concluded to be reverted austenite. The morphology of the phase appeared to be independent of the welding parameters simulated, and structures typical of its mottled and ribbon like appearance are shown in Fig. 3.33. The parent materials prior austenite grain size was unaffected by thermal cycling to 650°C.

Metallographic examination revealed no direct relationship between fracture path and microstructure. In all cases crack propagation occurred by the formation and coalescence of dimples, appearing the same as in the parent material. In some cases the dimples were clearly formed and of the same size as those in the parent plate, but others were less well defined.

Scanning electron microscopy of the fracture surfaces revealed the dimpled structure as expected. As with the metallographic examination, the fracture appearance was relatively constant irrespective of the welding parameters

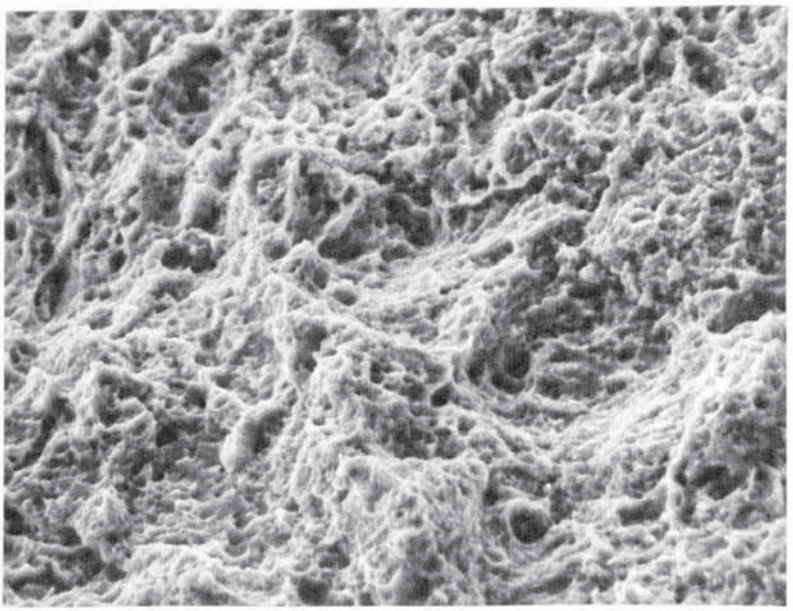

(a) x 700

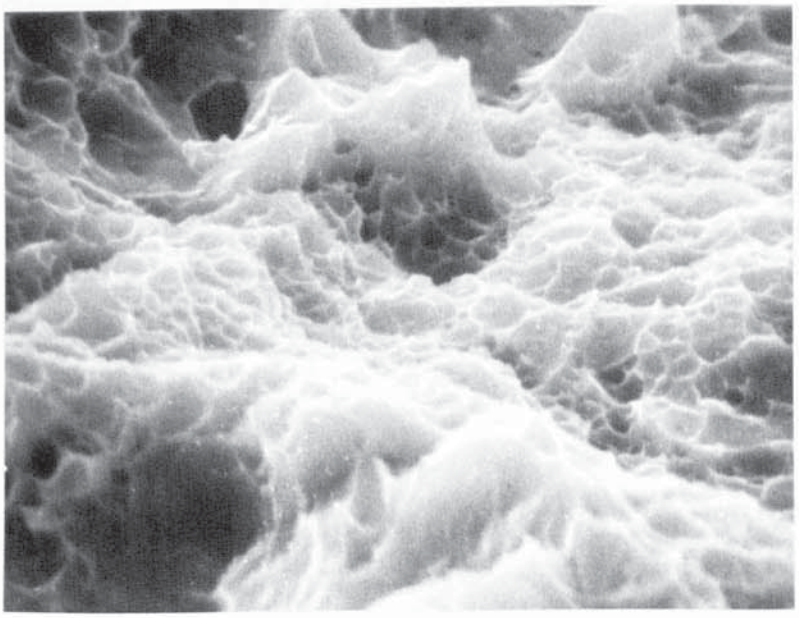

(b) x 7000

Fig. 3.32. Scanning electron micrographs of the fracture surface of aged parent material.

(a) Micro plasma 2

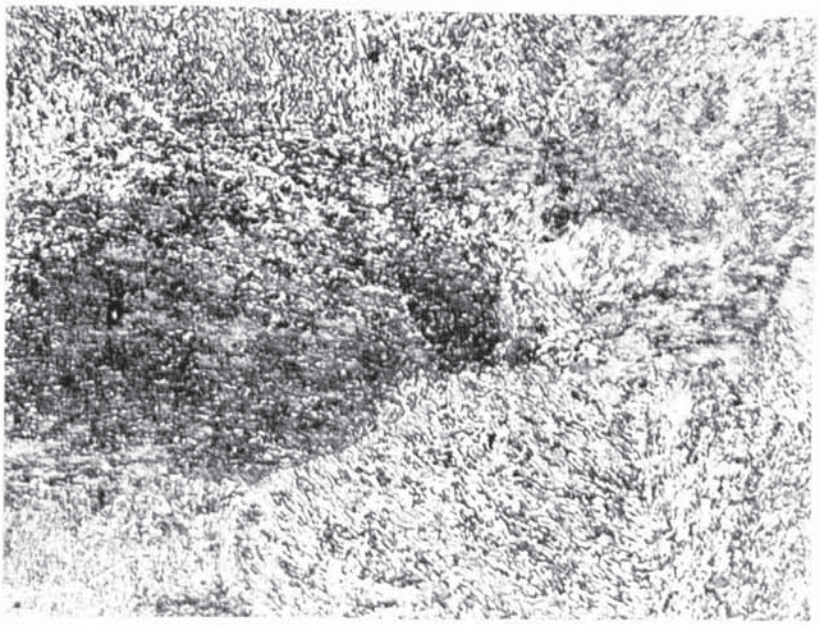

(b) TIG 3

Fig. 3.33. Simulated weld H.A.Z. microstructures. Thermal cycle peak temperature 650°C. Etchant 10% Nital, x 500

simulated. Typical examples of the fractures are shown in Fig. 3.34. There appeared to be two groups of dimples, larger dimples similar in size to those measured metallographically and smaller dimples throughout the fracture surface about 1μ and less in size. There was no evidence from the fracture surfaces to suggest that crack propagation had occurred preferentially through reverted austenite or martensite, or indeed that two phases were present in the structures.

Specimens taken from the real weld H.A.Z.s that experienced peak temperatures of 650°C revealed microstructures and fractures identical to the simulated weld H.A.Z. specimens. Typical microstructures are shown in Fig. 3.35 and the mottled and ribbon like appearance of the reverted austenite is readily apparent. Fracture through these structures was by ductile dimple formation and as previously was unaffected by the distribution of the phases. The predominant dimple size was 1μ as shown in the typical fractures in Fig. 3.36, and larger dimples were not apparent.

From earlier results, given in Fig. 3.21, it appeared that fracture toughness was independent of the welding parameters simulated. Nevertheless, it was considered that within the scatter of results obtained a relationship might be found to exist between the volume fraction of reverted austenite and fracture toughness. Consequently, X-ray diffraction analysis was carried out on a number of specimens of different fracture toughness from simulated and real weld H.A.Z.s. The results of this analysis are given in Table 3.17. Regression analysis was carried out on these results

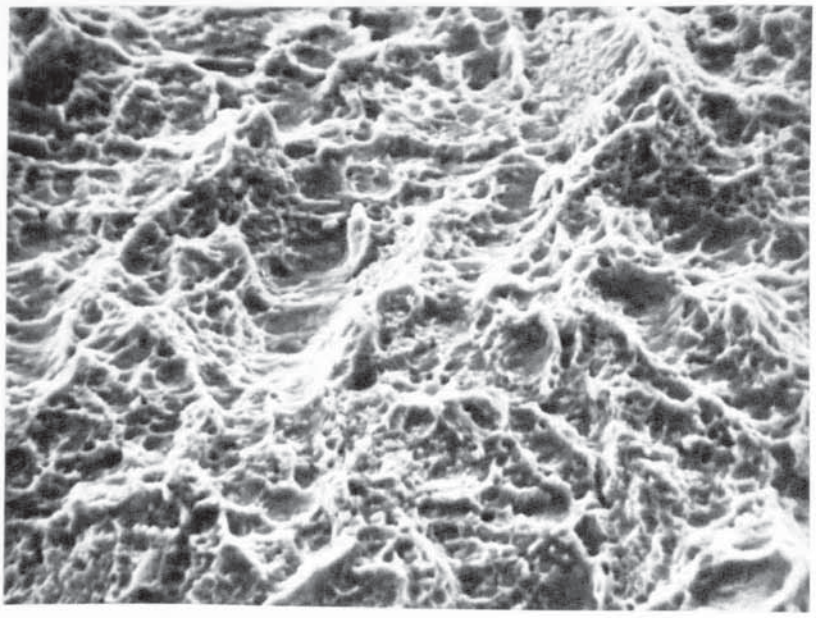

(a) Micro plasma 2

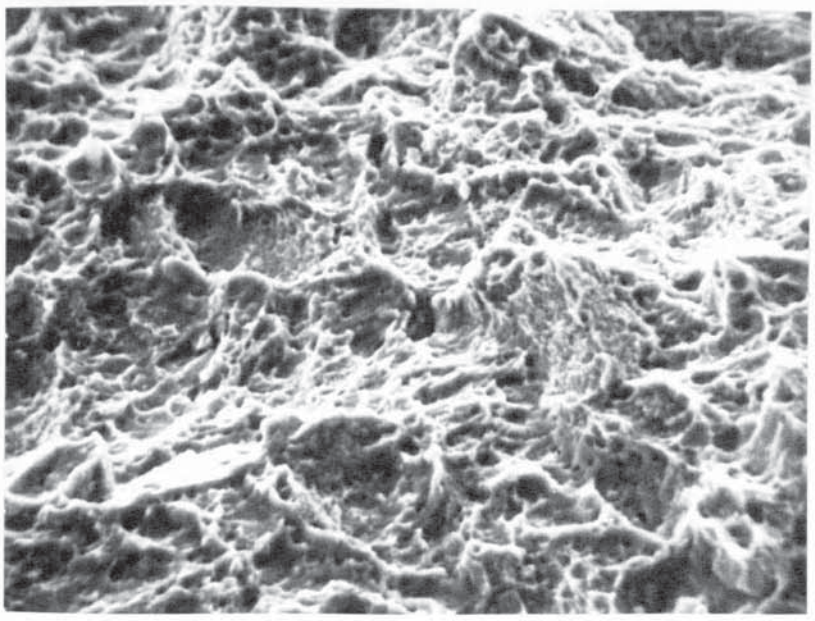

(b) TIG 4

Fig. 3.34. Scanning electron micrographs of fractures in simulated weld H.A.Z. structures. x 1500.

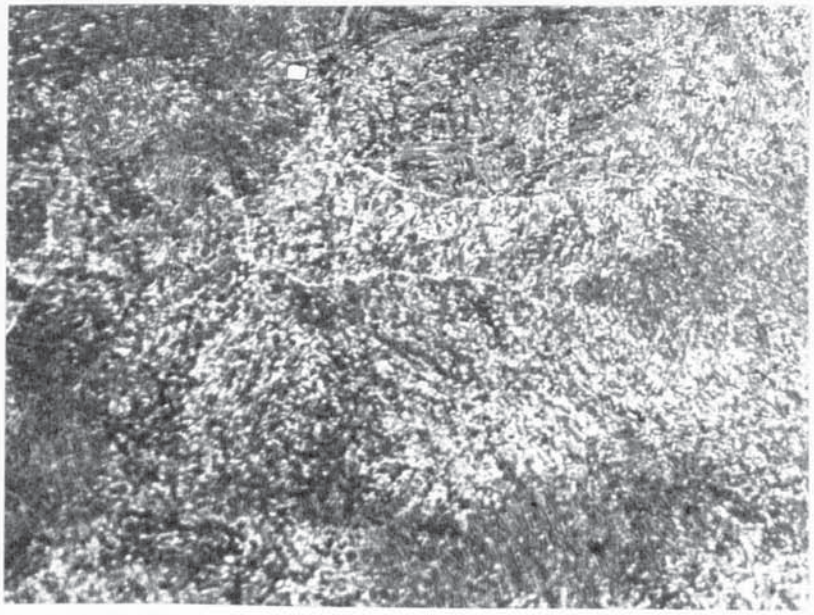

(a) Submerged arc

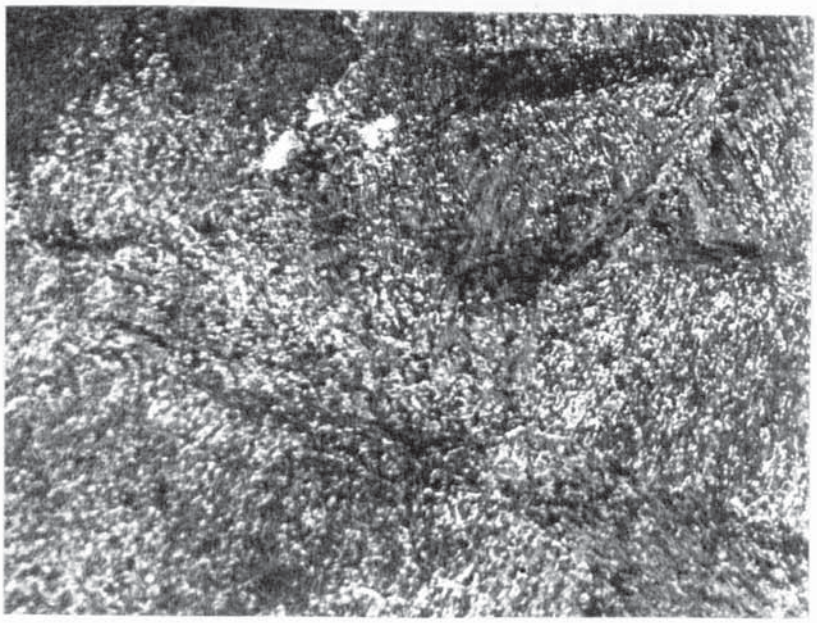

(b) M.I.G.

Fig. 3.35. Real weld H.A.Z. microstructures. Thermal cycle peak temperature 650°C. Etchant 10% Nital. x 500.

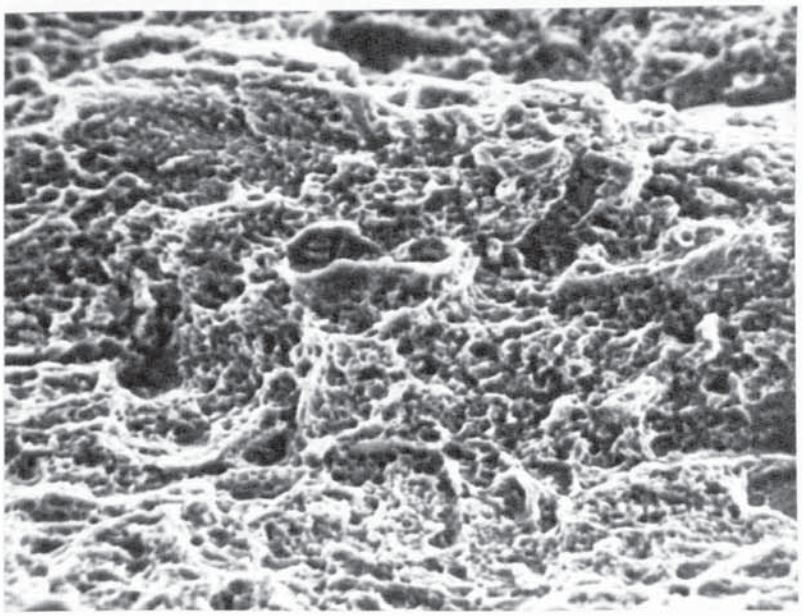

(a) Submerged arc

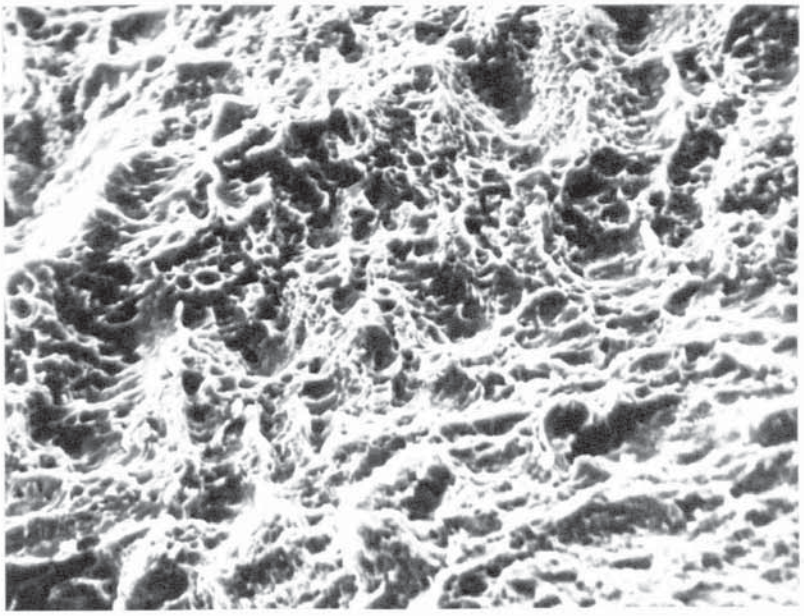

(b) M.I.G.

Fig. 3.36. Scanning electron micrographs of real weld H.A.Z. fractures. Thermal cycle peak temperature 650°C. x 1500.

Welding Parameters	Vol. γ %	K_{Ic} ksi$\sqrt{in}$	Heating rate ^{o}C per sec.
MP 1	17.3	67.9	80
MP 2	7.9	64.2	200
TIG 1	11.8	64.7	64
TIG 1	29.8	64.2	64
TIG 3	42.2	76.6	7
TIG 3	53.7	70.4	7
TIG 4	28.2	75.7	50
MIG 2	17.4	59.5	76
MIG 3	32.5	73.1	98
Sub. arc	17.5	73	22
Elect. beam	14.9	71.2	70
Real sub. arc	18.2	66	30
Real MIG	22.5	66.7	55

Table 3.17. The volume fraction of reverted austenite in a number of simulated and real weld H.A.Z. microstructures.

and between K_{Ic} and austenite content a correlation coefficient of 0.495 was obtained. This is significant at the 10% level but not at the 5% level. Between heating rate and austenite content the correlation coefficient was -0.577 which is significant at the 5% level and indicates that with increasing heating rate the austenite content decreases.

3.7.5 High temperature structures

A number of the same characteristic features were observed in all the specimens thermally cycled to peak temperatures of 1200°C, 1325°C and 1400°C. For continuity, the findings associated with each temperature will be considered separately.

All the structures produced by thermally cycling to 1200°C contained an acicular matrix and well defined prior austenite grain boundaries as shown in Fig. 3.37(a). The acicular matrix often had several different orientations, giving rise to domains within the prior austenite grain boundaries. A considerable variation in grain size was found in individual specimens, but in general the grain size decreased with increased heating rate. For the range simulated, mean values from 15μ to 30μ were measured. The domain boundaries were less distinct and consequently an accurate assessment of the domain size was not possible. The inclusions appeared unaffected by thermal cycling and although the prior austenite grain boundaries were well defined, no evidence of constitutional liquation of the inclusions or grain boundary embrittlement was detected in any of the specimens.

(a) General microstructure

(b) Fracture path through the microstructure

Fig. 3.37. Simulated weld H.A.Z. microstructures. Thermal cycle peak temperature 1200°C. Etchant 10% Nital. x 500.

The fractures were more undulating in these structures than any previously examined, as shown in Fig. 3.37(b). The fracture path appeared to be deflected in some areas by the acicular matrix, but exhibited no preference for grain boundaries or inclusions. In general the dimples were 5μ to 10μ long and no greater than 5μ wide. In places the dimples appeared unconnected, but at higher magnifications and with extra etching this was found to be associated with a phase similar in morphology to the ribbon like reverted austenite. This phase was dispersed throughout the matrix and was not found preferentially at the prior austenite or domain boundaries. Globular white areas, with the same etching characteristics as the ribbon like phase, and similar to those in the aged parent material were also observed.

The white etching phase in the parent material was considered to be reverted austenite, but this identification was not positive. Consequently, the ribbon like phase in the 1200^{o}C structures was considered to have a number of possible origins. Firstly, the redistribution of alloy concentration from the original material into a more acicular form could give rise to ribbon like reverted austenite on ageing. Secondly, if any of the globular regions in the original material were titanium carbide then the ribbon like phase could be due to constitutional liquation of these inclusions. In this case, the ribbons could be either films of titanium carbide or films of austenite resulting from the concentration of titanium in these areas. This enrichment might be sufficient to produce retained austenite or may only give rise to reverted austenite on

ageing. Only aged structures were available for examination and consequently it was not possible to determine if the ribbon like phase was present before or only after ageing. Thirdly, even if titanium carbides were not present, some undetected dissociation or constitutional liquation of the remaining inclusions might have resulted in the ribbon like phase.

X-ray diffraction analysis failed to detect any austenite in these structures. Electron probe microanalysis was applied to regions containing the ribbon like phase, but because the phase was so narrow, less than 1μ, no evidence of the elements present was detected. Consequently, it was not possible from these microstructures to confirm any of the suspected mechanisms of formation of the ribbon like phase.

The fracture surfaces revealed a dimple size of 10μ, shown typically in Fig. 3.38(a). A particular advantage of the scanning electron microscope was found to be that the role of the inclusions actually associated with the fracture process could be studied in more detail and quantity than was possible from any one metallographic section. The inclusions generated larger dimples, Fig. 3.38(b), but no evidence of constitutional liquation or brittle films was found in any of the fracture surfaces. In some areas the fracture had a flatter, "intergranular" appearance, Fig. 3.38(c), but at higher magnifications these areas were found to consist of small ductile dimples about 1μ in size, Fig. 3.38(d). It was considered that these areas related to the fracture path following the white etching ribbons

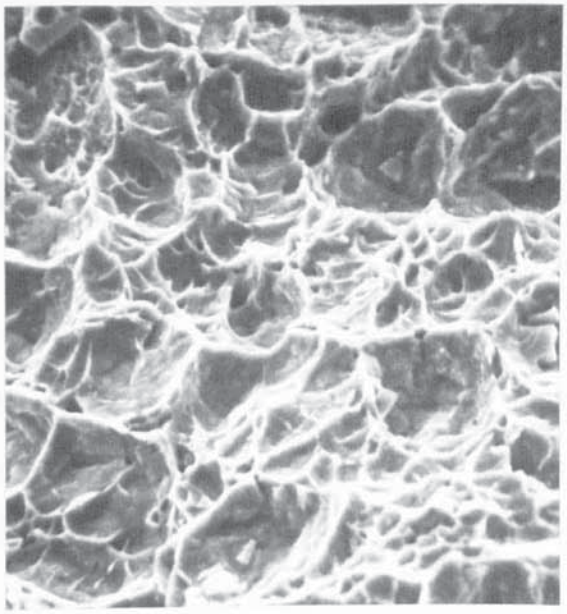

(a) General dimpled fracture. x 1500

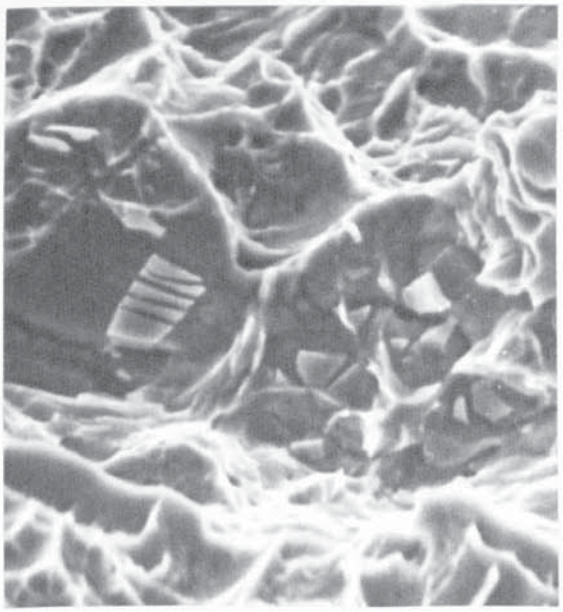

(b) Inclusion in the fracture. x 2500

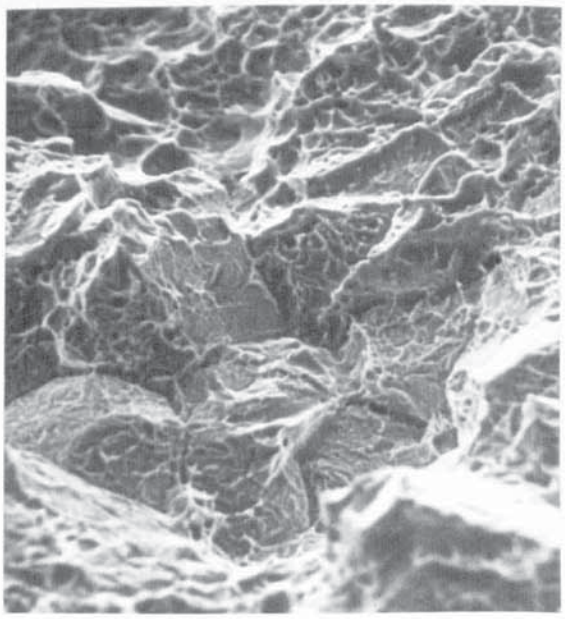

(c) Flatter "intergranular" fracture. x 700

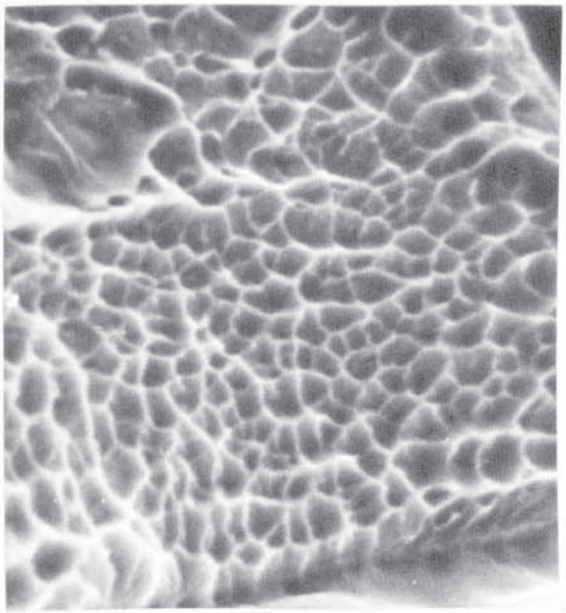

(d) Dimples in(c). x 7000

Fig. 3.38. Scanning electron micrographs of fracture features in simulated weld H.A.Z.s. Thermal cycle peak temperature 1200°C.

observed in the structures. Consequently, the ductile appearance of the fracture indicated that the ribbons were austenite and not brittle titanium carbide or titanium sulphide films. Nevertheless, the mechanism of formation of these ribbons was still not apparent.

The features observed in the specimens thermally cycled to 1325°C were similar to those observed in the 1200°C structures. The prior austenite grain size was generally greater and mean values of 27μ, 44μ and 56μ were measured for the decreasing heating rates simulated. A typical microstructure and fracture path are shown in Fig. 3.39. The ribbon like white etching phase was more abundant than in the 1200°C structures, and appeared to increase with decreasing heating rate. In some cases it appeared unrelated to any other features, as can be seen in the central regions of Fig. 3.39(a) and in Fig. 3.40(a) where it connects two large dimples in the fracture path. However, in other areas it was found to be directly related to the titanium sulphide inclusions, as shown in Fig. 3.40(b), indicating that constitutional liquation and dissociation of these inclusions had occurred. No evidence of constitutional liquation of the titanium carbonitrides was detected.

The morphology of the ribbon like phase indicated that it formed either at the prior austenite grain boundaries or at the domain boundaries. However, as can be seen in Figs 3.39 and 3.40, this was not apparent from the room temperature structures. Also, even though constitutional liquation was detected in these structures, there was no evidence of grain boundary embrittlement. The fracture path was

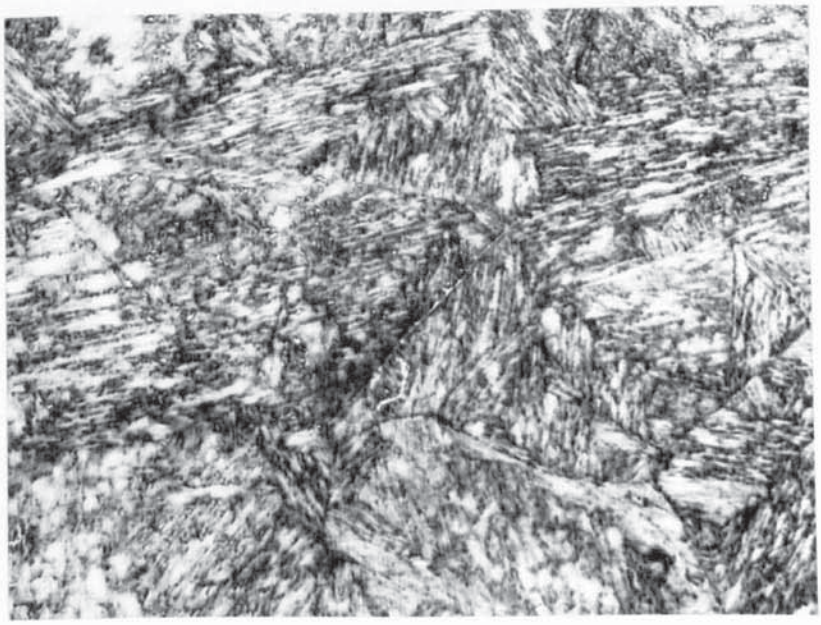

(a) General microstructure

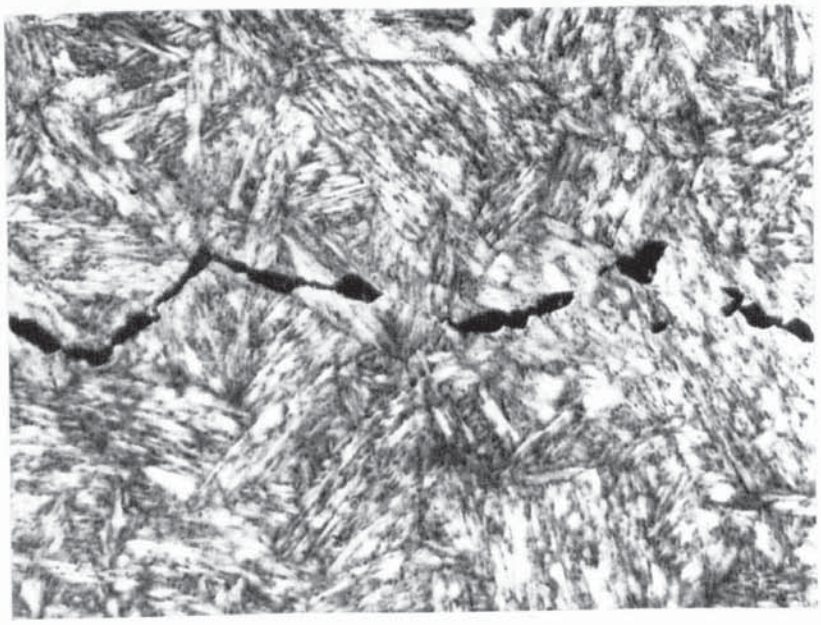

(b) Fracture path through the microstructure

Fig. 3.39. Simulated weld H.A.Z. microstructures. Thermal cycle peak temperature 1325°C. Etchant 10% Nital. x 500.

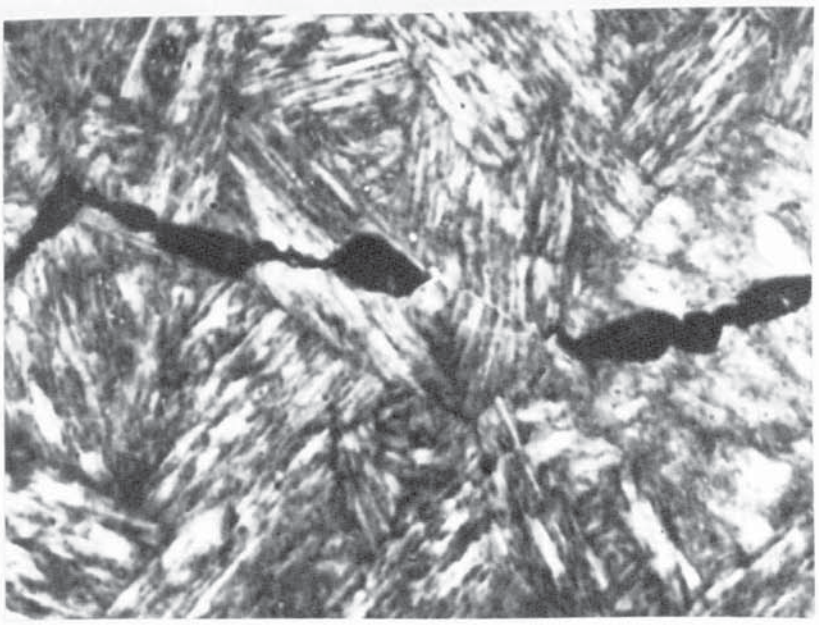

(a) Associated with the fracture path

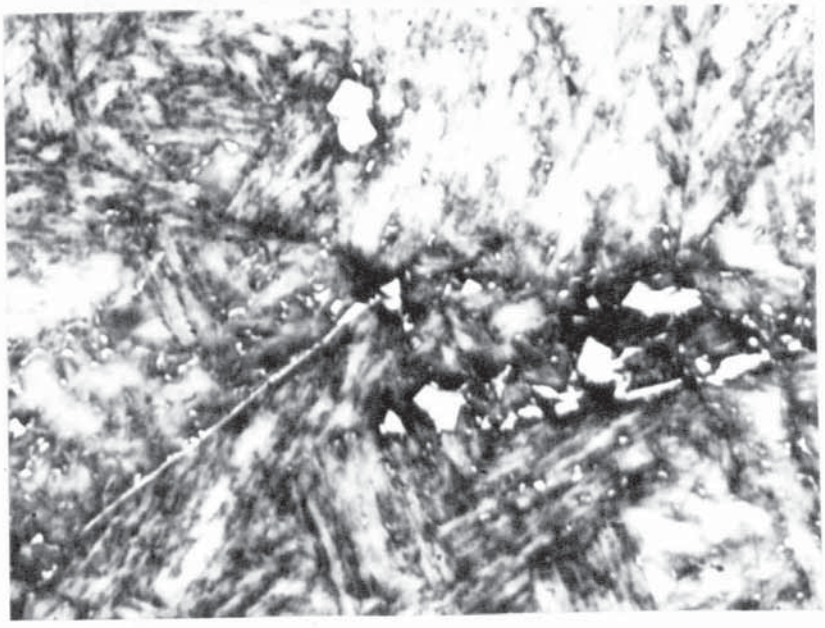

(b) Associated with a group of inclusions

Fig. 3.40. White etching phase present in simulated weld H.A.Z. microstructures. Thermal cycle peak temperature 1325°C. Etchant 10% Nital. x 1000.

undulating, as in the 1200°C structures, and appeared to be deflected by both the acicular matrix and the white etching ribbons, but exhibited no preference for the prior austenite grain boundaries.

In the 1200°C structures, the ribbon like phase was not directly related to any inclusions. Consequently, it was not possible from the microstructure alone to determine if the ribbons were simply liquated inclusions or films of austenite as a result of liquated inclusions. In the 1325°C structures these two features were directly related and since the ribbons etched white and the inclusions etched grey, it was considered that the ribbons were austenite. Further evidence to support this was sought using X-ray diffraction but only body centred cubic reflections were detected and it was not possible to identify the phase as austenite or quantify the contents. However, using an ARL electron probe micro-analyser it was found that the sulphur and carbon X-ray images clearly depicted the titanium sulphide and titanium carbonitride inclusions, but did not reveal the ribbon like phase. Spot analyses on the ribbon like phase and local matrix indicated variations in titanium contents, with mean values of 0.97% and 0.90% being obtained for the ribbon like phase and matrix respectively. Titanium concentrations have been shown to correspond to areas of reverted austenite[84]. Consequently, whilst the electron probe evidence was not conclusive it was considered to indicate that the ribbon like phase could be austenite, as previously suggested on the basis of its etching characteristics.

The fracture surfaces, Fig. 3.41(a), contained dimples ranging from 5μ to 10μ in size. Distinct evidence of constitutional liquation was not detected at all the inclusions, as can be seen in Fig. 3.41(b), but the increased amount of ribbon like phase observed metallographically was reflected in an increasing proportion of flatter "intergranular" fracture, Fig. 3.41(c). At higher magnifications this revealed a fine dimpled structure, Fig. 3.41(d), indicating that these areas were ductile and supporting the suggestion that the ribbon like phase was austenite. Attempts were made to analyse the flatter fracture surfaces using an electron probe attachment to the scanning electron microscope. However, due to severe undulations of the fracture surface no results were obtained that were comparable with the metallographic electron probe results.

The general features of the structures produced by thermal cycles to peak temperatures of 1400°C, Fig. 3.42(a), were as described for the 1200°C and 1325°C cases, with a number of notable differences in detail. The prior austenite grain size varied considerably throughout, but mean values of 35μ, 54μ and 66μ were obtained for the fast, intermediate and slow heating rates respectively. The fracture paths through these structures differed considerably from those through the other high temperature structures. Dimple formation was difficult to distinguish in many areas of the microsection although in places the fracture was 10μ wide. The fracture path appeared to be strongly dependent on the orientation of the acicular matrix, Fig. 3.42(b), and was more undulating than any previous case. No preference was

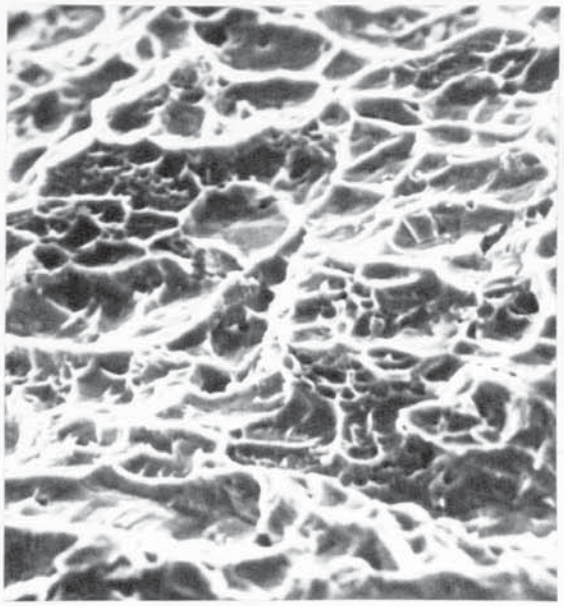

(a) General dimpled fracture x 1500

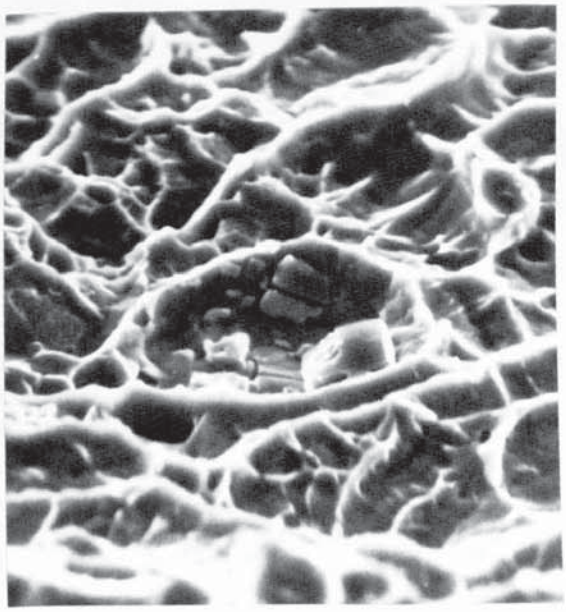

(b) Inclusions in the fracture x 3000

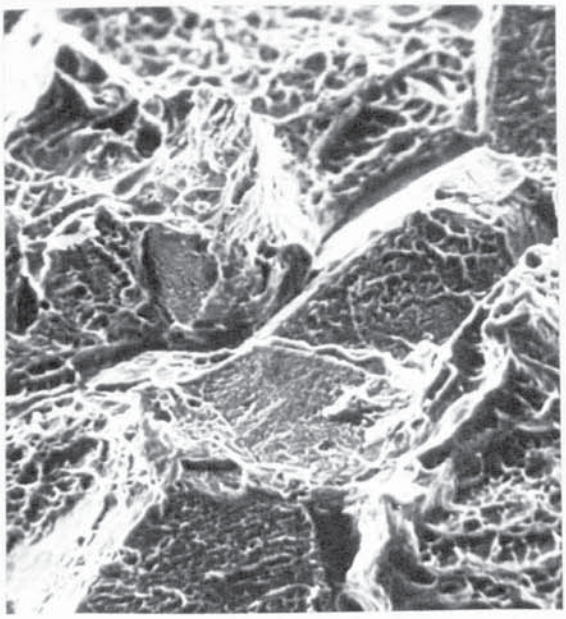

(c) Flatter "intergranular" fracture. x 700

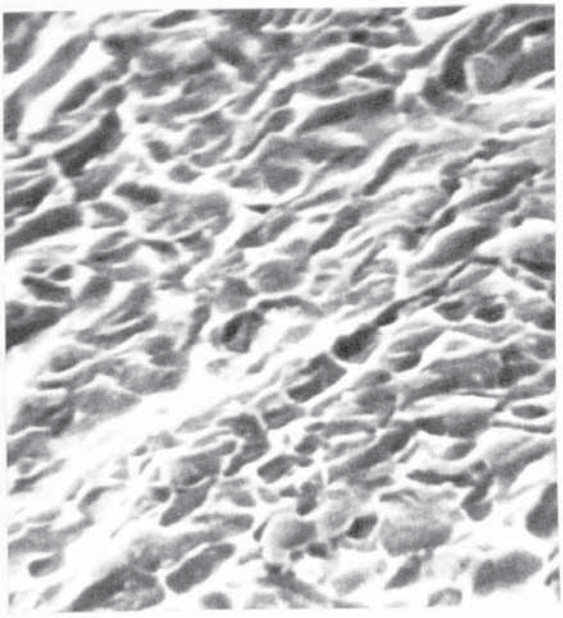

(d) Dimples in (c). x 7000

Fig. 3.41. Scanning electron micrographs of fracture features in simulated weld H.A.Z.s. Thermal cycle peak temperature 1325°C.

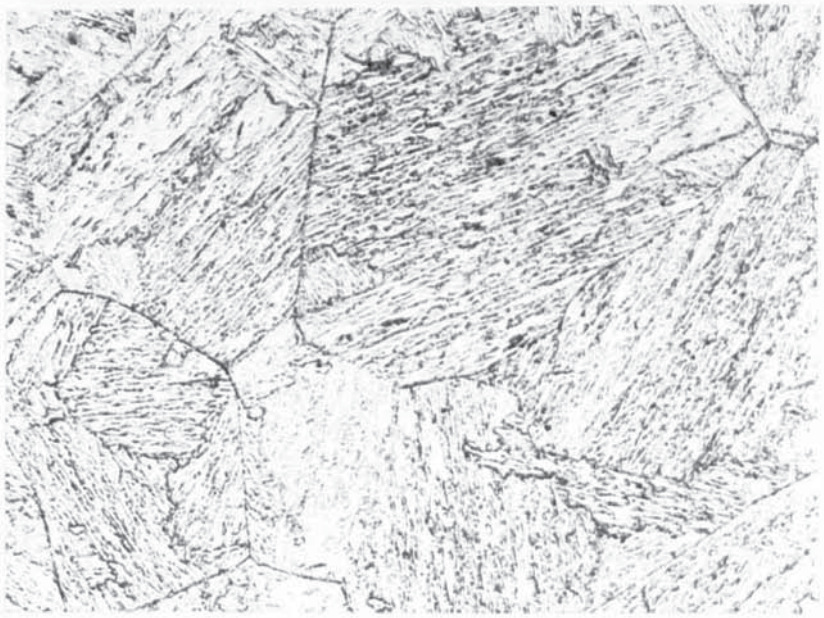

(a) General microstructure

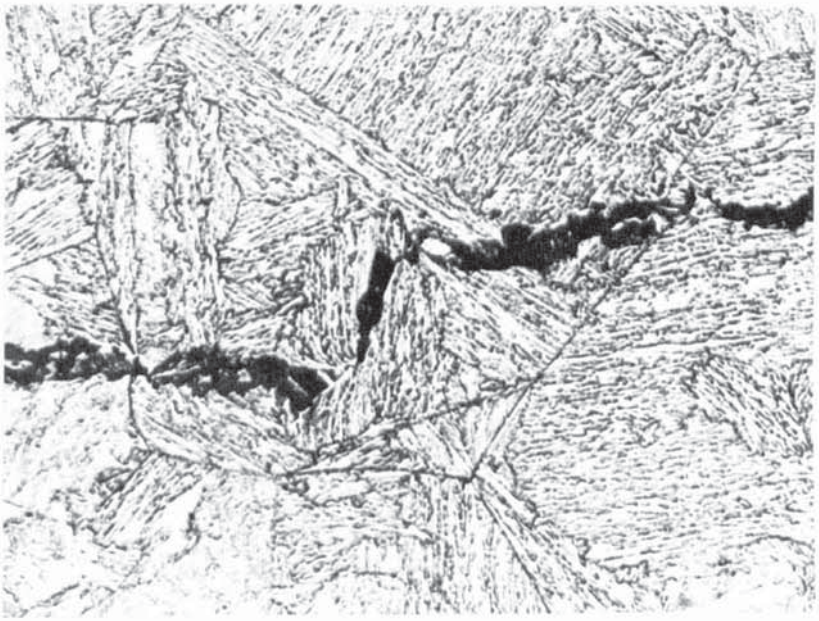

(b) Fracture path through the microstructure

Fig. 3.42. Simulated weld H.A.Z. microstructures. Thermal cycle peak temperature 1400°C. Etchant 10% Nital. x 500.

exhibited by the fracture path for the prior austenite grain boundaries and no evidence of bittle grain boundary films was detected.

The ribbon like phase was found in some areas, but to a much lesser extent than in the 1325°C structures. Similarly, the number of titanium sulphide inclusions observed was less than in the previous structures. Some remaining evidence of constitutional liquation of these inclusions was detected with small particles of the grey etching inclusions being found in white etching pools as shown in Fig. 3.43(a). Even where these areas of constitutional liquation were close to the fracture, Fig. 3.43(b), the fracture path was not attracted along the grain boundary, providing further evidence that grain embrittlement had not occurred. Some indication that constitutional liquation of the titanium carbonitrides had started was observed in these structures, as shown in Fig. 3.43(c). However, neither the white etching ribbon like phase or grain boundary embrittlement was associated with these inclusions.

The fracture surfaces revealed clearly defined dimples in some areas, Fig. 3.44(a), varying between about 5μ and 10μ in size. Very little evidence of the flatter "intergranular" fracture associated with the ribbon like phase was detected. In areas where the flatter fracture was found, it had less of an "intergranular" appearance and often contained titanium sulphide inclusions, Fig. 3.44(b). These areas were considered to relate to the regions in the microstructures where complete liquation of the inclusions had not occurred. However, the most striking feature of the

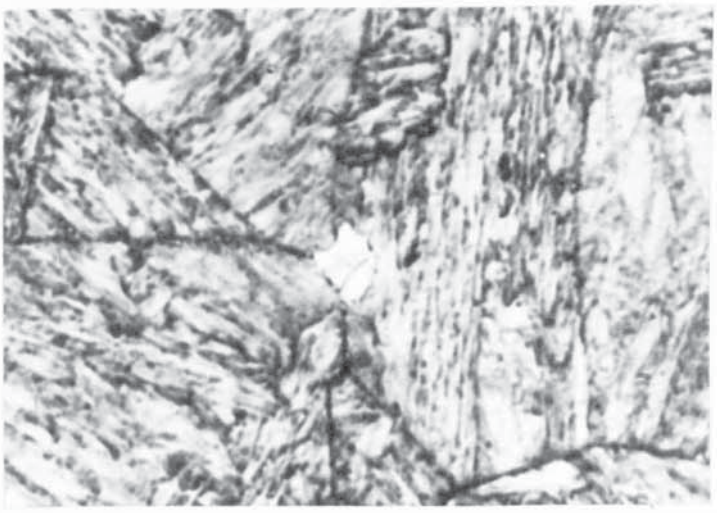

(a) Titanium sulphide

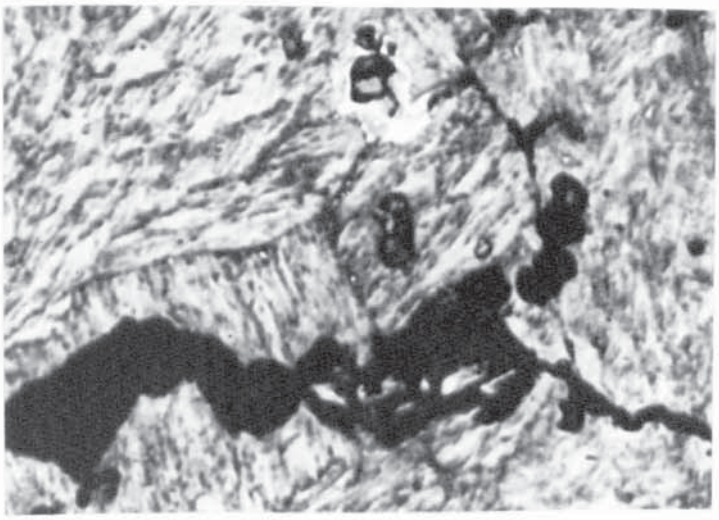

(b) Titaniumsulphide adjacent to fracture path

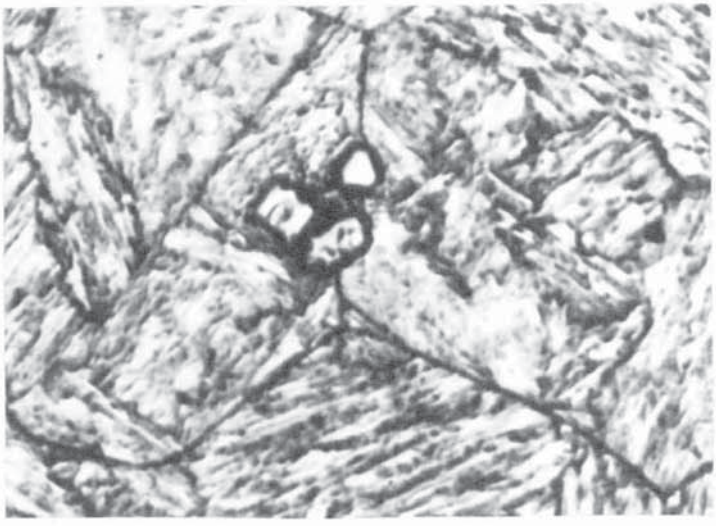

(c) Titainium carbonitride

Fig. 3.43. Constitutional liquation of inclusions in simulated H.A.Z.s. Thermal cycle peak temperature 1400°C. Etchant 10% Nital. x 1000.

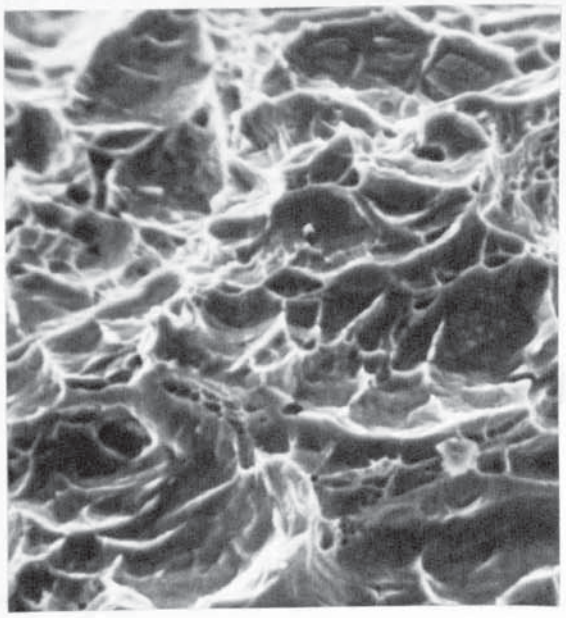

(a) Dimpled fracture. x 1500

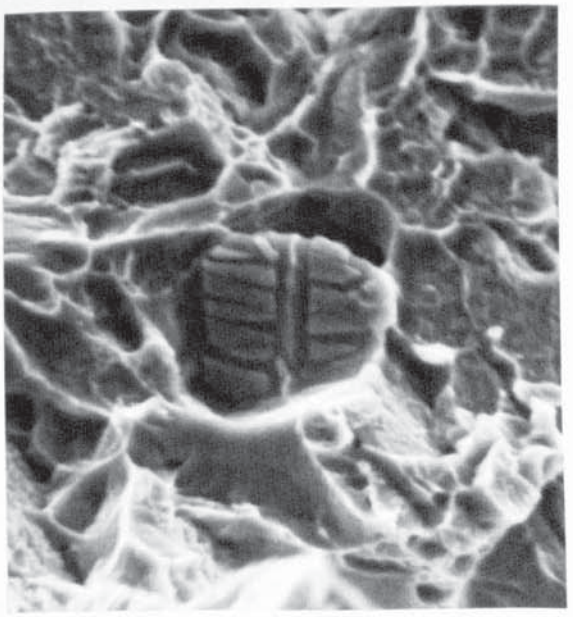

(b) Inclusions in the fracture. x 3000

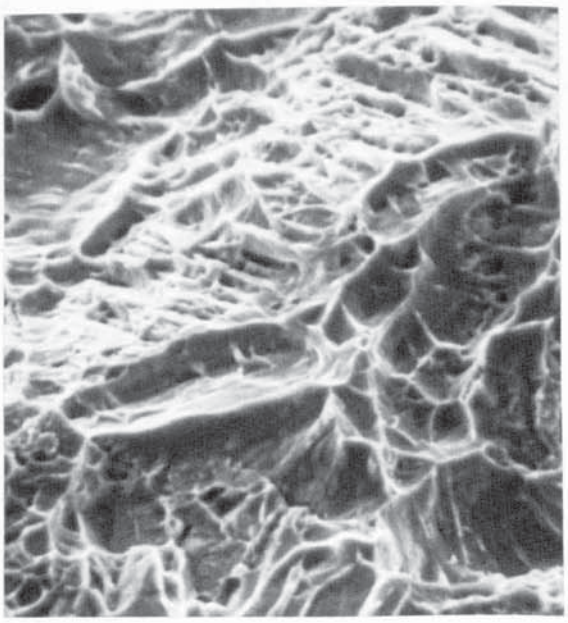

(c) & (d) Acicular appearance of the fracture surface.
x 1500

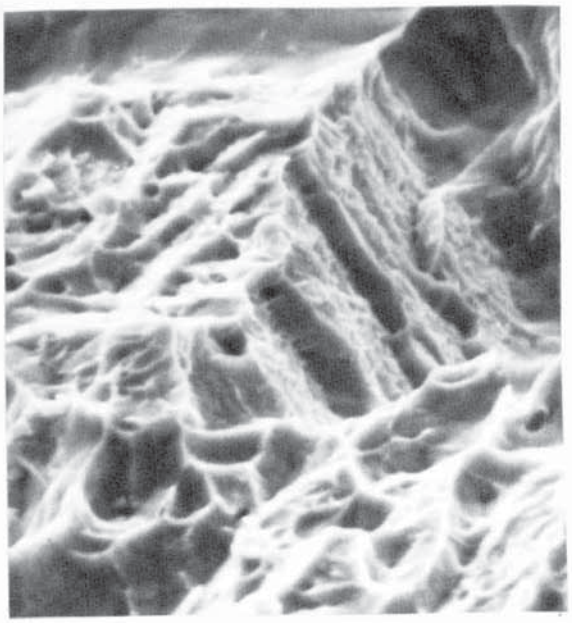

x 3000

Fig. 3.44. Scanning electron micrographs of fracture features in simulated weld H.A.Z.s. Thermal cycle peak temperature 1400°C.

fracture surfaces was that they were more undulating than in any previous case and in places had an acicular, but still dimpled, appearance as can be seen in Fig. 3.44(c) and (d). These features were considered to relate directly to the fracture path and structures observed metallographically.

The features observed in the simulated weld H.A.Z.s were also found in the real weld H.A.Z.s. The high temperature region of the submerged arc weld H.A.Z. and the weld metal are shown in Fig. 3.45(a) and the acicular matrix and prior austenite grain boundaries of the H.A.Z. are clearly defined. The grain size varied across the H.A.Z. and although it was difficult to relate directly to peak temperature, over the range from about 1000°C to 1400°C it increased from 20 to 70 on average. Immediately at the fusion boundary, in the peak temperature region of 1460°C+, there appeared some restriction on the grain size. An abundance of white etching weld metal phase was present in this area and in places had penetrated the H.A.Z.

Constitutional liquation of the titanium sulphide inclusions was observed in the acicular structures, as shown in Fig. 3.45(b). It was difficult to relate any particular region to an exact peak temperature, but the white etching ribbons were not observed close to the fusion boundary where temperatures in excess of 1400°C were experienced. In this region however, some evidence of constitutional liquation of the titanium carbonitride inclusions was detected, but in the remainder of the H.A.Z. these inclusions appeared unaffected by the thermal cycles. No evidence of hot cracking was detected in any region of the H.A.Z., and the fracture path

(a) General structure of the weld metal-H.A.Z. interface. x 150.

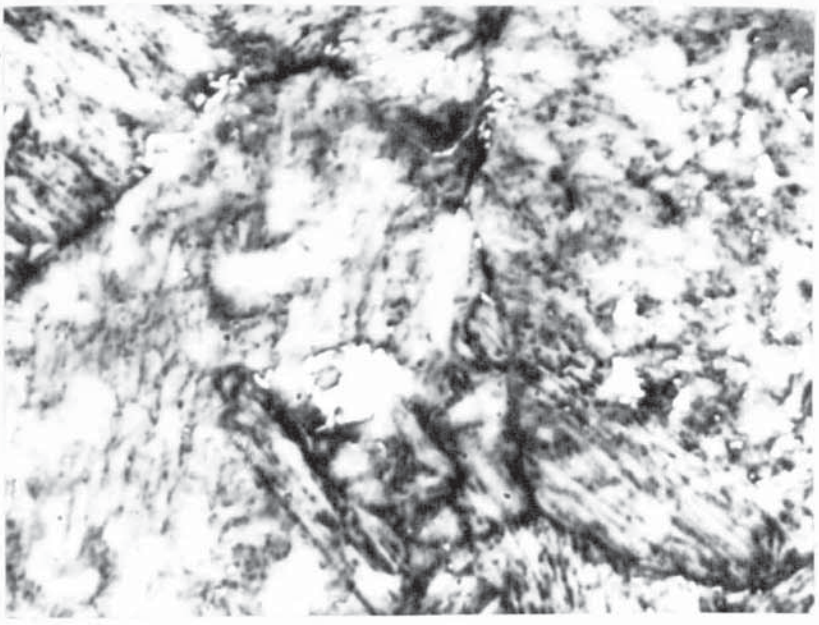

(b) Constitutional liquation of Ti_2S in the H.A.Z. x 1000.

Fig. 3.45. Submerged arc weld metal and H.A.Z. microstructures. Etchant 10% Nital.

showed no preference for the prior austenite grain boundaries, indicating embrittlement had not occurred.

Metallographic specimens were prepared from the as welded, unaged weld H.A.Z. in an attempt to determine if the white etching phase was retained or reverted austenite. The ribbon like regions were not detected, but some evidence of pools around inclusions was apparent by focusing and defocusing the microscope. This procedure also revealed a ghost grain boundary network close to the fusion boundary. However, the etching characteristics of the matrix were very similar to those of the pools and a distinct interface between the two was not clear. Consequently, although the morphology of the pools was present before ageing it was not possible to determine whether they were sufficiently enriched to be retained austenite. In contrast, the apparent absence of the ribbon like regions indicated that they only formed by reversion on ageing, although it was possible that the fine scale of these features prevented their detection in the unaged acicular matrix.

The fracture surfaces revelaed a transition corresponding to the different structures encountered by the fracture path, as shown in Fig. 3.46. The dimpled structure (a) relates to temperatures of about 1000°C. The presence of flatter "intergranular" fracture was apparent in the higher temperature areas, (b) and (c). Adjacent to the weld metal white etching phase, the fracture contained a mixture of ductile dimple sizes and was considerably undulating as shown in Fig. 3.46(d). The larger dimple size varied between 5μ and 10μ whilst the smaller dimple size was

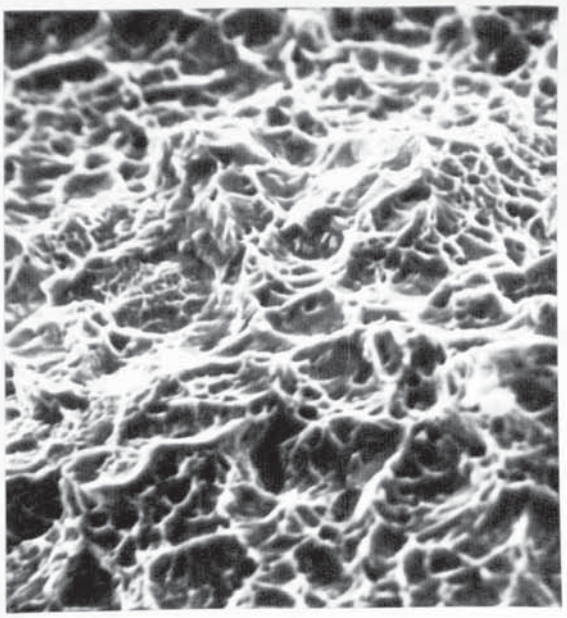

(a) General dimpled fracture 1000°C

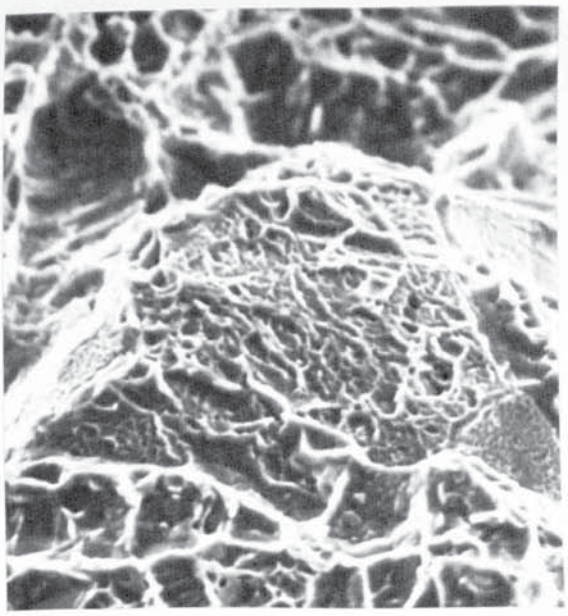

(b) Dimpled and flatter fracture 1200°C

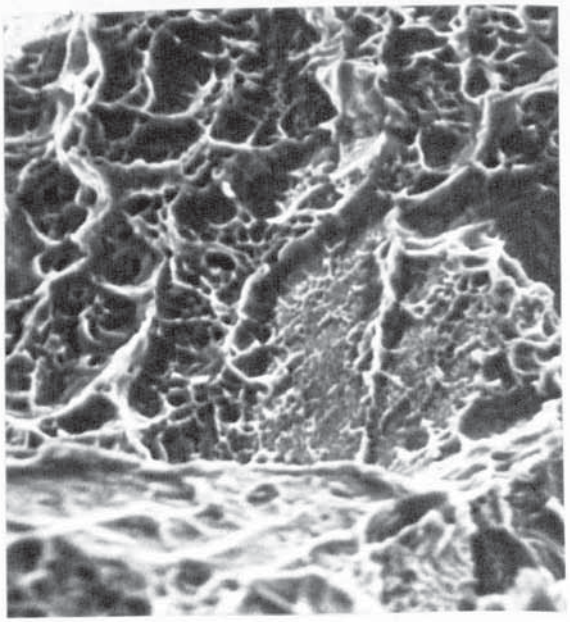

(c) Dimpled and flatter fracture 1300°C

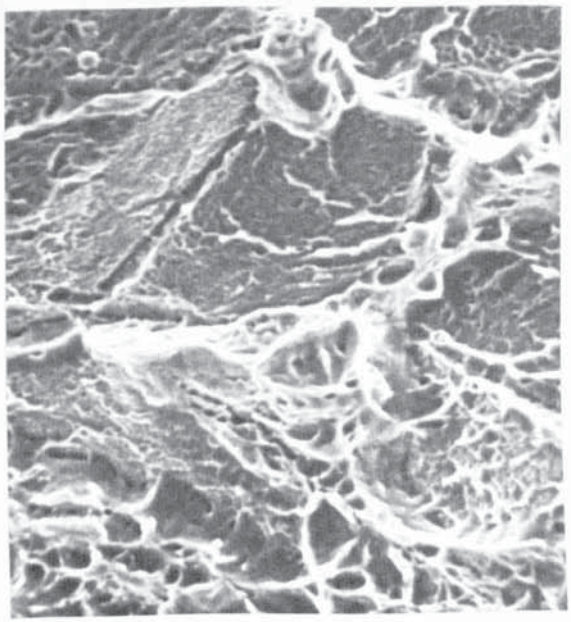

(d) Fracture adjacent to the fusion boundary. 1400°C+

Fig. 3.46. Scanning electron micrographs of fracture features from different peak temperature regions in the submerged arc weld H.A.Z. x 1500.

about 1μ. No evidence of hot cracking or grain boundary embrittlement was observed in any of the fractures.

Comparable results were obtained from the M.I.G. weld H.A.Z. The weld metal H.A.Z. interface is shown in Fig. 3.47(a) with the acicular matrix and prior austenite grain boundaries of the H.A.Z. clearly defined. The width of the H.A.Z. was less than the submerged arc weld H.A.Z., but a similar range of prior austenite grain size was detected. Constitutional liquation of the titanium sulphide inclusions and white etching ribbon like films were observed in the acicular structures, as shown in Fig. 3.47(b). As with the submerged arc weld, constitutional liquation of the titanium carbo-nitrides was only observed close to the fusion boundary.

Examples of the fracture surface are shown in Fig. 3.48. The dimpled structure (a) relates to a peak temperature of about 1000°C, with the dimple size being about 5μ. Increasing amounts of flatter fracture were observed over the temperature range from about 1200°C to 1300°C. These regions are shown in Figs 3.48(b) and (c) and in the latter case are directly associated with inclusions. Further evidence of the inclusions directly associated with the flatter "inter-granular" fracture was detected, as shown in Fig. 3.48(d). Finally, adjacent to the fusion boundary the fracture surface was considerably undulating. No evidence of hot cracking or grain boundary embrittlement was found in any of the fracture surfaces.

3.7.6 Intermediate structures

The microstructures and fracture surfaces related to thermal cycle peak temperatures of 600°C, 800°C and 1000°C

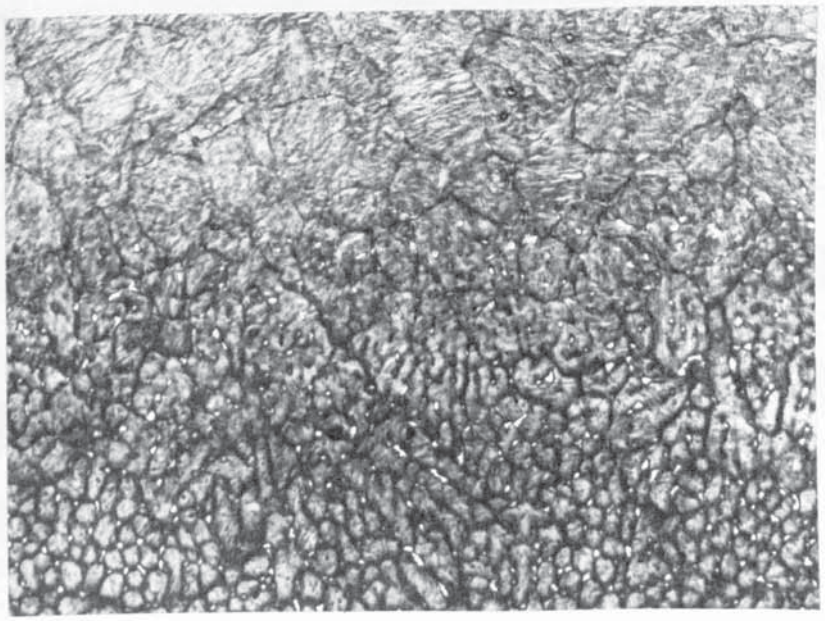

(a) General structure of the weld metal-H.A.Z. interface. x 150.

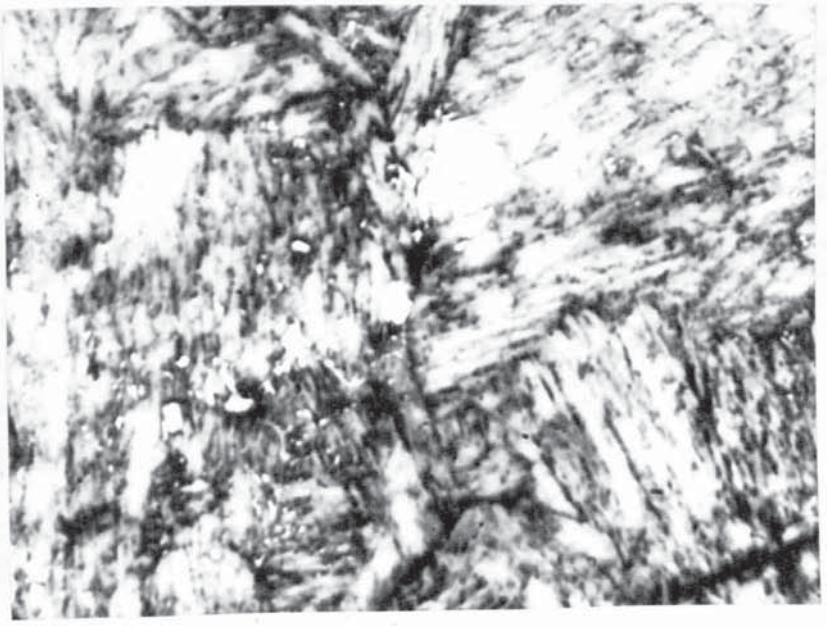

(b) Constitutional liquation of Ti_2S in the H.A.Z. x 1000

Fig. 3.47. M.I.G. weld metal and H.A.Z. microstructures. Etchant 10% Nital.

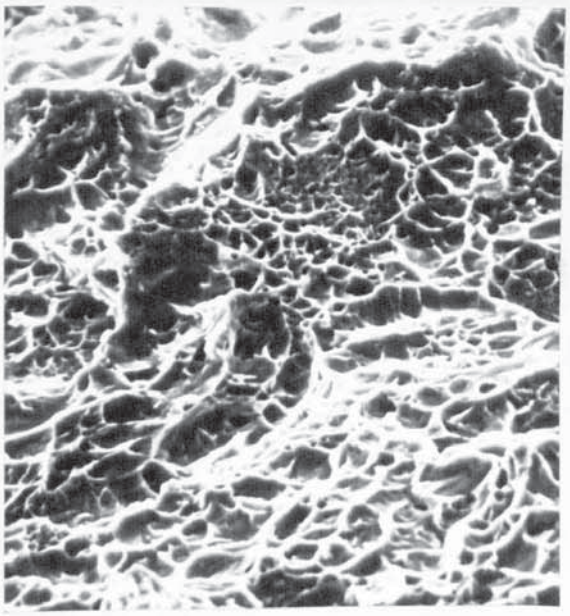

(a) General dimpled fracture 1000°C

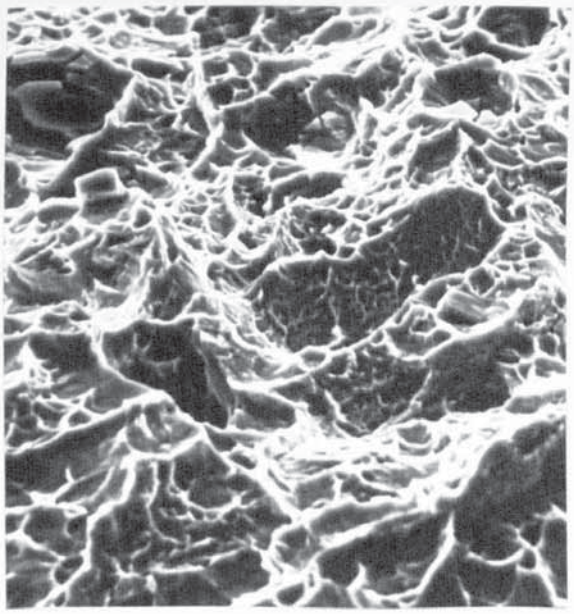

(b) Dimpled and flatter fracture 1200°C

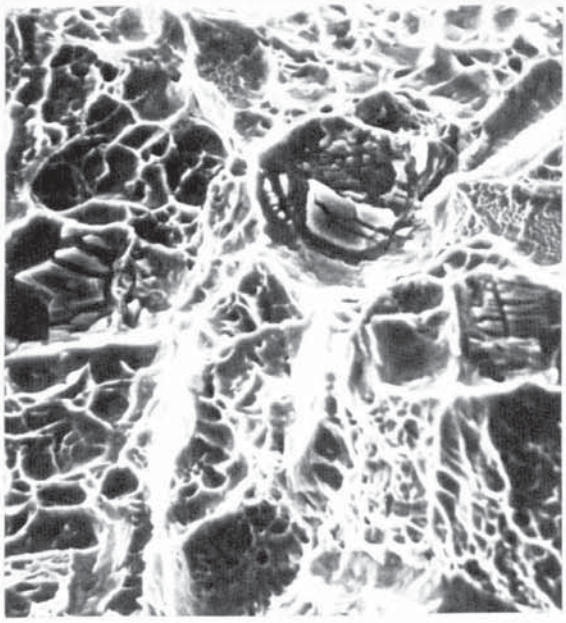

(c) Inclusions associated with flatter fracture. 1300°C

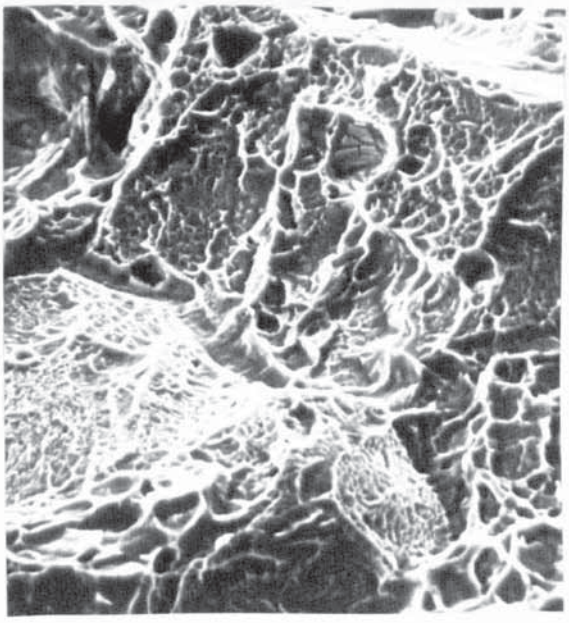

(d) Inclusions in flatter "intergranular" fracture. 1300°C+

Fig. 3.48. Scanning electron micrographs of fracture features from different peak temperature regions in the M.I.G. weld H.A.Z. x 1500.

were studied in detail in the simulated H.A.Z.s only. Over the range of welding parameters simulated the microstructures for any one peak temperature were relatively constant. Typical examples of these structures are shown in Fig. 3.49. Thermal cycles to 600°C produced no detectable changes from the as received material as can be seen in Fig. 3.49(a). At 800°C, Fig. 3.49(b), the structures were still relatively unaltered although they had experienced two phase changes. However, thermal cycles to 1000°C, Fig. 3.49(c), produced structures exhibiting a transition from a diffuse to an acicular appearance. The prior austenite grains were difficult to distinguish in these structures, and although they were becoming more apparent in the 1000°C structures, no grain size measurements were made. The globular white etching phase similar to that observed in the parent material was also present in these structures, but X-ray diffraction did not detect a second phase in any of the structures.

This range of structures was also observed in the real weld H.A.Z.s, but fracture toughness testing was confined to the simulated weld H.A.Z.s at these temperatures. The fracture surfaces from these structures exhibited a considerable consistency in appearance. Typical examples of this are shown in Fig. 3.50 for the three peak temperatures concerned. The entire fracture surfaces were dimpled and fracture occurred along a relatively flat plane. In all cases the dimple size was about 1μ.

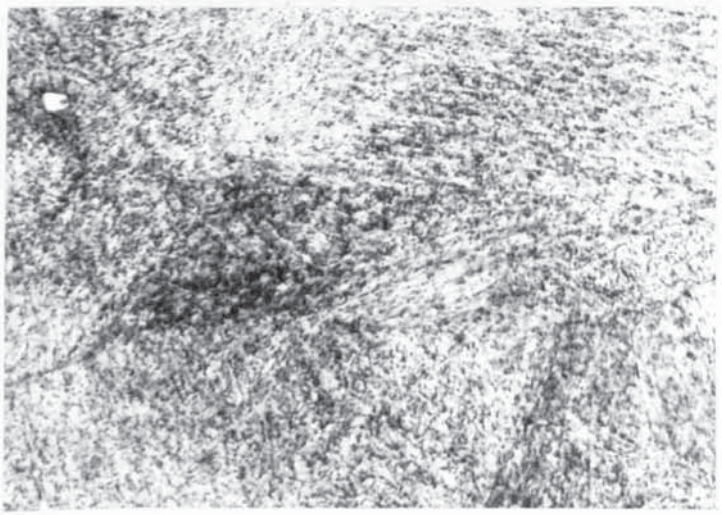

(a) 600°C

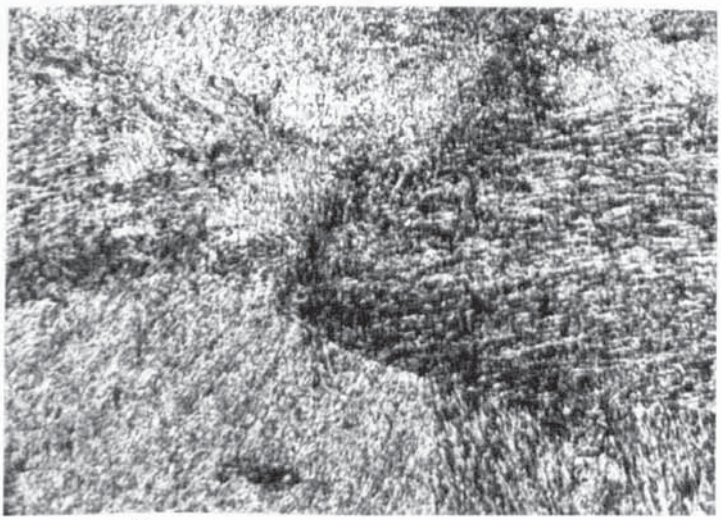

(b) 800°C

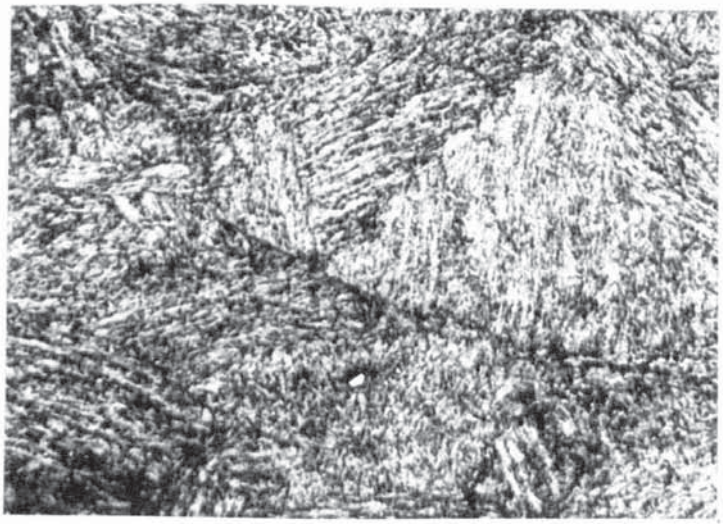

(c) 1000°C

Fig. 3.49. Simulated weld H.A.Z. microstructures for different thermal cycle peak temperatures. Etchant 10% Nital. x 500.

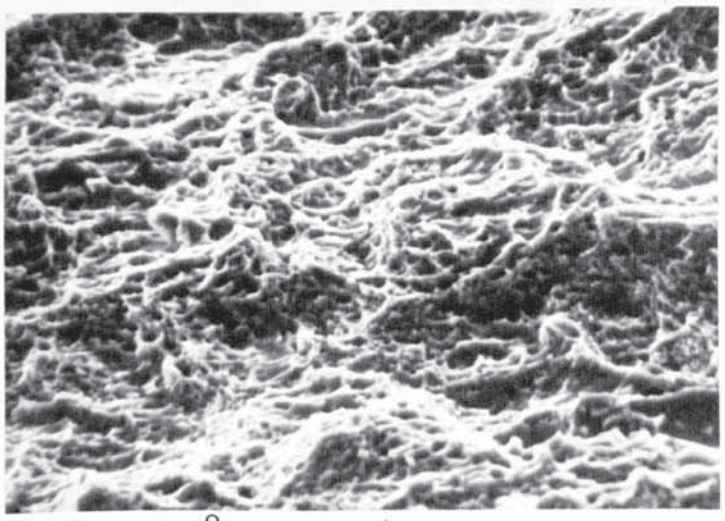

(a) 600°C

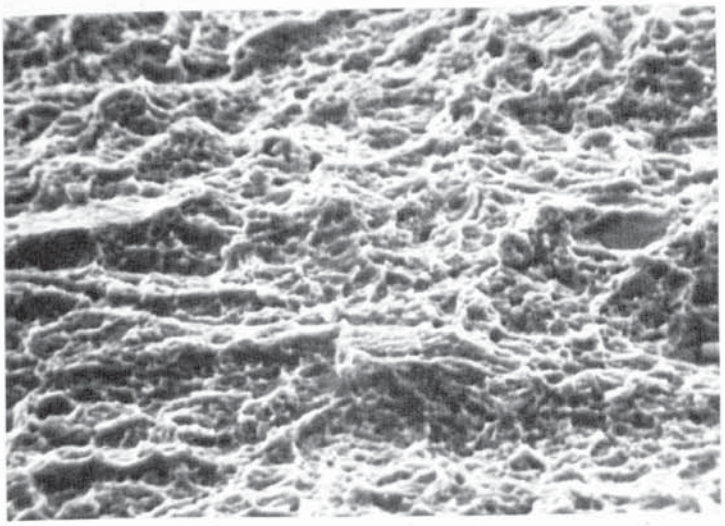

(b) 800°C

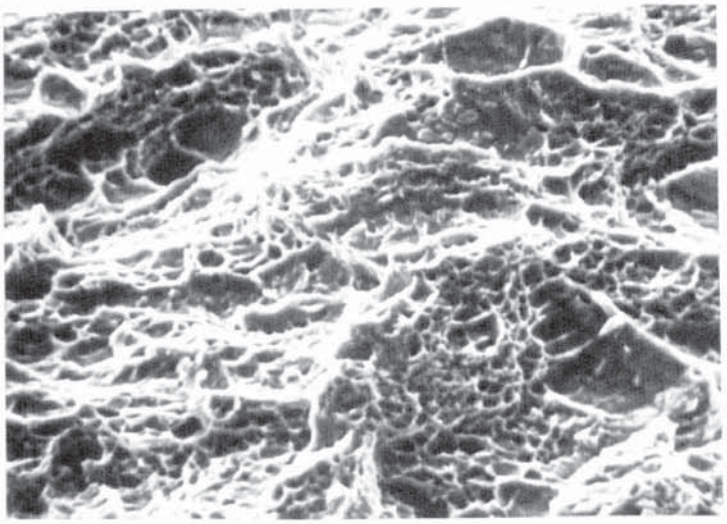

(c) 1000°C

Fig. 3.50. Scanning electron micrographs of the fractures in simulated weld H.A.Z.s for different peak temperatures. x 1500.

4. DISCUSSION

The main objective of this investigation was to determine the fracture toughness values and microstructures produced in real weld H.A.Z.s. The difficulties of testing in the real situation have already been discussed. It was because of these difficulties that the majority of the present work was carried out using a simulation technique. Nevertheless, before any detailed discussion of the results obtained by simulation can be considered, it is essential to show that the experimental techniques used accurately reproduced the real H.A.Z. situations.

4.1 Validity of Thermal Simulation

The thermal cycles for simulation were computed using Rosenthal's two dimensional heat flow equation and this represented the first deviation from the real weld H.A.Z. situation. Some of the reasons justifying this approach have already been presented in Section 2.4.3, and these were substantiated by results obtained in this investigation. Comparison of the real and computed H.A.Z. thermal cycles, given in Fig. 3.24 for the submerged arc weld in mild steel plate, indicated extremely good agreement for widely differing peak temperatures. Similar results were found for the H.A.Z. thermal cycles produced in maraging steel during submerged arc and M.I.G. welding as can be seen in Figs 3.25 and 3.27. The general trends of the real thermal cycles were followed by the computed thermal cycles in both cases. However, the real heating and cooling rates were faster and the differences between real and computed thermal cycles appeared to be greater for lower peak temperatures.

The agreement between real and computed thermal cycles is not as good for maraging steel as it is for mild steel and this is probably due to the different variations in thermal properties with temperature for the two materials. Since the heat flow equation assumes constant thermal properties, for mild steel, where K and α decrease with increasing temperature, the computed temperature at any instant will be low because K has not decreased and at the same time high because λ, $(\frac{1}{2\alpha})$, has not increased. If the net result is a balance this would account for the good agreement between real and computed thermal cycles. Extensive thermal property data are not available for maraging steel, but for alloy steels in general K increases with temperature whilst α increases or decreases depending on the alloy and temperature range considered. Consequently a balance is unlikely, which could account for the greater difference between real and computed thermal cycles in maraging steel. However, by covering a wide range of thermal cycles and having shown that the computed thermal cycles indicated the real trends, it is considered that the use of heat flow theory was justified.

The main basis on which thermal simulation can be considered valid however, must lie in a comparison of the fracture toughness and microstructure of the real and simulated H.A.Z.s. If the simulated H.A.Z. fracture toughness varied with heating and cooling rates the only results that could be used for direct comparison with the real H.A.Z.s would be those from the simulated H.A.Z.s involving the same heating and cooling rates as the real H.A.Z.s. However, the simulated H.A.Z. fracture toughness is

independent of heating and cooling rates and consequently the mean values of the simulated H.A.Z. fracture toughness can be used for comparison with either of the real weld H.A.Z.s.

The submerged arc and M.I.G. weld H.A.Z. fracture toughness results are given in Tables 3.14 and 3.16 respectively. The 650°C isotherms in the real weld H.A.Z.s are indicated by the dark etching bands in Figs 3.26 and 3.28. Since these are almost vertical through the plate thickness, the fracture toughness results from these positions can be considered to relate to this one peak temperature and should be directly comparable with the simulated H.A.Z. results. For peak temperatures of 650°C the simulated H.A.Z. mean fracture toughness, Fig. 3.21, is 67.8 ksi√in. which compares extremely well with the values of 67.5 ksi√in. and 66.9 ksi√in. for the submerged arc and M.I.G. weld H.A.Z.s respectively.

To compare the results at the other peak temperatures, it is necessary to remember that in the real weld H.A.Z.s the fracture toughness values relate to a range of peak temperatures. The submerged arc weld H.A.Z. results for the region 1000°C-1300°C have a mean value of 58 ksi√in. which agrees well with 57.8 ksi√in, the mean value obtained by combining the simulated results for thermal cycle peak temperatures of 1000°C-1325°C given in Table 3.11 and Fig. 3.22.

The mean fracture toughness values from the simulated H.A.Z.s involving peak temperatures of 1200°C-1400°C and 1000°C-1400°C can be compared with the real weld H.A.Z. results from the peak temperature regions of 1200°C-1460+°C for the submerged arc

weld and 1000°C-1460+°C for the M.I.G. weld. These are 63.6 ksi√in. and 60.6 ksi√in. for the simulated H.A.Z.s and 59.6 ksi√in. and 58.9 ksi√in. for the real weld H.A.Z.s. These results are also in agreement, but not as close as the previous comparisons. This may be due to grouping the simulated H.A.Z. results to contribute evenly to the mean values given above. In the real weld H.A.Z.s the temperature distributions covered by positions 3 in Fig. 3.26 and 2 in Fig. 3.28 would not give an even contribution from each temperature, and a larger proportion of the material will have experienced peak temperatures at the lower ends of the ranges covered. The exact proportions are difficult to evaluate, but if taken into account the effect would be to reduce the mean values quoted for the simulated H.A.Z.s. Also, the real weld H.A.Z. specimens contain some weld metal, which is generally expected to have a lower fracture toughness. If this were not present, the real weld H.A.Z. fracture toughness results would be increased. In view of this, it is considered that the real and simulated H.A.Z. fracture toughness results are in good agreement throughout.

The tensile properties also indicate that the simulated H.A.Z.s reproduced the real situation. In terms of σ_{LP}, the real H.A.Z. mean values, 115 tons/sq. in. and 116 tons/sq.in, for the peak temperature of 650°C are duplicated by the simulated H.A.Z. mean value of 115 tons/sq. in. As with the fracture toughness results, at higher peak temperatures direct comparisons are more difficult, but the simulated H.A.Z. results given in Tables 3.12 and 3.13 compare well with the submerged arc weld H.A.Z. results for peak temperatures

ranging from 1000°C to 1300°C given in Table 3.15. A general indication of the agreement between simulated and real H.A.Z. properties is also obtained from the hardness measurements presented in Figs 3.23, 3.29 and 3.30. In all cases the levels of hardness before and after ageing are about 340 Hv and 600 Hv respectively, except for the deviations that occur due to thermal cycling to peak temperatures around 650°C.

In comparing the microstructures, a similar close relationship is found to exist between the real and simulated H.A.Z.s. The formation of reverted austenite during thermal cycling to peak temperatures of 650°C was confirmed and analysed by X-ray diffraction in both cases. The volume fractions are given in Table 3.17 and the values for the submerged arc and M.I.G. weld H.A.Z.s, 18.2% and 22.5% respectively, fall within the range detected in the simulated H.A.Z.s. The morphology of the reverted austenite and the appearance of the fracture surfaces are consistent in the simulated H.A.Z.s, Figs 3.33 and 3.34, and the real H.A.Z.s, Figs 3.35 and 3.36, as well as being directly comparable with each other. This agreement shows that the strain cycles that will have been experienced in the real weld H.A.Z.s have not affected the structures or, as shown previously, the properties in this region.

At high thermal cycle peak temperatures once again good agreement between the real and simulated H.A.Z.s was found. In all cases well defined prior austenite grain boundaries were observed and the acicular matrix and undulating fracture paths were present throughout. Constitutional liquation was

common to both the real and simulated H.A.Z.s, as shown in Figs 3.40, 3.43 and 3.45, 3.47 respectively. As the thermal cycle peak temperature was increased in the simulated H.A.Z.s from 1200°C through 1325°C to 1400°C the amount of white etching ribbon like phase associated with constitutional liquation of titanium sulphide increased then decreased. Finally, at 1400°C constitutional liquation of titanium carbonitrides was observed. This corresponded to the real weld H.A.Z. high temperature structures where close to the fusion boundary the white etching ribbons were not apparent, but constitutional liquation of titanium carbonitrides had occurred.

If hot cracking and or grain boundary embrittlement had been encountered in the real weld H.A.Z.s, then the addition of strain to the simulated H.A.Z.s would have formed a necessary part of this investigation. However, constitutional liquation and the presence of strain in the real weld H.A.Z.s did not produce these problems and this is a significant factor in justifying thermal simulation alone in this alloy. It is realised that the real weld H.A.Z.s encountered in this investigation involved only slow to moderate heating and cooling rates and consequently high levels of strain may not have been produced. Nevertheless, work carried out at Bristol Aerojet Ltd[73,75] and recent discussions[115] revealed that even when high levels of strain were produced, with vacuum induction melted material of similar composition to that used in this investigation, hot cracking and or grain boundary embrittlement problems were not encountered. Consequently, it is considered that these H.A.Z. high

temperature structures can be accurately reproduced by thermal simulation alone.

The intermediate structures found in the real weld H.A.Z.s were also reproduced in the simulated H.A.Z.s. These structures related to peak temperatures of 600°C, 800°C and 1000°C, and although the latter two cases involved transformations, the presence of strain in the real weld H.A.Z.s did not appear to have had any effect. The general features were the same for both situations, differing little from the as received material, and confirming the agreement between real and simulated H.A.Z.s.

These comparisons between the fracture toughness, tensile properties and microstructures of the real and simulated H.A.Z.s indicate consistent agreement. Consequently it is considered that the thermal simulation approach to H.A.Z. studies in this alloy is fully justified.

4.2 The Fracture Toughness and Tensile Properties of the Weld H.A.Z.

The recommended practice for plane strain fracture toughness testing has been shown in Section 3.2.3 to predict an optimistic minimum thickness for valid K_{Ic} results from the parent material. However, the results from thermally cycled specimens, Tables 3.8 and 3.9, showed that the recommended practice was appropriate in the case of the fracture toughness and strength levels encountered in the weld H.A.Z. On the basis of the recommended practice, all the fracture toughness values to be discussed are valid as plane strain results.

Significant changes in fracture toughness and tensile properties were detected at various thermal cycle peak temperatures. In all such cases the fracture toughness was higher and the tensile strengths lower than the parent material values. The most substantial fracture toughness increases were found to correspond to thermal cycle peak temperatures of 650°C and 1400°C. These were 67.8 ksi$\sqrt{}$in. and 70.1 ksi$\sqrt{}$in. respectively as compared with the parent material value of 54.2 ksi$\sqrt{}$in. Fracture toughness values significantly higher than the parent material were also found for thermal cycle peak temperatures of 1200°C and 1325°C being 59.6 ksi$\sqrt{}$in. and 61.1 ksi$\sqrt{}$in. respectively.

The most striking feature of these results is that the fracture toughness is constant for any one thermal cycle peak temperature, and is independent of the heating and cooling rates. This is shown clearly by the H.A.Z. fracture toughness results given in Figs 3.21, 3.22 and Table 3.11.

At both high and low thermal cycle peak temperatures a wide range of heating and cooling rates have been covered, but for each peak temperature the fracture toughness is constant. For example, for thermal cycles to peak temperatures of 1200°C the heating rates range from 20°C per sec. to 600°C per sec. with corresponding cooling rates of 6°C per sec. and 88°C per sec. Even over such a range the fracture toughness remains constant about the mean value of 59.6 ksi√in.

For each case where the fracture toughness increases, the tensile strength decreases. This indicates a basic inverse relationship between toughness and strength and is found in most materials. As with the fracture toughness results, the tensile properties exhibit a dependence on the thermal cycle peak temperature and are independent of the heating and cooling rates.

The lowest mean values for the limits of proportionality were 115 tons per sq.in. and 118 tons per sq.in. which corresponded to the thermal cycle peak temperatures of 650°C and 1400°C respectively, where the highest fracture toughness values were detected. The remaining results were intermediate between these values and the parent material level of 129 tons per sq. in. In all cases the ultimate tensile strengths were between 6 and 9 tons per sq. in. greater than the limit of proportionality. The variation in tensile strengths was not reflected in the elongation and reduction of area results. For all H.A.Z. situations, except those corresponding to slow heating rates to peak temperatures of 1325°C and 1400°C, the elongations and reductions of area differed little from the parent material values of 9% and 44% respectively.

The dependence of fracture toughness and tensile properties on the H.A.Z. thermal cycle peak temperature was also reflected in the results where no significant changes were detected. This occurred for thermal cycles to peak temperatures of 600°C, 800°C and 1000°C. The fracture toughness and tensile properties, given in Tables 3.11 and 3.13 respectively, showed no dependence on heating and cooling rate and, except for the slightly lower tensile properties at 600°C, were very similar to the parent material properties.

Since the fracture toughness and tensile strengths are dependent only on the H.A.Z. thermal cycle peak temperatures, the relationship between properties and peak temperature can be presented graphically, as shown in Fig. 4.1. From such a plot, and a knowledge of the H.A.Z. peak temperature distribution in this material, the properties for any particular position can be predicted. The practical significance of this will be discussed in a later section.

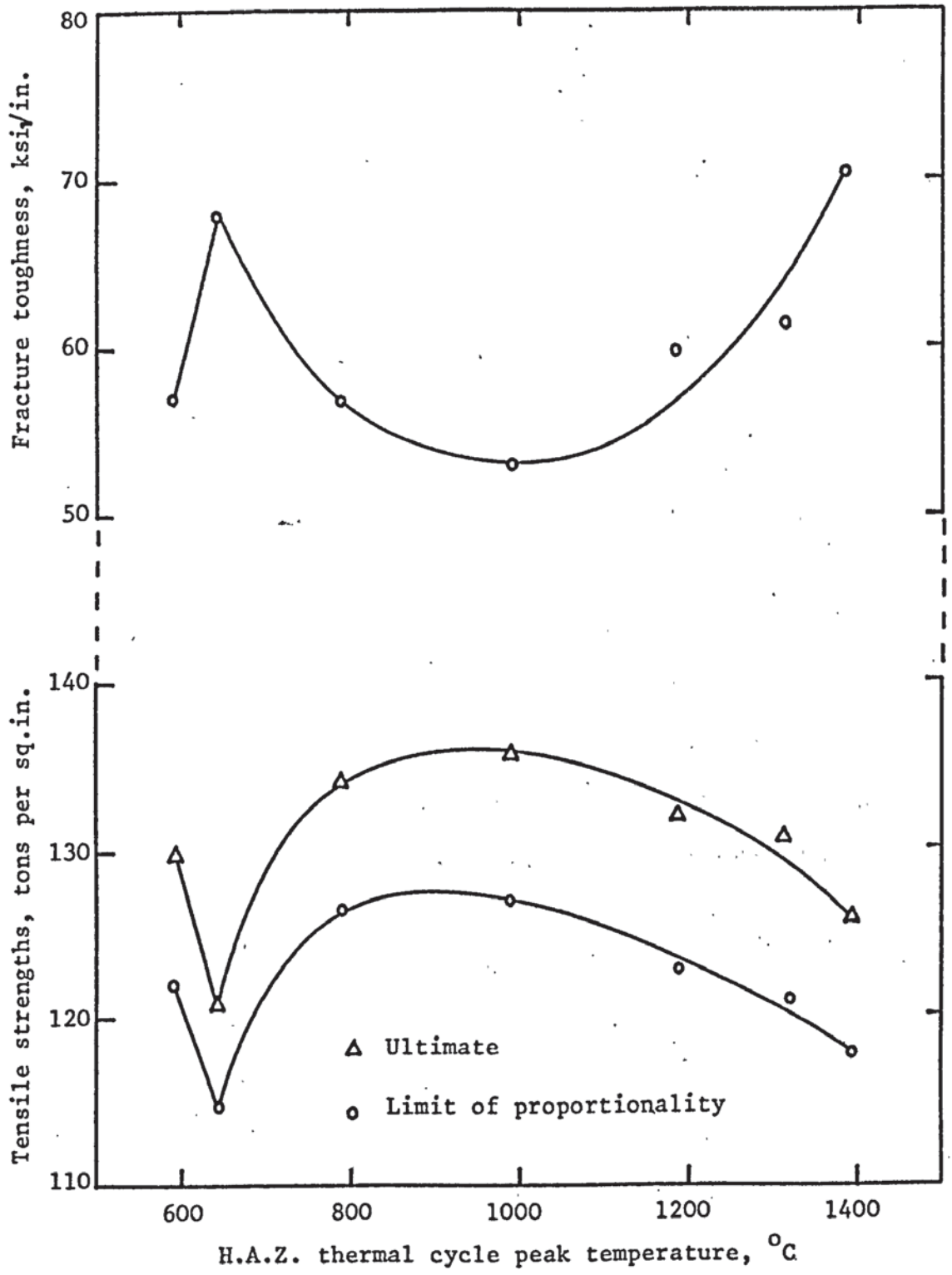

Fig. 4.1. The variation in fracture toughness and tensile strengths with H.A.Z. thermal cycle peak temperature.

4.3 Microstructures of the Weld H.A.Z.

The weld H.A.Z. microstructures in this material fall into three main groups as classified in Section 3.7. These relate to specific thermal cycle peak temperatures or temperature ranges, and can be conveniently discussed on this basis.

4.3.1 Reverted austenite structures

The presence of reverted austenite in maraging steels has been closely related to the material attaining a maximum temperature of 650°C and a mechanism of formation involving segregation and diffusion[82,84]. The results of this investigation show that H.A.Z. thermal cycles to peak temperatures of 650°C always result in the formation of a white etching phase. This has been identified as austenite which, since it formed on reheating to below the $\alpha \longrightarrow \gamma$ transformation temperature, is referred to as reverted austenite.

In all cases the reverted austenite occurred within the grains, giving rise to a mottled appearance, and in ribbons throughout the matrix, but did not produce a distinct two phase structure containing separate α and γ grains. The morphology of the reverted austenite was unaffected by the thermal cycle heating and cooling rates, as can be seen from Fig. 3.33 where the heating rate in (a) is 200°C per sec. compared with 7°C per sec. in (b). This is to be expected, since the only criterion for reversion is that the material becomes sufficiently enriched in alloying elements to revert and be metastable. Consequently, once enrichment and reversion have occurred, the heating and cooling rates should not affect the morphology of the phase formed.

The amount of reverted austenite formed would, however, be expected to depend on the heating and cooling rates. The volume fractions of reverted austenite have been determined for a number of H.A.Z.s, and are given in Table 3.17. These results show considerable scatter even for one welding process, as indicated by the two separate TIG 1 results of 11.8% and 29.8% reverted austenite. These variations may be due to inaccurate location of the notches which, subsequent to grinding away the fracture surfaces, would mean that X-ray diffraction was not carried out on the central region of the H.A.Z. However, the importance of these results is that they represent a statistically significant relationship between an increase in the volume fraction of reverted austenite and a decrease in the thermal cycle heating rate. This is consistent with the mechanism of formation of reverted austenite involving a diffusion controlled process. Consequently, thermal cycles involving slow heating rates will allow sufficient time at temperature for significant diffusion and reversion to occur, whereas at rapid heating rates the time at temperature and the amount of reversion will be reduced.

4.3.2 High temperature structures

The microstructures produced by H.A.Z. thermal cycles to high peak temperatures all contained an acicular matrix and well defined prior austenite grain boundaries. The acicular structures contained light and dark etching areas and the orientation varied from grain to grain and within the grains giving rise to domains. These reflected the different orientations produced when the austenite transformed

by shear to massive martensite on cooling. These structures have been shown to consist entirely of b.c.c. massive martensite[4] and although some evidence exists to indicate that the dark etching areas contain concentrations of alloying elements[84], the exact cause of the dark etching appearance has not been established.

The Widmanstatten structures produced by normal solution annealing, Fig. 3.1(a), are similar to the high temperature structures but less acicular. This could be analogous to the formation of feathery and acicular bainite in carbon steels, where faster cooling ratesproduce the more acicular structures. Consequently, since the weld H.A.Z. experiences more rapid cooling than the parent material undergoes after annealing, the weld H.A.Z. structures would be expected to appear more acicular.

The prior austenite grain size in the H.A.Z. indicates the nature of the thermal cycles experienced. In all cases, at any one peak temperature the grain size increased as the heating and cooling rates decreased. This is considered to be a direct result of slow thermal cycles involving longer times above the transformation temperature, where grain growth can occur, than fast thermal cycles. This factor together with the range of peak temperatures involved can be used to explain the observed variation in grain size. At peak temperatures of 1200°C thermal cycling resulted in grain refining even at the slowest heating rates. In this case the grain size was 30μ and the time at temperature was not sufficient for the newly formed austenite grains to grow to 50μ, the size produced at 1 hour at 820°C in the parent

material. At peak temperatures of 1325°C and 1400°C only the fastest thermal cycles produced a refined prior austenite grain size. The intermediate thermal cycles in each case resulted in a grain size of the same order as the as received material. However, the slowest thermal cycles involved sufficient time at temperature for the grains to grow to 56μ at 1325°C and 66μ at 1400°C, which in both cases was greater than the parent material grain size of 50μ.

Constitutional liquation was detected throughout the high temperature structures. In the 1200°C and 1325°C structures its occurrence was apparent in the form of the white etching ribbon like phase. In the 1200°C case, this was not directly related to either the titanium sulphide or titanium carbonitride inclusions previously identified in the parent material. However, in the 1325°C structures its association with the titanium sulphide inclusions was evident, as can be seen in Fig. 3.40(b). In view of this it is considered that the ribbons in the 1200°C structures are due to constitutional liquation or dissociation of inclusions, but the inclusions responsible have not been positively identified. Langstone[74] has shown that titanium carbides will liquate at temperatures below 1200°C, but these were not detected in the parent material in this investigation. However, Boniszewski[80] has reported that these inclusions are globular and white etching and it is possible that their presence within the reverted austenite in the parent material was missed. Consequently, it is considred that the constitutional liquation of titanium carbides could be responsible for the small amount of ribbon like phase observed in the 1200°C structures.

In the 1325°C structures the amount of ribbon like phase increased as the thermal cycle heating rate decreased. This is to be expected, since with slow H.A.Z. thermal cycles the structures will be above the critical temperature for constitutional liquation for longer periods of time than with fast thermal cycles. Consequently, providing the times involved were not sufficient to homogenise the alloy concentrations giving rise to liquation, a larger fraction of each inclusion would liquate giving an increase in the amount of ribbon like phase.

An important aspect of these structures is that there is no indication that the ribbon like phase is simply a film of the liquated titanium sulphide or carbide. In fact, most evidence points to the ribbons being either retained or, more probably, reverted austenite. This could arise if the sulphur and carbon, if present, diffused away from the liquated films, either further along the grain boundaries or into the matrix, leaving a titanium rich area. Although the electron probe microanalysis evidence is limited, it does indicate a titanium concentration in the ribbons. Consequently, this evidence in conjunction with the ductile nature of the ribbons is considered to indicate that this phase is austenite, and may have been formed by the mechanism described.

A further possibility exists since the ribbons of austenite may have formed by simple dissociation of the inclusions, in which case liquid films would not have formed. However, thermal cycles to 1325°C should, on the basis of published work[76], be sufficient to produce liquid films.

Also, the morphology of the phase and the extent to which it spreads unidirectionally indicates that it formed from liquid films that penetrated the prior austenite grain boundaries. Although the phase was not found at the prior austenite grain boundaries in the room temperature structures, this is consistent with the mechanism proposed by Pepe and Savage[76] whereby the prior austenite grain boundaries are unpinned and move on once the liquid films have solidified.

In the 1400°C structures there was little evidence of the austenite ribbons and only a few titanium sulphide inclusions were observed. These are considered to be the last indications of constitutional liquation of what were originally larger inclusions, since they were often associated with pools of austenite. The general absence of austenite ribbons can be explained by the high peak temperature of the thermal cycles having an homogenising effect on the alloy concentrations resulting from liquation. This is consistent with the proposal[75] and observation[76] that increased time at temperature can remove all evidence of constitutional liquation from the H.A.Z. structures in maraging steel. This appears to have been partially achieved for the titanium sulphide inclusions by simply increasing the temperature. However, the 1400°C structures also contained the first evidence of constitutional liquation of the titanium carbonitrides. The greater stability of these inclusions compared with the titanium sulphides and carbides has been reported previously[74]. Nevertheless, it is evident that the thermal conditions in the weld H.A.Z. are

sufficient to cause liquation even of these, the most stable maraging steel inclusions.

Well defined prior austenite grain boundaries were observed throughout the H.A.Z. high temperature structures. In other studies involving maraging steel[73-75] this has been related to titanium sulphide and carbide films and precipitates formed at the grain boundaries as the result of constitutional liquation and complete solution of the inclusions. In cases where the sulphur, carbon and consequent inclusion contents were high, as found generally in vacuum arc melted material, these grain boundary regions were severely embrittled and led to catastrophic failures. In other cases, where vacuum induction melted material low in inclusions was used, grain boundary embrittlement was not encountered. The results of this investigation have not led to the identification of any grain boundary films, and embrittlement has not been encountered in any of the structures. There is some evidence from the 1000°C and 1200°C structures to suggest that the prior austenite grain boundaries become more apparent even before appreciable constitutional liquation occurs. However, the main reason for the absence of grain boundary embrittlement would appear to be the low sulphur, carbon and inclusion contents of the vacuum induction melted parent material.

Finally, although H.A.Z. structures with thermal cycle peak temperatures greater than 1400°C were not simulated, they were observed in the real H.A.Z.s. Above this temperature and close to the weld metal, ghost grain boundaries were observed. These have been reported by Pepe and Savage[77]

and related to the alloy concentrations resulting from constitutional liquation. However, in this investigation they appear to be more directly related to the weld metal interdendritic austenite. This, as can be seen in Fig. 3.45(a), penetrates the H.A.Z. grain boundaries adjacent to the weld metal and would provide an adequate source of alloy concentration to produce the ghost grain boundaries.

4.3.3. Intermediate structures

The most significant feature about the structures produced by thermal cycling to peak temperatures of 600°C, 800°C and 1000°C is that they differed very little from the parent material structure. Also, as can be seen in Fig. 3.49, the structures are very similar to each other over this range of peak temperatures. As with the previous H.A.Z. regions, the heating and cooling rates had no apparent effect on the general appearance of the structures at any one peak temperature.

The structures produced by thermal cycling to 600°C might have been expected to contain some reverted austenite, but apart from globular areas as observed in the parent material after ageing, none was detected by either metallographic or X-ray diffraction techniques. This finding is also reflected in the hardness results presented in Fig. 3.23. These clearly indicate that a peak temperature of 600°C is sufficient to produce considerable ageing in the solution annealed material during the relatively short time involved in thermal cycling. However, subsequent to ageing, the hardness level was further increased to the normal aged level of 600 Hv, and softening due to the presence of reverted austenite was not encountered.

The structures produced by thermal cycling to peak temperatures of 800°C and 1000°C have all been subjected to the $\alpha \rightleftharpoons \gamma$ transformation. In quenched and tempered carbon and low alloy steels the effects of heating rate and particularly cooling rate are considerable on similar transformations and their transformation products. However, the consistent appearance of the structures observed in this investigation indicate that the $\alpha \rightleftharpoons \gamma$ transformation is insensitive to the heating and cooling rates experienced. This is in agreement with the expected behaviour of maraging steel[9], and consequently, over the peak temperature range from 800°C to 1000°C maraging steel weld H.A.Z.s would be expected to exhibit a consistent microstructure.

The transition from these intermediate structures to the high temperature structures can be seen in the H.A.Z. produced by thermal cycles to 1000°C. These structures begin to take on a more acicular lighter etching appearance and the prior austenite grain size becomes more apparent as can be seen in Fig. 3.49(c). Even so, at 1000°C the structures are more similar to the parent material than the H.A.Z. high temperature structures.

4.4 Correlation of Fracture Toughness and Microstructure

The H.A.Z. fracture thoughness results obtained in this investigation fall into two main groups; those that have increased significantly above the parent material value and those that are relatively unaffected. The microstructures of the H.A.Z. also fall into two broad groups of similar identity; those structures that have altered and those that have not. To obtain a quantitative correlation it is necessary to relate definite features of the microstructures or fractures directly or indirectly to the properties.

4.4.1 Quantitative correlation

The models of Krafft[53,54] and Wells[57] attempt this through the process zone size d_T and the crack opening displacement ($2V_c$) respectively. These factors have been evaluated from the fracture toughness and tensile data given in the results. The values of Young's Modulus, 30×10^6 psi, and strain hardening exponent 0.013, used in this evaluation have been taken from data published on a 275 grade of maraging steel[116], and are assumed to be constant throughout. The metallographic and fractographic features measured in the H.A.Z. structures were the grain size and dimple dimensions. These are presented for correlation in Table 4.1 together with the corresponding values of d_T, ($2V_c$) and mean fracture toughness.

The generation of microvoids occurs ahead of the crack tip, usually at structural discontinuities. Consequently, d_T should be related to features that occur regularly thoughout the structure or fracture surface. Selecting grain size for comparison, it is apparent from Table 4.1

Thermal cycle peak temperature °C	Fracture Toughness ksi√in.	Process zone size d_T		C.O.D. ($2V_c$) μ	Grain size μ	Dimple size	
		Model 1 μ	Model 2 μ			Length μ	Width μ
Parent	54.2	78	19	4	50	1,5-10	5
600	56.7	86	23	5	50	1	5
650	67.8	123	36	8	50	1,5-10	5
800	56.7	86	21	5	-	1	5
1000	52.8	74	18	4	-	1	5
1200	59.6	95	25	6	15-30	1,5-10	5
1325	61.1	100	26	6	27-56	1,5-10	5
1400	70.1	131	36	8	35-66	1,5-10	10

Table 4.1. The fracture toughness and microstructural features of the H.A.Z. and the corresponding process zone size and crack opening displacement based on existing models.

that d_T evaluated from Krafft's original model does not relate in any way to grain size. Considering the parent material, 600°C and 650°C structures, d_T varies from 75μ to 123μ whilst the grain size is constant at 50μ. This model has been altered to take account of the triaxial stresses at the tip of a crack, and this gives much smaller values of d_T. However, as before these vary from 19μ to 36μ for the same structures with a grain size of 50μ.

For the high temperature structures, the d_T values are of the same order of magnitude as the prior austenite grain size. However, since the grain size varies with heating rate at any one peak temperature whilst the fracture toughness and consequent d_T values are constant, these factors cannot be considered to correlate. In terms of dimple length, the most significant feature about the values obtained from the fracture surfaces is that they vary little throughout the structures studied. Consequently, since d_T varies from 18μ to 36μ throughout the structures examined, it is considered that the Krafft model is not applicable to these features.

A possible objection to the basis of this attempted correlation might arise from the use of a constant value of the strain hardening exponent n, in evaluating d_T. If n varies then it will affect the values of d_T. In order to determine n for each H.A.Z. peak temperature, it would be necessary to carry out precise tensile tests utilising an extensometer to arrive at a logarithmic plot of true stress against true strain and hence from the slope, n. This was not practicable with the specimens used in this investigation.

However, since the strain hardening exponent relates to the plastic region of the stress-strain curve, an estimate of how it varies can be obtained from the difference between the limit of proportionality and tensile strengths, and the elongation and reduction of area values. It has already been shown that these factors are relatively constant throughout apart from some of the high temperature structures' elongation and reduction of area values. Consequently, it is considered that any variation in the strain hardening exponent would be small and not sufficient to produce a correlation between process zone size and structural features.

The crack opening displacement values calculated from the model of Wells should be compared with the width of the dimples measured in the microsections for the purpose of correlation. The width of the dimples given in Table 4.1 represent the maximum crack surface displacement and reasonable correlation exists between these values and $(2V_c)$. However, the two most significant fracture toughness increases are found at peak temperatures of 650°C and 1400°C, and in both these cases correlation is not good. Also, this model does not enable fracture toughness to be related to definite microstructural features, but only to the fracture itself. Since there appears to be no quantitative relationship between fracture toughness and microstructure on the basis of existing models, and the results given in Table 4.1 indicate no other quantitative relationship, the findings of this investigation must be assessed on a more qualitative basis.

4.4.2 Qualitative correlation

The fracture toughness results relate directly to the three groups of structures previously described. The structures containing reverted austenite correspond to an increased mean fracture toughness of 67.8 ksi√in. The reverted austenite phase is uniformly dispersed throughout the structures and does not appear to affect the fracture path itself. However its formation depends on the segregation of alloying elements, in particular nickel and titanium, that form a major part of the strengthening precipitates[9, 18-21]. Consequently, on ageing maximum strengthening is not obtained in these structures, as shown by the mean limit of proportionality 115 tons/sq.in. As the strength decreases the toughness will increase in accordance with the general inverse relationship between these properties, and it is considered that this accounts for the increased fracture toughness detected in these structures.

The results given in Table 3.17 have already been shown to indicate a significant relationship between the volume fraction of reverted austenite and heating rate. Also, it is found that a relationship exists between the volume fraction of reverted austenite and fracture toughness. This may be taken to indicate that a relationship exists between heating rate and fracture toughness through the volume fraction of austenite. However, the results presented in Fig. 3.21 show that for the range of heating rates studied no relationship exists. Consequently, it is considered that even the fastest heating rates give rise to sufficient reverted austenite to produce a significant increase in

fracture toughness. Thereafter, decreasing the heating rate will produce more reverted austenite, but with a less significant effect on toughness.

A more direct, but still qualitative, correlation exists between the fracture toughness and high temperature microstructures. In both the 1200°C and 1325°C peak temperature structures, fracture occurred by ductile dimple formation as can be seen in Fig. 3.37(b) and 3.39(b). Dimple formation was not so evident in the 1400°C peak temperature structures, but was revealed in the fracture surfaces, Fig. 3.44(a). However, in all cases the fracture path was more undulating than in the as received material, Fig. 3.31(b). Any deviation in the fracture path from its mean line will involve a greater consumption of energy as the fracture advances than would occur if the fracture remained along the mean line. It is considered that this deviation of the fracture path accounts for the increased fracture toughness of these structures.

A number of metallographic features appear to contribute towards the fracture path deviation. All the high temperature structures contain the ribbon like reverted austenite phase as a result of constitutional liquation. This is shown in Fig. 3.40 and, as can be seen in (a), the fracture path can be deviated along this phase. These regions of the fracture take on an intergranular appearance, Figs 3.38(a) and 3.41(c), even though metallographically they appear within the matrix. However, this appearance is consistent with the phase having been a liquid film at the prior austenite grain boundaries which subsequently moved on when the film solidified.

The dimple size in these reverted austenite areas was 1μ and compared directly with the dimples in the 650°C structures. Hence, since the fracture toughness of structures containing large proportions of reverted austenite has been shown to increase, the ribbons of reverted austenite could also be expected to have an increased fracture toughness. Consequently, the presence of reverted austenite in the high temperature structures could contribute to the observed increases in fracture toughness both by deviating the fracture path as well as representing areas of locally increased fracture toughness.

Some small deviations also occurred in the fracture paths at the prior austenite grain boundaries, although in general there was no preference for these regions. Nevertheless, the fracture advances by ductile dimple formation even along the grain boundaries, as can be seen in Fig. 3.37(b). Consequently, since there is no evidence to suggest that the grain boundaries are embrittled or provide an easy path for fracture, deviation of the fracture path by the prior austenite grain boundaries may also contribute to the observed increase in fracture toughness.

The most significant factor however appears to be the acicular nature of the matrix itself. The majority of the fracture path deviations occurred within the matrix at positions related to changes in the orientation of the structure. This was particularly noticeable in the H.A.Z. structures that had experienced thermal cycle peak temperatures of 1400°C, as can be seen in Fig. 3.42(b). In this

case the fracture path crosses a number of different acicular orientations and two grain boundaries without any significant deviation in the fracture path. However, in the central region where the acicular matrix is at right angles to the fracture path, it is deviated through 90°. Similar deviations in the fracture path and the acicular appearance of these structures are also apparent in the fracture surfaces shown in Fig. 3.44(c) and (d).

These observations indicate that it is relatively easier for void formation and fracture propagation to occur parallel to the direction of the acicular structure than it is transverse to the acicular structure. However, since this relatively easier path for fracture involves considerable deviation the net result is an increase in fracture toughness. Similar observations have been made by Salmon Cox et al[84], although in this case banded and not acicular structures were responsible for deviating the fracture path and increasing the toughness.

The exact reason for the effect the acicular matrix has on the fracture path is not evident from this investigation. Also, it is not clear why the fracture toughness should increase from about 60 ksi√in. for the 1200°C and 1325°C structures to 70 ksi√in. for the 1400°C structures. It is possible that the larger grain size in the 1400°C structures resulted in larger domains, and consequently increased both the fracture path deviation and toughness. However, if this were the case it would be expected that the fracture toughness would increase as the grain size increased, irrespective of the peak temperature. This was not observed,

and in all cases the fracture toughness was independent of the grain size for any one peak temperature. Nevertheless, it is considered that deviation of the fracture path due to the formation of these acicular structures is the main factor causing the increase in fracture toughness.

One further general contribution to the overall increase in fracture toughness of these structures could be the observed decrease in their strength, as given in Table 3.13. In the case of the 650°C structures, the decrease in tensile strength was accounted for in terms of less precipitation hardening. Since the dark etching areas of some acicular structures have been shown to contain higher alloy contents, this might also arise in the high temperature structures and so affect the strength after ageing. No evidence to confirm this has been obtained in this investigation but, nevertheless, as the strength decreases the fracture toughness would be expected to rise.

The results given in Table 3.13 also reveal that the elongation and reduction of area values for the intermediate and slow heating rates to peak temperatures of 1325°C and 1400°C are less than the levels generally obtained in this investigation. This may be partly a result of the inverse relationship between grain size and the strain for fracture[41], as shown in Fig. 2.15, but is considered to be more directly related to the effects of constitutional liquation. During tensile testing it is possible that deformation was confined to regions of the ribbon like reverted austenite. If this were the case, the elongation and reduction of area properties for the 1325°C structures could be a reflection of the

content and nature of this phase. The fastest heating rate produced the least austenite and it would appear that this was insuffient to affect the properties. For the remaining structures, these properties are considerably reduced, with a minimum level at the intermediate heating rate. The amounts of reverted austenite were similar in both cases, but with increased time at the slowest heating rate the ribbons may have become more diffuse and consequently more ductile than those present in the intermediate heating rate structures. Although the metallography and fractography of these structures has not revealed any distinct difference between the ribbons, the above mechanism would explain the observed elongation and reduction of area properties.

The ribbon like reverted austenite phase was almost completely absent from the 1400°C structures. As a result the tensile properties, Table 3.13, were much less affected. The reduction of area properties were reduced in both the slow and intermediate heating rate structures and, although constitutional liquation may have had some effect, this could be simply the effect of large grain size.

The structures produced at H.A.Z. positions relating to peak temperatures of 600°C, 800°C and 1000°C were very similar to the aged parent plate microstructures. This similarity was also apparent in their fracture toughness values given in Table 3.11. In all cases the fracture surfaces contained ductile dimples that differed very little throughout this range of peak temperatures, as can be seen in Fig. 3.50.

Also, fracture took place along a relatively flat plane and there appeared to be no relationship between the

fracture path and the microstructure. However, these results do serve to indicate that providing the microstructure is unaffected by the thermal cycles experienced in a weld H.A.Z., the fracture toughness should also be unaffected.

The tensile properties of the majority of these structures were also consistent with those of the parent material, as can be seen in Table 3.13. Some variations are apparent in the structures produced by thermal cycling to peak temperatures of 600°C. In this case the limit of proportionality and tensile strengths are 122 tons/sq.in. and 130 tons/sq.in. respectively, slightly less than the parent material values. This is considered to be due to the effect of some reverted austenite, although its presence was not apparent from X-ray diffraction, metallographic or fracture toughness results.

4.5 Practical Significance of the Results

A number of factors of practical significance are evident from the results of this investigation. These fall into two main groups: those that apply specifically to this material and those of more general applicability. These factors will now be discussed.

The results of this investigation represent a detailed description of the weld H.A.Z. in terms of its fracture toughness and tensile properties. This data, as shown in Fig. 4.1, gives a good indication of the fracture resistance to be expected at different positions in the H.A.Z. However, its full practical significance can only be realised when it is used to predict the defect size that a particular zone can tolerate. It has been shown that this critical defect size depends not only on the fracture toughness of the material, but also the stress normal to the defect and the dimensions and type of defect[37]. For an embedded flaw the relationship is given by equation 2.13 as

$$a_{cr} = \frac{Q_{cr}}{\pi}\left[\frac{K_{Ic}}{\sigma}\right]^2$$

To demonstrate the variation in critical defect size across the weld H.A.Z. it is necessary to assume precise values for a number of the above parameters. The flaw shape parameter Q depends on the defect ratio a/2C and the ratio σ/σ_{ys}, as shown in Fig. 2.14. The value of a/2C can be assumed constant throughout, and σ_{ys} will depend on the H.A.Z. position. However, σ is less readily defined.

It is normal practice in the aerospace industry to design to operate at 75% of the ultimate tensile stress or 85% of the yield stress, whichever is the lower, and proof pressure test at 110% of this operating stress[115]. Since these values are based on the parent material properties, this procedure will result in a maximum applied stress of 108 tons/sq.in. arising during proof testing. On this basis σ/σ_{ys} will vary across the weld H.A.Z. and with a/2C constant, Q will also vary. However, it has been suggested that local residual stresses in the weld H.A.Z. can contribute to the operating stress to produce local stresses equal to the yield point of the material[39]. Using this as the criterion σ/σ_{ys} will be unity across the H.A.Z. and assuming a/2C constant, Q will be constant.

The critical defect size for an embedded flaw in the weld H.A.Z. of this material has been calculated from the data in Fig. 4.1 assuming a/2C constant and corresponding to a Q value of 1.5. These values are presented in Fig. 4.2 plotted against the H.A.Z. thermal cycle peak temperature. As would be expected, this is similar in appearance to Fig. 4.1, but more directly applicable to the practical situation. It is apparent from this plot that the 650°C and 1400°C regions of the H.A.Z. can tolerate defects up to twice the size of those that would be critical in the parent material or intermediate structures. Consequently, defects could grow to a critical size in one region of the H.A.Z. and become subcritical on propagating into another, tougher region. The converse may also occur, and subcritical defects growing in the tougher zones may become critical on reaching the less tough zones.

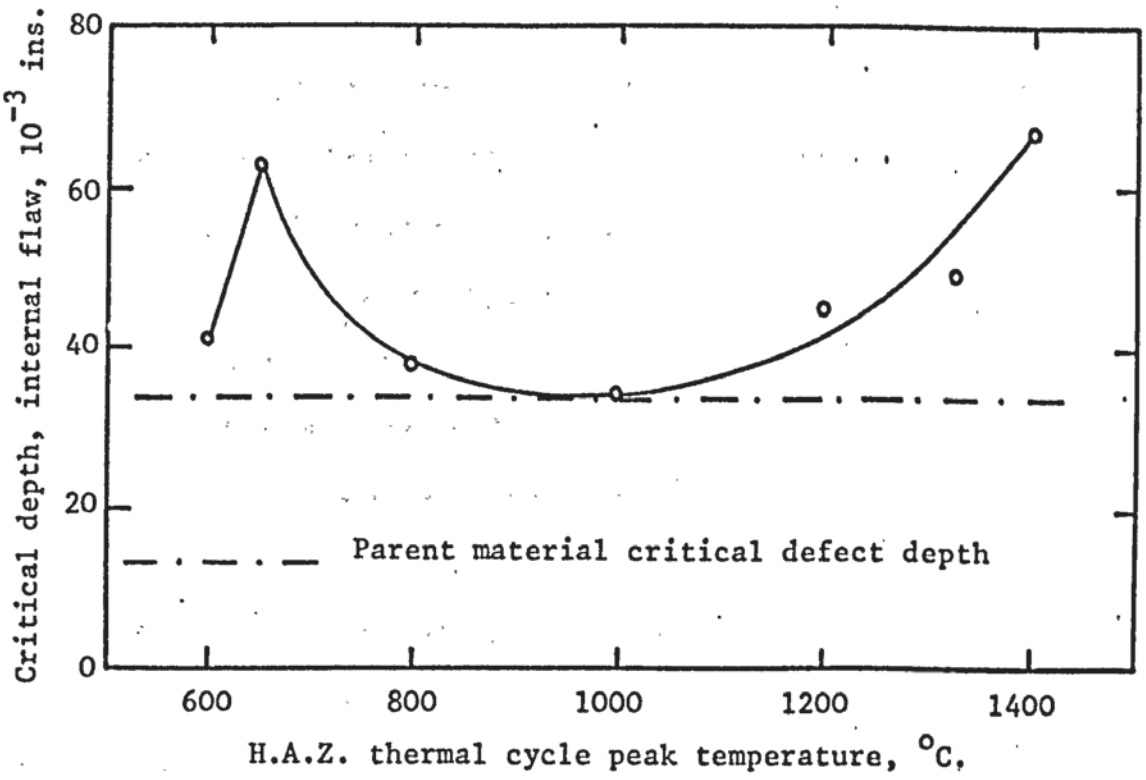

Fig. 4.2. The variation in the critical depth of an internal flaw with H.A.Z. thermal cycle peak temperature.

Even if the tougher regions of a H.A.Z. are unable to arrest a crack, they may provide sufficient resistance to deviate its path into a less tough region and in so doing cause it to be arrested as a result of the reduction in normal stress across the crack. This sort of behaviour has been observed recently in a practical situation involving the proof testing of a rocket motor casing[115]. The casing was manufactured from a vacuum induction melted 300 grade maraging steel of similar composition to that used in this investigation. After proof testing, transverse cracking in the weld H.A.Z. was observed, but this had been deflected parallel to the weld by both the reverted austenite and acicular structures. In deflecting the cracks the stresses acting across them were reduced and the cracks arrested. The origin of this cracking was considered to be hydrogen embrittlement, and eliminating the source of hydrogen has removed the H.A.Z. cracking problems[115]. Nevertheless, the interaction between the reverted austenite and acicular structures and the propagating cracks appears to be in agreement with that expected from the results of this investigation.

The critical defect size data given in Fig. 4.2 also represents a basis for selective non-destructive testing (N.D.T.). At present, 100% radiography is carried out on most aerospace components and any defect detected is considered intolerable. However, a more realistic approach would be to utilise N.D.T. to pass or reject a component on the basis of the experimentally determined critical defect size for that structure. At present there exists a limit

to the minimum size of defect that can be found using N.D.T., and the critical defect size for many high strength steels is below this limit. However, as advances are made in N.D.T., detailed information such as the variation in critical defect size across a weld H.A.Z. will become a necessity.

This factor indicates the significance of utilising a simulation technique for H.A.Z. studies. It has already been shown that in lower peak temperature regions, the real weld H.A.Z. can be tested with some accuracy. However, at higher peak temperatures testing in the real weld H.A.Z. is not sufficiently selective to differentiate between the considerable property changes that can occur over small distances in these regions. Consequently, it is considered that the simulation approach to H.A.Z. studies should be adapted more generally, with the proviso that it is established as valid and reproduces the real situation.

Since a wide range of maraging steels exist, having various combinations of fracture toughness and strength, it is necessary to consider if the findings of this investigation can be applied in general. The significant changes in microstructure and fracture toughness observed in this investigation related to thermal cycle peak temperatures of 650°C and 1200°C-1400°C. At 650°C the formation of reverted austenite produced a mean fracture toughness of 67.8 ksi$\sqrt{in}$., considerably higher than the parent material value of 54.2 ksi$\sqrt{in}$. The material used in this investigation was a 300 grade maraging steel, having one of the highest strengths and corresponding lowest toughness of the commercial grades available. Hence, the 25% increase in fracture toughness

and 11% decrease in tensile strength produced by the formation of reverted austenite in this material might be partly a reflection of the original levels of these properties. Similar significant changes might not be encountered in the lower strength, higher toughness 200 and 250 grades of maraging steel. Nevertheless, since the formation of reverted austenite is mainly temperature dependent, the presence of this phase and its general effects on properties would be expected to be found at the 650°C isotherm in the weld H.A.Z. of any grade of maraging steel.

The increased fracture toughness obtained in the H.A.Z. at peak temperatures of 1200°C-1400°C has been related to the formation of acicular massive martensite structures and their effect on the fracture path. An important feature of these structures was that they were contained within prior austenite grain boundaries that were not embrittled even though constitutional liquation of the inclusions had occurred. If grain boundary embrittlement had been encountered, then the fracture path would have been intergranular and the beneficial effect on toughness of the acicular matrix would not have been experienced. There would appear to be no reason why acicular structures should not be formed in the high temperature region of any maraging steel weld, and indeed such structures are generally observed. Consequently, if high purity vacuum induction melted material is used to avoid the formation of brittle grain boundary films, the acicular structures should represent a region of increased fracture toughness in any maraging steel weld H.A.Z.

Finally, the results of this investigation indicate that the fracture toughness of maraging steel is not impaired by the effects of thermal cycles in the weld H.A.Z. However, since these materials are often used at working stresses approaching the yield stress, it is important to realise that significant decreases can occur in this property in the H.A.Z. This was particularly noticeable in the reverted austenite region where, as can be seen in Table 3.12, with very slow heating and cooling rates the yield strength of the H.A.Z. was reduced by 20% to 104 tons/sq. in. This case represents the greatest change encountered, and by avoiding the very slow thermal cycles these drastic reductions in strength can be overcome. Nevertheless, it must be realised that although the fracture toughness of a particular region is increased, the locally reduced strength in this region might result in unexpected problems of plastic deformation and distortion.

5. CONCLUSIONS

The conclusions of this investigation fall into two main groups. Firstly, a number of conclusions relate specifically to vacuum induction melted 300 grade maraging steel.

1. The fracture toughness and microstructure produced by thermal simulation alone in this alloy correlate with those produced in real weld H.A.Z.s.
2. The H.A.Z. fracture toughness increased significantly in certain regions, with mean values of 67.8 ksi$\sqrt{in.}$ and 59.6 to 70.1 ksi$\sqrt{in.}$ being measured as compared with the parent material fracture toughness of 54.2 ksi$\sqrt{in.}$
3. The fracture toughness of the weld H.A.Z. is a function of peak temperature only, with the regions of increased fracture toughness found to correspond to peak temperatures of 650°C and 1200°C-1400°C.
4. The increase in H.A.Z. fracture toughness produced by thermal cycling to a peak temperature of 650°C is related to the formation of reverted austenite.
5. Acicular structures produced by thermal cycling to peak temperatures of 1200-1400°C account for the increases in fracture toughness in this region of the H.A.Z.
6. Thermal cycles to peak temperatures of 1200-1400°C produce constitutional liquation in the H.A.Z., but low carbon, sulphur and consequent inclusion contents ensure grain boundary embrittlement is not a problem.

Secondly, this investigation presents certain conclusions of general significance.

7. The increased fracture toughness resulting from the formation of reverted austenite should be detected in all grades of maraging steel. Similarly, the acicular structures produced by high thermal cycle peak temperatures should also produce increases in fracture toughness in other grades of maraging steel, providing the alloy is not susceptible to grain boundary embrittlement.

8. The use of a simulation technique provides a means of obtaining H.A.Z. data that is not revealed by testing in the real situation. Provided it is first justified, the simulation approach should be advantageous in H.A.Z. studies of other alloys.

6. GENERAL IMPLICATIONS AND FUTURE WORK

The findings of this investigation lead to a number of general implications that justify further work. One of the major implications concerns the thermal simulation technique. In the 300 grade maraging steel alloy used in this investigation it was found that thermal simulation alone produced properties and microstructures that correlated with those in the real weld H.A.Z. Similar findings have also been reported in mild and low alloy steel weld H.A.Z.s[90,91]. However, there is no reason to suppose that this will be the case in all materials, and other factors such as the effects of strain could be of considerable significance. Consequently, an examination of the factors affecting the validity of thermal simulation in other alloys would form the basis of extremely useful work. Indeed, if this approach is adopted in any future H.A.Z. investigation it is essential that it is first justified by comparison with the real weld H.A.Z.

A finding with equally important implications, is the variation in properties with the H.A.Z. thermal cycle peak temperature. The results of this investigation show that the properties, as well as some microstructural features, are dependent only on the peak temperature. This relationship is of considerable practical significance since it enables the properties of any weld H.A.Z. position to be predicted from a knowledge of the peak temperature distribution. The fact that the transformations in maraging steel are relatively insensitive to heating and cooling rates no doubt contributes to this finding. Nevertheless, the possibility of similar relationships being found in other materials is worthy of further investigation.

In low alloy carbon steels and other materials involving complex heat treatments, the effects of heating and cooling rates are likely to be more significant than was found in this investigation. However, the thermal cycle peak temperature would still be expected to be of equal importance. In materials of this type the effects of heating and cooling rate should be examined as well as the effects of peak temperature.

Two specific areas present possibilities for future work on maraging steels. Firstly, although constitutional liquation of inclusions did not produce grain boundary embrittlement in this investigation, it has been encountered in other work. The factor separating the two situations appears to be the composition and resulting cleanliness of the parent material. Consequently, the effects of composition on constitutional liquation and grain boundary embrittlement would form a useful investigation. Finally, this investigation has shown that high temperature acicular structures produce an increase in the H.A.Z. fracture toughness. This finding has been explained in a qualitative manner. However, a more quantitative relationship may be established if further examination, possibly utilising electron microscopy, was carried out on these structures.

7. ACKNOWLEDGEMENTS

The author wishes to thank Dr. M. F. Jordan for his supervision, interest and stimulating discussion throughout this investigation. Thanks are also due to Professor W. O. Alexander, Head of the Department of Metallurgy, for providing laboratory facilities, and to the Science Research Council for their financial support. The author also appreciates the co-operation of the United Kingdom Atomic Energy Authority in providing the thermal simulation facilities and the assistance of D. Crichton with this work. Similarly, the supply of material and much useful data by Bristol Aerojet Ltd. is gratefully acknowledged. The assistance of J. P. B. Smith with the computer programme and the staff and technicians of the Department of Metallurgy with many practicalities are equally appreciated.

Finally, the author wishes to thank his wife for her continuous encouragement and support throughout the course of this research.

8. APPENDIX

The full programme for computing H.A.Z. thermal cycles using Rosenthal's two-dimensional heat flow equation is given on the following pages 239-242. The programme is written in 1900 Algol and was run on a ICL 1905A series computer with a 32K core store. Once the programme has been compiled by the computer it is ready to accept data and compute the thermal cycles. A typical example of the data layout is as follows:

- 1	285.0	0.2120	0.050	0.0618	1200.0
1.4	- 0.0424	- 1.8	1.0	1460	10

Each number must be separated by two blank spaces, and taken in order the above data represents:

285.0	heat input, cals per sec. cm thickness
0.2120	welding speed, cms per sec.
0.050	thermal conductivity cals per cm sec. ^{o}C
0.0618	thermal diffusivity cm^2 per sec.
1200.0	thermal cycle peak temperature ^{o}C
1.4 - 0.0424 - 1.8	The initial, step and final distances parallel to the welding direction over which the thermal cycle is to be calculated
1.0	a steering parameter instructing the computer to present the results in a tabular form. (It was envisaged that 2.0 would instruct a graphical output, but this section has not been written.)
1460	melting point ^{o}C. This is typed as a heading on the output.
10	required tolerance on the peak temperature, ^{o}C.

The above data has been used to compute a thermal cycle and the output is given in Table 8.1. Some of the heading is not included, but as can be seen it took three cycles to achieve the required peak temperature tolerance. The intervals of X were selected so that consecutive positions represented time increases of 0.2 secs.

Having computed the required thermal cycle the programme returns to a position for accepting new data. If - 1 is now read, the programme accepts a completely new set of data. However, one or more individual pieces of data can be replaced without clearing all the existing data. This is achieved by indicating the data positions to be changed and the new data to be inserted. This is followed by q 0 which terminates the reading sequence and allows computation to commence. For example, in the above data the heat input and peak temperature can be changed and a new thermal cycle computed by the following data:

1 450.0 5 1325 0

The computations can be finally terminated using a terminator card:

1 - 1 0

This terminator card remains the same whether one or several thermal cycles have been computed.

```
17/08/71          COMPILED BY XALE MK.  5C

'SEND TO' ( ED,ICLA-DEFAULT(0),,PROGRAM)
'WORK' (ED,WORK FILE    (0))
'BEGIN' 'COMMENT' WELDMODEL1 MTSTF043 SMITH.PROGRAM USES THE TWO-
                  DIMENSIONAL INFINITE PLATE MODEL TO CALCULATE THE TEMP.
                  DISTRIBUTION FOR VARIOUS POSITIONS FROM THE WELD POOL.
                  POSITIONS VARY ALONG AN AXIS PARALLEL TO THE WELDING
                  HEAD MOVEMENT (X) AND Y VALUES ARE CHOSEN TO CORRESPOND
                  TO A REQUIRED PEAK TEMP. Y VALUES ARE MODIFIED BY
                  FEEDBACK TO ENSURE PEAK TEMP. FALLS WITHIN THE REQUIRED
                  RANGE ;
      'REAL'PI,MT,PE,TP,DP,MM,CO,TD,DI,AR;
      'INTEGER'A,B,Z,Y,X,W,V;
      'ARRAY'AA[1:12];
'PROCEDURE' KOZ1(A,B) ;
'COMMENT' PROCEDURE EVALUATES KOZ FOR WELD CALCS WHERE MATERIAL HAS LOW
        LAMBDA VALUE ;
'REAL' A,B ;
'BEGIN''REAL' T1,T2,FACR,WW,XX,YY,IOZ,H;
      'INTEGER' R,T ;
      IOZ:=1 ;
      FACR:=1 ;
      R:=0 ;
      T2:= 0.5 ;
      'FOR' R:=R+1 'WHILE' IOZ/(IOZ-T2) 'GT' 1.0000002 'DO'
      'BEGIN' FACR:=FACR*R ;
              T2:= B↑(2*R)/FACR↑2 ;
              IOZ:=IOZ+T2 ;
      'END' ;
      H:=0 ;
      FACR:=1 ;
      R:=0 ;
      T2:= 2 ;
      'FOR' R:=R+1 'WHILE' T2 'GT' 1.0000002 'DO'
      'BEGIN' YY:=0 ;
              WW:=B↑(2*R) ;
              FACR:=FACR*R ;
              XX:=FACR*FACR ;
              'FOR' T:=1 'STEP' 1 'UNTIL' R 'DO'
                YY:=YY+1/T  ;
              T1:=(WW/XX)*YY;
              H:=H+T1 ;
              'IF' R-1 'EQ' 0
              'THEN' T2:=2
              'ELSE' T2:=H/(H-T1) ;
      'END' ;
      A:=-(0.57721567+LN(B))+IOZ+H ;
'END' ;
'PROCEDURE' KOZ2(A,B,E)  ;
'COMMENT' PROCEDURE EVALUATES KOZ FOR WELD CALCS WHERE MATERIAL HAS HIGH
        LAMBDA VALUE ;
'REAL' A,B,E  ;
'BEGIN'
      A:=SQRT(PI*B)*(1.0-0.125/E+4.5/(64*E*E)) ;
'END' ;
      'PROCEDURE' TEMP(A,B,C) ;
      'VALUE' C ;
      'INTEGER' C ;
```

```
    'ARRAY' A,B ;
    'BEGIN''REAL' S,E,KNE,EX,SH ;
          S:=SQRT(A[C]*A[C]+DI*DI) ;
          F:=AA[10]*AA[2]*S ;
          'IF' AA[10]-3 'LT' 0
          'THEN''BEGIN'
                        SH:=E/2;
                        KOZ1(KNE,SH);
                'END'
          'ELSE''BEGIN'
                        SH:=1/(2*E);
                        KOZ2(KNE,SH,E) ;
                'END' ;
          EX:=-AA[10]*AA[2]*(S+A[C]) ;
          'IF' ABS(EX) 'GT' 75.0
          'THEN' B[C]:=19
          'ELSE' B[C]:=20+AA[1]*KNE*EXP(EX)/(2*PI*AA[3]) ;
    'END' ;
    'PROCEDURE' GUESS(A,B,C,D);
    'REAL' A,B,C,D ;
    'BEGIN' 'REAL' Z;
          Z:=(A-B)/B;
          D:=C+Z*C;
    'END';
    PI:=3.1415927 ;
ONE;A:=READ ;
    'IF' A 'GT' 0
    'THEN''BEGIN'
                AA[A]:=READ ;
                'IF' A 'EQ' 4
                'THEN' AA[10]:=1/(2*AA[4]) ;
                'GOTO' ONE ;
          'END' ;
    'IF' A 'LT' 0
    'THEN''BEGIN'
                'FOR' B:= 1 'STEP' 1 'UNTIL' 9 'DO'
                AA[B]:=READ ;
                AA[10]:=1/(2*AA[4]) ;
                AA[11]:=READ;
                AA[12]:=READ;
          'END' ;
    'IF' AA[1] 'LT' 0 'THEN' 'GOTO' STOP;
    'IF' AA[1]  'EQ' 0 'THEN' 'GOTO' ONE;
    SPACE(2); WRITETEXT('('WELDING%HEAT%FLOW')') ; NEWLINE(1);
    SPACE(2); WRITETEXT('('2-D%INFINITE%PLATE%MODEL')') ; NEWLINE(3);
    SPACE(5); WRITETEXT('('WELDING%CONDITIONS')') ; NEWLINE(1);
    SPACE(5); WRITETEXT('('HEAT%INPUT,Q0%=')');PRINT(AA[1],4,1);
    NEWLINE(1); SPACE(5);WRITETEXT('('HEAD%SPEED,V%=')');SPACE(4);
    PRINT(AA[2],1,4) ;NEWLINE(2) ;
    SPACE(5); WRITETEXT('('THERMAL%CONSTANTS')'); NEWLINE(1) ;
    SPACE(5); WRITETEXT('('CONDUCTIVITY,K%=')'); SPACE(2) ;
    PRINT(AA[3],1,4) ; NEWLINE(1); SPACE(5) ;
    WRITETEXT('('DIFFUSIVITY%=')');SPACE(4) ; PRINT(AA[4],2,4) ;
    NEWLINE(1) ;SPACE(5); WRITETEXT('('LAMBDA%=')');SPACE(9) ;
    PRINT(AA[10],2,4) ; NEWLINE(2) ;
    SPACE(5) ; WRITETEXT('('MELTING%POINT%=')') ;
    PRINT(AA[11],4,1) ; NEWLINE(1) ; SPACE(5) ;
    WRITETEXT('('TOLERANCE%=')') ; SPACE(6);
    PRINT(AA[12],2,1) ; NEWLINE(1) ;
    SPACE(5) ; WRITETEXT('('AIM%FOR%PEAK')') ;
```

```
        SPACE(3); PRINT(AA[5],4,1) ;
        NEWLINE(2) ;
        DI:= (AA[1]/(8*AA[3]*AA[5])-0,20)+2*AA[4]/AA[2] ;
        A:=0 ;
        Z:=ENTIER((ABS(AA[8]-AA[6])+0,51)/AA[7]);
        'IF' Z 'LT' 0
        'THEN' Z:=-Z ;
'BEGIN'
        'ARRAY' BB[0:Z],CC[1:Z] ;
'PROCEDURE' OUTPUT1(Z) ;
 'VALUE' Z ;
'INTEGER' Z ;
 'BEGIN'
        'REAL' ZZ ;
        ZZ:=ENTIER(Z/3)+1 ;      SPACE(8) ;
        SPACE(1) ;
        WRITETEXT('('X'('13S')'TEMP'('17S')'X'('13S')'TEMP'('17S')'X'('
                13S')'TEMP')') ;    NEWLINE(2) ;
        'FOR' A:=1 'STEP' 1 'UNTIL' ZZ 'DO'
        'BEGIN' SPACE(5) ; PRINT(CC[A],2,4) ; SPACE(5) ; PRINT(BB[A],4,2);
                SPACE(10); PRINT(CC[A+ZZ],2,4);SPACE(5); PRINT(BB[A+ZZ],4
                ,2); SPACE(10) ;
                'IF' A+(2*ZZ) 'LT' Z
                'THEN''BEGIN'
                                PRINT(CC[A+(2*ZZ)],2,4);SPACE(5) ;
                                PRINT(BB[A+(2*ZZ)],4,2);NEWLINE(1)
                        'END'
                'ELSE' NEWLINE(1) ;
        'END' ;
        PAPERTHROW ;
 'END' OUTPUT1(Z) ;
        'PROCEDURE' OUTPUT2 ;
        'BEGIN'SPACE(5) ;
              WRITETEXT('('CYCLE%NUMBER')') ; SPACE(8) ;
              PRINT(Y,2,0) ; NEWLINE(1) ;  SPACE(5) ;
              WRITETEXT('('Y%DISTANCE(CMS.)')') ;  SPACE(4) ;
              PRINT(DP,2,4) ;NEWLINE(1) ;  SPACE(5) ;
              WRITETEXT('('PEAK%TEMP.(C)')') ; SPACE(5) ;
              PRINT(MT,4,2) ;NEWLINE(1) ;  SPACE(5) ;
              WRITETEXT('('X%DISTANCE(CMS.)')') ; SPACE(4) ;
              PRINT(CC[X],2,4);NEWLINE(2) ;
        'END' ;
        'FOR' AR:=AA[6] 'STEP' AA[7] 'UNTIL' 'IF' AA[8] 'LT' 0
                                        'THEN' AA[8] -0.1
                                        'ELSE' AA[8] +0.1
        'DO'
        'BEGIN' A:=A+1 ;
              CC[A]:=AR ;
        'END' ;
        Z:=A ;
   TWO:Y:=0 ;
   THR:Y:=Y+1 ;
        BB[0]:=0.0;
        'FOR' A:= 1 'STEP' 1 'UNTIL' Z 'DO'
        'BEGIN' TEMP(CC,BB,A) ;
                'IF' BB[A] 'LT' BB[A-1]
                'THEN''GOTO'NEXT ;
        'END' ;
 NEXT:MT:=BB[A-1] ;
        X:=A-1 ;
```

```
'IF' ABS(MT-AA[5]) 'LT' AA[12]
'THEN''BEGIN'
                'FOR' A:=X 'STEP' 1 'UNTIL' Z 'DO'
               TEMP(CC,BB,A);
               'IF' AA[9] 'EQ' 1
               'THEN''BEGIN'
                                  NEWLINE(1);SPACE(5);
                                  WRITETEXT('('CYCLEXNUMBER')');
                                  SPACE(8); PRINT(Y,2,0); NEWLINE(1);
                                  SPACE(5);WRITETEXT('('FINALXYXDISTANCE')'
                                  );SPACE(3);PRINT(DI,2,4) ;NEWLINE(2);
                                  OUTPUT1(Z) ;
                        'END' ;
           'GOTO' ONE;
     'END'
'ELSE'
DP:=DI;
OUTPUT2;
GUESS(MT,AA[5],DP,DI);
'GOTO' THR;
'END' ;
STOP;'END';
```

CYCLE NUMBER 3
FINAL Y DISTANCE 0.2767

X	TEMP	X	TEMP	X	TEMP
1.4000	25.47	0.2552	486.98	-0.8896	814.45
1.3576	26.41	0.2128	573.45	-0.9320	800.97
1.3152	27.51	0.1704	672.48	-0.9744	788.15
1.2728	28.80	0.1280	781.84	-1.0168	775.93
1.2304	30.31	0.0856	895.70	-1.0592	764.26
1.1880	32.09	0.0432	1004.19	-1.1016	753.10
1.1456	34.18	0.0008	1095.34	-1.1440	742.42
1.1032	36.65	-0.0416	1159.58	-1.1864	732.19
1.0608	39.55	-0.0840	1193.84	-1.2288	722.38
1.0184	42.96	-0.1264	1201.95	-1.2712	712.95
0.9760	46.98	-0.1688	1191.33	-1.3136	703.89
0.9336	51.73	-0.2112	1169.41	-1.3560	695.17
0.8912	57.33	-0.2536	1141.81	-1.3984	686.77
0.8488	63.94	-0.2960	1112.12	-1.4408	678.67
0.8064	71.76	-0.3384	1082.37	-1.4832	670.85
0.7640	81.01	-0.3808	1053.59	-1.5256	663.31
0.7216	91.96	-0.4232	1026.24	-1.5680	656.02
0.6792	104.94	-0.4656	1000.47	-1.6104	648.96
0.6368	120.35	-0.5080	976.30	-1.6528	642.14
0.5944	138.65	-0.5504	953.64	-1.6952	635.53
0.5520	160.42	-0.5928	932.39	-1.7376	629.12
0.5096	186.33	-0.6352	912.44	-1.7800	622.91
0.4672	217.23	-0.6776	893.68	-1.8224	616.88
0.4248	254.10	-0.7200	876.01		
0.3824	298.10	-0.7624	859.33		
0.3400	350.59	-0.8048	843.56		
0.2976	413.06	-0.8472	828.62		

Table 8.1. Computed thermal cycle, presented as the temperature at a position x along a line parallel to the weld centre line.

9. REFERENCES

1. C. G. BIEBER, Metal Prog., 1960, 78, 99-100.
2. R. F. DECKER et al, Mater. Des. Engng., 1962, 55, 106-111.
3. R. F. DECKER et al, Trans. Am. Soc. Metals, 1962, 55, 58-76.
4. S. FLOREEN and R. F. DECKER, ibid, 1962, 55, 518-530.
5. G. P. CONTRACTOR, J. Metals, 1966, 18, 938-946.
6. N. A. MATTHEWS et al, Am. Soc. Metals, Metals Engng. Quart., 1963, 3, 1-10.
7. J. A. SRAWLEY, Proc. 2nd Int. Conf. Fracture, Brighton, 1969, 131-146.
8. H. T. CORTEN, Ocean Engng., 1969, 1, 261-284.
9. S. FLOREEN, Metall. Rev., 126, 1968, 13, 115-128.
10. E. A. OWEN and Y. H. LIU, J. Iron Steel Inst., 1949, 163, 132-137.
11. F. W. JONES and W. I. PUMPHREY, ibid, 1949, 163, 121-131.
12. W. D. SWANSON and J. G. PARR, ibid, 1964, 202, 104-106.
13. S. FLOREEN, Trans. Metall. Soc. A.I.M.E., 1964, 230, 842-849.
14. S. FLOREEN, ibid, 1966, 236, 1429-1440.
15. P. M. KELLY and J. NUTTING, Proc. Roy. Soc. A., 1961, 259, 45-58.
16. O. JOHARI and G. THOMAS, Acta. Metall., 1965, 13, 1211-1212.
17. R. B. G. YEO, Trans. Metall. Soc. A.I.M.E., 1963, 227, 884-890.
18. B. G. REISDORF, Trans. Am. Soc. Metals, 1963, 56, 783-786.

19. G. P. MILLAR and W. I. MITCHELL, J. Iron Steel Inst., 1965, 203, 899-904.

20. H. MARCUS et al, Trans. Am. Soc. Metals, 1966, 59, 468-478.

21. J. M. CHITTON and C. J. BARTON, ibid, 1967, 60, 528-542.

22. S. FLOREEN and G. R. SPEICH, ibid, 1964, 57, 714-726.

23. D. T. PETERS and C. R. CUPP, Trans. Metall. Soc. A.I.M.E., 1966, 236, 1420-1429.

24. A. A. GRIFFITH, Phil. Trans. R. Soc., 1920, 221, 163-198.

25. C. E. INGLIS, Trans. Instn. Nav. Archit., 1913, 55, 219-230.

26. V. WEISS and S. YUKAWA, A.S.T.M., S.T.P. 381, 1965, 1-22.

27. E. OROWAN, Trans. Instn., Engrs. Shipbldrs. Scotl., 1945, 89, 165-215.

28. E. OROWAN, Weld. J., 1955, 34, 157s-160s.

29. G. R. IRWIN, Fracturing of Metals, Am. Soc. Metals, 1948, 147-166.

30. G. R. IRWIN, J. Appl. Mech., 1957, 24, 361-364.

31. P. C. PARIS and C. SIH, A.S.T.M., S.T.P. 381, 1965, 30-81.

32. J. T. BARNBY, Weld. Metal Fabric., 1969, 37, 71-75.

33. W. F. BROWN, Jr. and J. E. SRAWLEY, A.S.T.M., S.T.P. 410, 1966.

34. B.I.S.R.A., Open Report, MG/EB/312/67.

35. A.S.T.M. Special Committe, 5th Report, Matls. Res. Stds, 1964, 4, 107-119.

36. G. R. IRWIN, J. Appl. Mech., 1962, 84E, 651-654.

37. C. F. TIFFANY and J. N. MASTERS, A.S.T.M., S.T.P. 381, 1965, 249-277.

38. C. L. M. COTTRELL and P. F. LANGSTONE, J. Iron Steel Inst., 1968, 206, 1077-1087.

39. C. L. M. COTTRELL, Brit. Weld. J., 1968, 15, 262-267.

40. N. J. PETCH, J. Iron Steel Inst., 1953, 174, 25-28.

41. J. R. LOW, Jr., Relation of Properties to Microstructure, Am. Soc. Metals, 1954, 163-179.

42. A. T. ENGLISH and W. A. BACKOFEN, Fracture. An Advanced Treatise, Volume 6, Academic Press, 1969.

43. W. E. DUCKWORTH et al, B.I.S.R.A. Report MG/E/170/65.

44. A. J. BIRKLE et al, Trans. Am. Soc. Metals, 1965, 58, 285-301.

45. G. T. HAHN and A. R. ROSENFIELD, Acta Metall., 1966, 14, 1815-1825.

46. K. E. PUTTICK, Phil. Mag., 1959, 4, 964-969.

47. C. J. McMAHON and M. COHEN, Acta Metall., 1965, 13, 591-604.

48. J. T. BARNBY, ibid, 1967, 15, 903-909.

49. S. FLOREEN and H. W. HAYDEN, Metal Sci. J., 1970, 4, 77-80.

50. C. D. BEACHEM and R. M. N. PELLOUX, A.S.T.M., S.T.P. 381, 1965, 210-244.

51. L. ROESCH and G. HENRY, A.S.T.M., S.T.P. 453, 1969, 3-29.

52. A. S. TETELMAN and A. J. McEVILY, Jr., Fracture of Structural Materials, Wiley, 1967.

53. J. M. KRAFFT, Appl. Matls, Res., 1964, 3, 88-101.

54. J. M. KRAFFT, Nat. Symp. Fract. Mechs., Lehigh Univ., Pa., June 1967.

55. A. J. BIRKLE et al, Trans. Am. Soc. Metals, 1966, 59, 981-990.

56. W. A. SPITZIG, A.S.T.M., S.T.P. 453, 1969, 90-110.

57. A. A. WELLS, Brit. Weld. J., 1963, 10, 563-570.

58. B. COTTERELL, Proc. 1st. Int. Conf. Fracture, Sendai, 1966, 1663-1672.

59. W. A. SPITZIG, Trans. Am. Soc. Metals, 1968, 61, 344-349.

60. T. BONISZEWSKI and D. M. KENYON, Brit. Weld. J., 1966, 13, 415-435.

61. F. D. DUFFEY and W. SUTAR, Weld. J., 1965, 44, 251s-263s.

62. E. M. WILSON and A. I. WILDMAN, Brit. Weld. J., 1966, 13, 67-74.

63. H. E. ROMINE, N.A.S.A., CR-302, Sept. 1965.

64. H. E. ROMINE, Third Maraging Steel Project Review, RTD-TDR-63-4048, AFML, Nov. 1963.

65. D. A. CORRIGAN, Weld. J., 1964, 43, 289s-294s.

66. C. M. ADAMS and R. E. TRAVIS, ibid, 1964, 43, 193s-197s.

67. A. T. D'ANNESSA, Brit. Weld. J., 1967, 14, 62-70.

68. N. KENYON, Weld. J., 1968, 47, 193s-198s.

69. C. E. WITHERELL et al, Metal Prog., 1963, 84, 81-83.

70. N. BAILEY, Metal. Const., 1971, 3, 1-5.

71. P. H. SALMON COX et al, Trans. Am. Soc. Metals, 1967, 60, 125-143.

72. W. A. PETERSEN, Weld. J., 1964, 43, 428s-432s.

73. A. I. WILDMAN, Bristol Aerojet Ltd., T.R.No. 468, April 1968.

74. P. F. LANGSTONE, ibid., T.R.No. 467, April 1968.

75. L. GROOME, ibid, T.R.No. 480, August 1968.

76. J. J. PEPE and W. F. SAVAGE, Weld. J., 1967, 46, 411s-422s.

77. J. J. PEPE and W. F. SAVAGE, ibid, 1970, 49, 545s-553s.

80. T. and E. BONISZEWSKI, J. Iron Steel Inst., 1966, 204, 360-365.

81. N. P. ALLEN and C. C. EARLEY, ibid., 1960, 166, 281-228.

82. A. J. SEDRIKS and J. V. CRAIG, ibid, 1965, 203, 268-272.

83. R. F. DECKER, N.P.L. Symp. No. 15, H.M.S.O., 1963, 647-671.

84. P. H. SALMON COX et al, Trans. Metall. Soc., A.I.M.E., 1967, 239, 1809-1817.

85. T. BONISZEWSKI et al, Iron Steel Inst. Special Report No. 76, 1962, 100-105.

86. Z. P. SAPERSTEIN et al, A.I.M.E. Met. Soc. Conf., 1966, 31, 163-225.

87. A. S. TETELMAN, Stanford Univ., Dept. Matls. Sci., Report No. 66-37, 1966.

88. D. J. WIDGERY, Metal Const., 1969, 1, 328-332.

89. W. F. SAVAGE, J. Appl. Polym. Sci., 1962, 6, 303-315.

90. E. SMITH et al, Weld. Metal Fabric., 1970, 38, 242-251.

91. E. SMITH et al, Weld Metal Fabric., 1970, 38, 496-504.

92. J. CARGILL, Strain, 1970, 6, 6-13.

93. I. HRIVNAK, Theory of mild and micro-alloy steels weldability, Bratislava, Alfa, 1969.

94. B. WATKINS et al, Brit. Weld. J., 1966, 13, 350-356.

95. R. E. DOLBY and D. J. WIDGERY, Welding Institute Members Report No. M/52/70.

96. R. E. DOLBY, ibid, M/53/70.

97. D. ROSENTHAL, Weld. J., 1941, 20, 220s-234s.

98. D. ROSENTHALL, Trans. Am. Soc. Mech. Engrs, 1946, 68, 849-866.

99. P. S. MYERS et al, Welding Research Council Bulletin, 1968.

100. W. F. HESS et al, Weld. J., 1943, 22, 377s-422s.

101. A. A. WELLS, ibid, 1952, 31, 263s-267s.

102. D. K. ROBERTS and A. A. WELLS, Brit. Weld. J., 1954, 1, 553-560.

103. R. L. APPS and D. R. MILNER, ibid., 1955, 2, 475-485.

104. N. CHRISTENSEN et al, ibid, 1965, 12, 54-75.

105. B. W. RALPH, M.Sc. Thesis, Univ. of Aston in Birmingham, 1966.

106. C. M. ADAMS, Jr., Weld J., 1958, 37, 210s-215s.

107. V. PAVELIC et al, ibid, 1969, 48, 295s-305s.

108. E. F. WALKER and M. J. MAY, B.I.S.R.A. Open Report MG/E/307/67.

109 E. T. WHITTAKER and G. N. WATSON, A Course of Modern Analysis, 4th ed., Cambridge Univ. Press, 1952.

110. A. SANDERSON, The Welding Institute, private communication.

111. Aerospace Structural Metals Handbook, 1, Syracuse Univ. Press, 1966.

112. G. R. SALTER, BWRA, Report No. C116/4/66.

113. B. D. CULLITY, Elements of X-ray diffraction, Adison-Wesley, 1959.

114. A.S.T.M., S.T.P. 463, 1970.

115. P. F. LANGSTONE and G. ANDERTON, Bristol Aerojet Ltd., private communication.

116. G. T. HAHN and A. R. ROSENFELD, A.S.T.M., S.T.P. 432, 1968, 5-32.